Registration of Medical Images:
Methods of Point Matching by Geometric Transformation

by

Michael Wirth

A Thesis
Submitted to the Faculty of Graduate Studies
in Partial Fulfillment of the Requirements
for the Degree of

Master of Science

Department of Computer Science
University of Manitoba
Winnipeg, Manitoba
Canada

ISBN 0-612-13567-5

Name Michael Andrew Wirth

Dissertation Abstracts International is arranged by broad, general subject categories. Please select the one subject which most nearly describes the content of your dissertation. Enter the corresponding four-digit code in the spaces provided.

APPLIED SCIENCES

SUBJECT TERM

0984

SUBJECT CODE

U·M·I

Subject Categories

THE HUMANITIES AND SOCIAL SCIENCES

COMMUNICATIONS AND THE ARTS

Architecture 0729
Art History 0377
Cinema 0900
Dance 0378
Fine Arts 0357
Information Science 0723
Journalism 0391
Library Science 0399
Mass Communications 0708
Music 0413
Speech Communication 0459
Theater 0465

EDUCATION

General 0515
Administration 0514
Adult and Continuing 0516
Agricultural 0517
Art 0273
Bilingual and Multicultural 0282
Business 0688
Community College 0275
Curriculum and Instruction 0727
Early Childhood 0518
Elementary 0524
Finance 0277
Guidance and Counseling 0519
Health 0680
Higher 0745
History of 0520
Home Economics 0278
Industrial 0521
Language and Literature 0279
Mathematics 0280
Music 0522
Philosophy of 0998
Physical 0523
Psychology 0525
Reading 0535
Religious 0527
Sciences 0714
Secondary 0533
Social Sciences 0534
Sociology of 0340
Special 0529
Teacher Training 0530
Technology 0710
Tests and Measurements 0288
Vocational 0747

LANGUAGE, LITERATURE AND LINGUISTICS

Language
- General 0679
- Ancient 0289
- Linguistics 0290
- Modern 0291

Literature
- General 0401
- Classical 0294
- Comparative 0295
- Medieval 0297
- Modern 0298
- African 0316
- American 0591
- Asian 0305
- Canadian (English) 0352
- Canadian (French) 0355
- English 0593
- Germanic 0311
- Latin American 0312
- Middle Eastern 0315
- Romance 0313
- Slavic and East European 0314

PHILOSOPHY, RELIGION AND THEOLOGY

Philosophy 0422
Religion
- General 0318
- Biblical Studies 0321
- Clergy 0319
- History of 0320
- Philosophy of 0322

Theology 0469

SOCIAL SCIENCES

American Studies 0323
Anthropology
- Archaeology 0324
- Cultural 0326
- Physical 0327

Business Administration
- General 0310
- Accounting 0272
- Banking 0770
- Management 0454
- Marketing 0338

Canadian Studies 0385
Economics
- General 0501
- Agricultural 0503
- Commerce-Business 0505
- Finance 0508
- History 0509
- Labor 0510
- Theory 0511

Folklore 0358
Geography 0366
Gerontology 0351
History
- General 0578
- Ancient 0579
- Medieval 0581
- Modern 0582
- Black 0328
- African 0331
- Asia, Australia and Oceania 0332
- Canadian 0334
- European 0335
- Latin American 0336
- Middle Eastern 0333
- United States 0337

History of Science 0585
Law 0398
Political Science
- General 0615
- International Law and Relations 0616
- Public Administration 0617

Recreation 0814
Social Work 0452
Sociology
- General 0626
- Criminology and Penology 0627
- Demography 0938
- Ethnic and Racial Studies 0631
- Individual and Family Studies 0628
- Industrial and Labor Relations 0629
- Public and Social Welfare 0630
- Social Structure and Development 0700
- Theory and Methods 0344

Transportation 0709
Urban and Regional Planning 0999
Women's Studies 0453

THE SCIENCES AND ENGINEERING

BIOLOGICAL SCIENCES

Agriculture
- General 0473
- Agronomy 0285
- Animal Culture and Nutrition 0475
- Animal Pathology 0476
- Food Science and Technology 0359
- Forestry and Wildlife 0478
- Plant Culture 0479
- Plant Pathology 0480
- Plant Physiology 0817
- Range Management 0777
- Wood Technology 0746

Biology
- General 0306
- Anatomy 0287
- Biostatistics 0308
- Botany 0309
- Cell 0379
- Ecology 0329
- Entomology 0353
- Genetics 0369
- Limnology 0793
- Microbiology 0410
- Molecular 0307
- Neuroscience 0317
- Oceanography 0416
- Physiology 0433
- Radiation 0821
- Veterinary Science 0778
- Zoology 0472

Biophysics
- General 0786
- Medical 0760

EARTH SCIENCES

Biogeochemistry 0425
Geochemistry 0996
Geodesy 0370
Geology 0372
Geophysics 0373
Hydrology 0388
Mineralogy 0411
Paleobotany 0345
Paleoecology 0426
Paleontology 0418
Paleozoology 0985
Palynology 0427
Physical Geography 0368
Physical Oceanography 0415

HEALTH AND ENVIRONMENTAL SCIENCES

Environmental Sciences 0768
Health Sciences
- General 0566
- Audiology 0300
- Chemotherapy 0992
- Dentistry 0567
- Education 0350
- Hospital Management 0769
- Human Development 0758
- Immunology 0982
- Medicine and Surgery 0564
- Mental Health 0347
- Nursing 0569
- Nutrition 0570
- Obstetrics and Gynecology 0380
- Occupational Health and Therapy 0354
- Ophthalmology 0381
- Pathology 0571
- Pharmacology 0419
- Pharmacy 0572
- Physical Therapy 0382
- Public Health 0573
- Radiology 0574
- Recreation 0575
- Speech Pathology 0460
- Toxicology 0383

Home Economics 0386

PHYSICAL SCIENCES

Pure Sciences

Chemistry
- General 0485
- Agricultural 0749
- Analytical 0486
- Biochemistry 0487
- Inorganic 0488
- Nuclear 0738
- Organic 0490
- Pharmaceutical 0491
- Physical 0494
- Polymer 0495
- Radiation 0754

Mathematics 0405
Physics
- General 0605
- Acoustics 0986
- Astronomy and Astrophysics 0606
- Atmospheric Science 0608
- Atomic 0748
- Electronics and Electricity 0607
- Elementary Particles and High Energy 0798
- Fluid and Plasma 0759
- Molecular 0609
- Nuclear 0610
- Optics 0752
- Radiation 0756
- Solid State 0611

Statistics 0463

Applied Sciences

Applied Mechanics 0346
Computer Science 0984
Engineering
- General 0537
- Aerospace 0538
- Agricultural 0539
- Automotive 0540
- Biomedical 0541
- Chemical 0542
- Civil 0543
- Electronics and Electrical 0544
- Heat and Thermodynamics 0348
- Hydraulic 0545
- Industrial 0546
- Marine 0547
- Materials Science 0794
- Mechanical 0548
- Metallurgy 0743
- Mining 0551
- Nuclear 0552
- Packaging 0549
- Petroleum 0765
- Sanitary and Municipal 0554
- System Science 0790

Geotechnology 0428
Operations Research 0796
Plastics Technology 0795
Textile Technology 0994

PSYCHOLOGY

General 0621
Behavioral 0384
Clinical 0622
Developmental 0620
Experimental 0623
Industrial 0624
Personality 0625
Physiological 0989
Psychobiology 0349
Psychometrics 0632
Social 0451

REGISTRATION OF MEDICAL IMAGES:

METHODS OF POINT MATCHING BY GEOMETRIC TRANSFORMATION

BY

MICHAEL WIRTH

A Thesis submitted to the Faculty of Graduate Studies of the University of Manitoba in partial fulfillment of the requirements for the degree of

MASTER OF SCIENCE

Dedication

This thesis is dedicated to all the women in my life without which whose encouragement and friendship I would not be where I am today. To all those who believed in me. To my Mom, Monica, Catherine, Cyndy, Meghan, Edwina, Sally, Natasha, Leanne, Georgina and Nikki.

Table of Contents

3 Control Point Selection

4 Control Point Matching

5 Geometric Transformations

List of Figures

List of Tables

Abstract

This dissertation presents a point-matching technique for registering distorted monomodal and multimodal medical images using geometric transformations. The point-matching registration technique is composed of three components: control-point selection, control-point matching and geometric transformation. The main focus of the research is on methods of automatic control-point selection and the generation of an appropriate transformation function. The methods of geometric transformation include both linear (affine) and non-linear (polynomial and surface-spline) models. The performance of each of the transformation methods has been evaluated by a series of experiments using synthetically distorted Computed Tomography and Magnetic Resonance images containing both linear and geometric distortion.

Acknowledgments

I would like to express thanks to my supervisor, Professor Desmond Walton for his support and guidance. I would also like to express my gratitude to Professor Dereck Meek for his help. For provision of the computed tomography and magnetic resonance images I would like to thank Victoria Hospital, New York University, and the Australian Geological Survey Organization.

Chapter 1

Introduction

1.1 Background

A *modality* is the manner in which an image is obtained from a specific kind of imaging device. The term *monomodal* refers to a single modality, whereas *multimodal* refers to multiple modalities. Images of the head and body from modalities such as computed tomography (CT), magnetic resonance (MR), and positron emission tomography (PET) contain complementary anatomic (CT and MR) and physiological or functional information important to medical research, diagnosis and treatment. Image *registration,* or *matching* as it is often referred to, can be defined as matching or aligning two images by geometrically transforming one of the images.

Image registration is a classical problem. Traditionally, correlation-like techniques [13,53,84] were used to do image registration. However, this kind of approach is inherently sensitive to gray-level modification and the presence of geometric distortion, so its use in medical image registration is limited. A *point-*

matching registration technique is based on the following assumption: given two medical images of the same region of the body or head, from either the same or differing modalities, a unique point-transformation can be found which, when applied to one of the images gives the closest possible alignment of the two images [81]. For example, the evolution of a tumor can be assessed by comparing two images produced by the same modality for the same patient at different times. The integration of anatomic and physiological images allows a more accurate understanding of the physiologic and pathologic mechanisms associated with a specific disease.

The approach to image registration presented in this research is based on point-matching techniques for image registration. Essentially the method will cover the five major categories of medical registration problems, namely, multimodal, monomodal, temporal, viewpoint and template registration. The methodology involved is not unique to any one particular class of images and therefore might be applied more generally. An image often contains a subset of points which are used to describe a certain feature within the image. Such points are known as *control-points*. Image registration involves warping or modifying the geometry of an image so that the set of control points in the distorted image (Figure 1-1(a)) have the same spatial relationship as those in the reference image (Figure 1-1(b)).

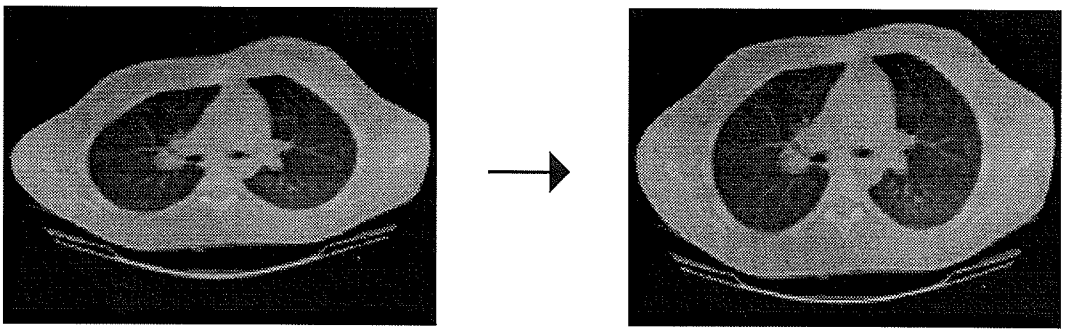

(a) (b)

Figure 1-1 Example of Image Registration (a) *Distorted Image*, (b) *Reference Image*

1.2 Preliminary Discussion

The discussion on image registration focuses on grayscale images, composed of 256 different intensities of gray. Color medical images are beyond the scope of this research, although the only fundamental difference would occur in the control-point selection technique. The point-matching registration technique is composed of three related components, namely control-point selection, control-point matching and geometric transformation. The control-point selection schema discussed here focuses on the automatic extraction of identifiable anatomic features from a medical image and subsequently deriving significant points from these features. Control-point matching matches corresponding control points in the two images into control-point pairs. Geometric transformation finds a transformation association between the two images.

First it is appropriate to discuss some of the terminology used throughout this research. Registration determines the "best-fit" between two images, one of which represents the *reference image* while the other is geometrically transformed and is known as the *distorted image*. Medical images are normally characterized as belonging to one of two types: *anatomical* or *physiological*. Anatomical images contain information relating to anatomy (e.g. soft-tissue, bone-tissue), while physiological images contain metabolic and functional information (e.g. blood flow). Five kinds of medical images are used throughout the research, namely, Computed Tomography (CT), Magnetic Resonance (MR), Single Photon Emission Computed Tomography (SPECT), Positron Emission Tomography (PET) and Ultrasound (US).

Throughout each chapter, a number of sample medical images are used. The first, shown in Figure 1-2, is a computed tomography image of a thoraxial (chest) cross-section, depicting tissue such as the spine and lungs. The second, shown in Figure 1-3 is the corresponding magnetic resonance image which provides details relating to soft-tissue structures. The shape of the chest section differs in the two images due to different arm positionings in the standard CT and MR modalities. These two images will be used to illustrate multimodal registration.

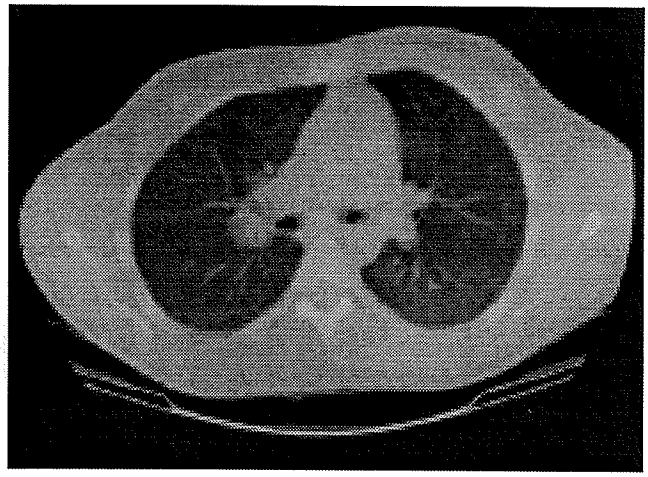

Figure 1-2. Original Thoraxial Computed Tomography Image

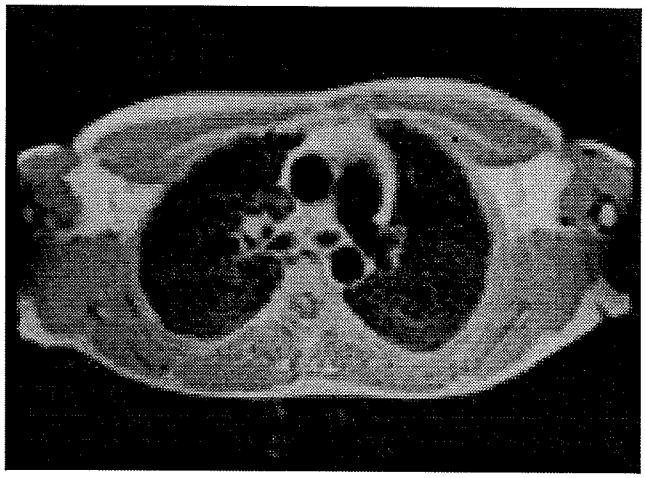

Figure 1-3. Original Throaxial Magnetic Resonance Image

The images shown in Figures 1-4 and 1-5 are part of a series of synthetically generated distortions of the image in Figure 1-2. The two images shown in Figures 1-4 and 1-5 depict linear and non-linear (geometric) distortion respectively and will be used to illustrate the differing forms of distortion found within medical images.

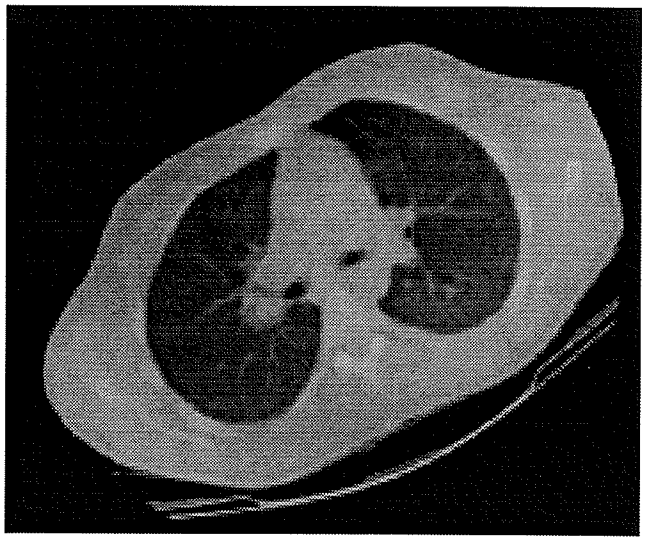

Figure 1-4. CT Image containing Linear Distortion (23° rotation)

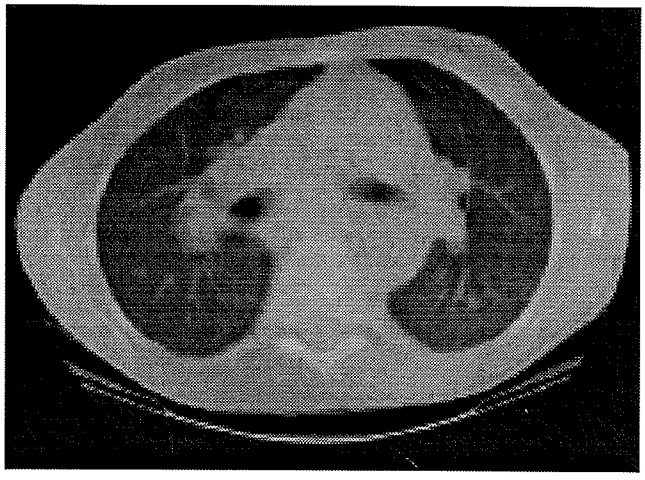

Figure 1-5. CT Image containing Geometric ("barrel") Distortion

1.3 Medical Imaging Modalities

Some significant tomographic imaging modalities used in radiology include single photon emission computed tomography (SPECT), positron emission tomography (PET), X-ray computed tomography (CT), magnetic resonance (MR) and ultrasound (US) [73]. Magnetic resonance images are useful for discerning subtle changes in soft tissues, whereas computed tomography images are most useful for visualizing bone tissue and SPECT images depict metabolism. The five categories are discussed in detail below [90,91]. It should be noted that medical images taken relative to the body are either longitudinal or transverse. Longitudinal images divide the human body in places parallel to its length and transverse images divide it perpendicular to its length.

1.3.1 Nuclear Medicine (NM)

Nuclear medicine involves the use of radionuclides (e.g. ^{11}C, ^{13}N, ^{15}O, ^{18}F) and radiopharmaceuticals in conjunction with either a rotating (360°) or stationary gamma camera to produce a specific metabolic or functional image. *Single photon emission computed tomography* (SPECT) and *positron emission tomography* (PET) are nuclear medicine modalities. In SPECT images, a radionuclide-labeled substance introduced into the body emits photons, which are detected by gamma cameras. SPECT images are used to detect bone cancer, liver disease and brain lesions. In PET images, a positronium-labeled substance introduced into the body emits oppositely directed photons in pairs, which are absorbed by a detector on either side. PET images of the brain depict several aspects of cerebral function including glucose activity, oxygen consumption, and blood flow [91].

1.3.2 Computed Tomography (CT)

In computed tomography, a narrowly collimated fan-shaped beam of X-rays emanates from the focal point of the x-ray source and passes through the body in a direction transverse to its longitudinal axis. The emerging rays are intercepted by a detector array whose length and distance from the X-ray source define the angle of the fan. The X-ray source and detector move perpendicular to the beam direction and a series of cross-sections are made at evenly spaced points. CT is commonly used to obtain images of the brain as shown in Figure 1-6. It can be used to detect deformation and displacement of normal brain tissue, characterize the position, size and density of abnormal structures in the brain, such as tumors, cysts or abscesses and can detect regions of hypoperfusion and hyperperfusion used in the diagnosis and evaluation of stroke and trauma.

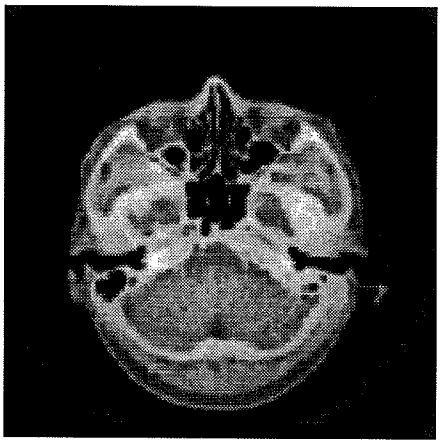

Figure 1-6. A Computed Tomography Image of the Brain

1.3.3 Magnetic Resonance (MR)

Magnetic resonance imaging, often referred to as *nuclear magnetic resonance* (NMR) uses devices that probe the magnetic moments of nuclei, employing radio frequency

(RF) radiation and strong, time varying magnetic fields. These nuclei are typically protons (H), but other nuclei, including F and sodium are also used. Properties concerning the spatial distribution of nuclear magnetization in the patient is determined from RF signal emission from the stimulated nuclei. MR images are most often used to depict soft tissue and nervous tissue, such as that shown in Figure 1-7, the MR image corresponding to the CT image of Figure 1-6.

Figure 1-7. A Magnetic Resonance Image of the Brain

1.3.4 Ultrasound (US)

Ultrasound involves the use of high frequency (5-10MHz) sonic waves to image the body. The transducer, a crystal stimulated electrically, resonating at a specific frequency transmits a brief pulse (0.2-1.0μs) which transits the patient, scattering and reflecting off tissue interfaces where there is a large acoustical impedance mismatch. The returned echoes are received by the transducer during the pulse-off time. Ultrasound is commonly used in obstetrics and the diagnosis of breast cancer [91], as normal and diseased breast tissue exhibit distinct ultrasonic properties.

1.3.5 Multimodal Images

The modalities discussed here often provide complementary information. SPECT, PET and MRS (magnetic resonance spectroscopy) images provide functional information, but delineate anatomy poorly, whereas MR, CT and ultrasound images depict aspects of anatomy, but provide little functional information. Furthermore, CT and MR images describe complementary morphological features. For example, calcifications and cortical bone are best seen on CT images, while soft-tissue structures and iron deposition are rendered most clearly by MR images [60]. Features from one modality can often be superimposed over another. For example, CT images of skeletal structures can be overlaid with MR images of soft-tissue anatomy.

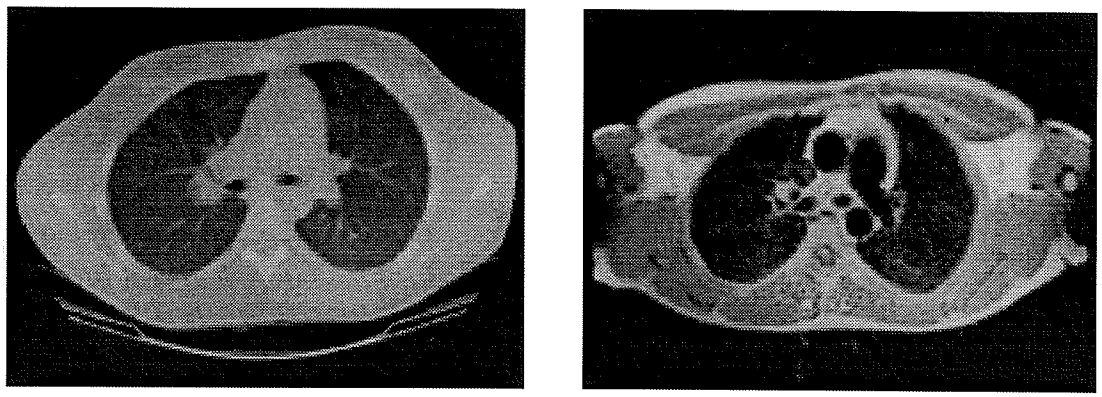

(a) (b)

Figure 1-8. Multimodal Images: (a) Computed Tomography, (b) Magnetic Resonance

Figures 1-8(a) and 1-8(b) represent computed tomography and magnetic resonance images of the thorax respectively. They are taken at the same transversal section. The shape of the chest section differs in the two images due to differences in the standard CT and MR imaging modalities. The CT image provides more detail in the lung and spinal regions. The objective is to transform the MR image to match the CT image. A

composite image could then be formed, where the lung and spine regions from the CT image are superimposed onto the MR image.

Areas of multimodality matching include radiotherapy and nuclear medicine [112]. For example, in radiation therapy, CT and MR have complementary roles. The CT image provides a map of the radiation attenuation coefficient, used to calculate dose distributions, while the anatomy of the target lesion is provided by the MR image [60]. In nuclear medicine, determination of the anatomical location of dysfunctional areas and studies of functional/structural relationships are facilitated by the integration of functional and morphological images with anatomical images may be used to improve PET or SPECT reconstruction. Registration of monomodal images can also be used for clinical diagnosis of images over a period of time.

1.4 Chapter Outline

In Chapter 2, the general concepts associated with image registration and medical images are discussed. This includes defining the problem and providing an overview of the categories of registration problems. A description of the four major techniques currently used in the registration of medical images is followed by an outline of the methodology associated with point-matching techniques. The latter portion of the chapter is devoted to the kinds of image distortion.

Chapter 3 is dedicated to control-point selection. A description of the kinds of control-points found is followed by an overview of the methodology associated with control-point selection. The focus of the chapter is placed on the automatic selection of control points from anatomic features contained within medical images. After a brief discussion on image enhancement techniques used for noise suppression and edge attenuation, the focus turns to methods of image segmentation used for feature extraction, namely edge detection and thresholding. Subsequent discussion is based

on the detection of lines, curves and corners from these edge maps. The detection of significant points from these features is the focus of the latter portion of the chapter. There, the kinds of control-points associated with lines and curves are described and a number of methods used to detect them are overviewed.

Methods employed in control-point matching are briefly described in Chapter 4. Chapter 5 describes the geometric transformation of images. The first part of the chapter focuses on the differing methods of transformation, whilst the remainder of the chapter is dedicated to methods of two-dimensioanl image transformation. Three methods are presented, each dealing with a particular kind of image distortion. Chapter 6 covers aspects relating to the reconstruction of 3-D volumetric medical images from tomographic images using the image transformation techniques discussed in Chapter 5. This leads to a brief discussion on the registration of 3-D medical images. This is essentially a preview to future research in 3-D point-matching registration techniques. Finally, Chapter 7 provides a summary of the research.

Chapter 2

Image Registration

2.1 Introduction

The diagnosis of a disease from medical images usually involves two steps. The first one, registration, discards image differences produced by distortion. The second step, comparison, estimates differences induced by actual modifications in the image. Diagnosis is based on such differences [34]. This chapter is divided into six sections. A description of image registration is given in Section 2.2. Section 2.3 outlines the five major categories of registration. The major approaches to medical image registration are covered in Section 2.4, followed by the methodology associated with point-matching methods in Section 2.5. Finally, image distortions and their relationship to solving the registration problem are described in Section 2.6.

2.2 Definition

Registration can be defined as matching or aligning two or more images of the same scene taken from different modalities or at different times using geometric properties that are common to all images [109]. The terms *matching* and *registration* are both used to denote the process that determines a transformation that relates one image to another. Finding a geometric transformation is generally the key to the registration problem. The term image refers to a two-dimensional light-intensity function, denoted by $f(x,y)$, where the value of f at spatial coordinates (x,y) gives the intensity (brightness) of the image at that point. An image is normally approximated by a discrete two-dimensional array of size $m \times n$, where $0 \le x < m$ and $0 \le y < n$. Each element of the array is referred to as a *pixel.* For two images R and D, representing the reference and distorted images respectively, $R(u,v)$ and $D(x,y)$ represent the gray-scale intensities at the coordinates (u,v) and (x,y) respectively. The relationship between the reference image and the distorted and *transformed* images is shown below in Figure 2-1, where the coordinates of the *transformed* image are represented by (x',y').

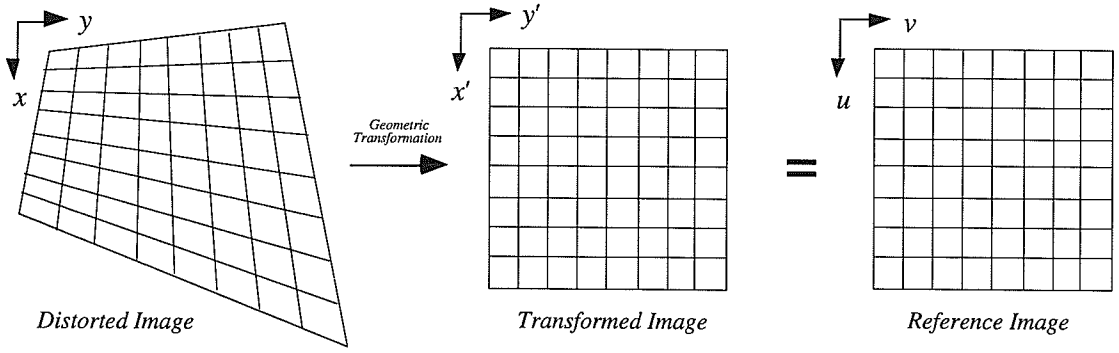

Figure 2-1. The relationship between the *Reference* Image and the *Distorted* Image

The registration of the distorted image with respect to the reference image is expressed through a transformation function T by an equation of the form:

$$(u,v) = T[(x,y)] \rightarrow (x',y') \tag{2.1}$$

Registration can be performed in any number of dimensions. A one-dimensional method may perform a temporal match on a time series of spatially consistent images. In two-dimensional methods, projection images or tomographic slices of different modalities are aligned, assuming that the images are made exactly in the same plane relative to the patient. Three-dimensional methods consider a tomographic image as a volumetric data set rather than a set of individual slices, that can be registered with another (2D or 3D) image. For example, the matching of a 2D projection image such as DSA (digital subtraction angiography) with a 3D tomographic image. The methods considered here will focus on two-dimensional registration. Any registration method will produce a set of functions that transform the coordinates of each point in one image into the coordinates of the corresponding point in the other image.

2.3 Categories of Registration Problems

The four general categories of registration problems outlined by Brown [13], namely multimodal, template, temporal, and viewpoint have been supplemented with the inclusion of monomodal matching problems. Registration problems are by no means limited to this categorization scheme. Many problems are combinations of these five classes of problems; for example, images are frequently taken from different modalities at different times.

2.3.1 Multimodal

Multimodal registration is the registration of medical images of the same scene acquired from different modalities. It is often used in the detection of functional abnormalities within anatomic structures. This requires matching a functional image (PET/SPECT) to the corresponding anatomical image (MRI/CT). It is also used to integrate different kinds of anatomic information. For example, CT images of skeletal structures can be overlaid with MR images of soft-tissue anatomy.

2.3.2 Template

Template registration is the registration of an image from one modality with a reference or "atlas" image from another modality. For example, some MR images exist in the form of a neuro-anatomical atlas [33,49] , with regions corresponding to gray matter, white matter, cerebrospinal fluid and scalp. This brain "atlas" is transformed to fit a given SPECT image of the brain in a functional/anatomical mapping.

2.3.3 Temporal

The registration of images of the same scene taken at different times is known as temporal registration. It is often used to detect and monitor changes caused by disease. For example, in ophthalmology, retinal images taken at different times over a period of years are used to detect slow changes in the retina, such as nerve fibre layer damage, optic disk cupping and pallor and intraocular tumors [80]. Alternatively, images may be taken only a fraction of a second apart, as in measuring dilution curves in fluorescein angiography.

2.3.4 Viewpoint

Viewpoint registration is the registration of medical images of the same scene taken from differing viewpoints. For example, the comparison of psoriasitic lesions [48] requires the use of digitized photographic images which often contain distortion due to the differing position of the photographic lens.

2.3.5 Monomodal

The registration of medical images from the same modality is known as monomodal registration. For example in magnetic resonance imaging, monomodal registration would be used to remove geometric distortion produced by non-linearity of the gradient fields. Non-linearity of the gradient along the slice-section direction tends to warp the planes causing a "potato chip" effect [65,103].

2.4 Registration Techniques

There have been a number of approaches to the alignment of medical images, including the transformation of images based on point-matching or statistical methods. The latter includes methods using moments/principal axes and correlation methods. These statistical registration techniques do not include gray level transformations. This is important in the registration of images of the same modality. For example in registering photographic images, correction must be allowed for differences in exposure time and brightness. In multimodality image registration, however, corresponding points can have very different gray values due to the nature of the different imaging modalities. Registration techniques can be classified into four categories. There are four major categories of registration techniques, namely

correlation matching, moments/principal axes matching, elastic matching and point-matching.

2.4.1 Correlation Methods

A *correlation* method involves a statistical approach to image registration [13,53,84] based on maximizing the correlation between two images and is therefore an approximation method. It gives a measure of the degree of similarity between two images. The images $R(u,v)$ and $D(x,y)$ represent the two images to be registered, where $R(u,v)$, of size U×V, is considered to be the reference image and $T(x,y)$ denotes a X×Y template region extracted from $D(x,y)$, the distorted image, where it is assumed X≤U and Y≤V. The normalized cross-correlation between the image pair is defined as

$$C(m,n)=\frac{\sum_{i=0}^{X-1}\sum_{j=0}^{Y-1}T(i,j)R(i+m,j+n)}{\left[j\sum_{i=0}^{X-1}\sum_{y=0}^{Y-1}R(i+m,j+n)^2\right]^{\frac{1}{2}}} \tag{2.2}$$

In Equation (2.2), $m=0,1,\ldots,M$ and $n=0,1,\ldots,N$ where $M=U-X$ and $N=V-Y$. For any value of *(m,n)*, Equation (2.1) yields one value of *C*. As *m* and *n* are varied, *T(x,y)* moves around the image area, giving the function *C(m,n)*. The maximum value of *C(m,n)* indicates the position where *T(x,y)* best matches $R(u,v)$. A related measure, is the correlation coefficient:

$$\gamma(m,n) = \frac{\sum_{i=0}^{X-1}\sum_{j=0}^{Y-1}[T(i,j)-\mu_T)(R(i+m,j+n)-\mu_R]}{\left[\sum_{i=0}^{X-1}\sum_{j=0}^{Y-1}(T(i,j)-\mu_T)^2\sum_{i=0}^{X-1}\sum_{j=0}^{Y-1}(R(i+m,j+n)-\mu_R)^2\right]^{\frac{1}{2}}} \tag{2.3}$$

In Equation (2.3), $m = 0,1,...,M$ and $n = 0,1,...,N$ where $M = U - X$ and $N = V - Y$, μ_T is the mean of the sub-image template and μ_R is the mean of the region coincident with the current location of T. The correlation coefficient $\gamma(m,n)$ is scaled in the range [-1,1] and the closer γ is to 1, the more similar the two images are. This method of gray value correlation is generally not useful for multimodal image registration as pixel intensities vary in differing modalities.

The general correlation concept for translational registration can be generalized, in principle, to accommodate changes in rotation. If an image contains arbitrary rotation angle, θ_r looking for the best match requires rotating $T(x,y)$ by some set of angles $\theta_1 \le \theta_r \le \theta_R$ until it aligns itself with $R(u,v)$. This method however, requires a significant amount of computation because of the need to transform $T(x,y)$ for each sample rotation angle θ_r. Junck, *et al.*, [53] allow rotations and translations in their correlation method for alignment of functional brain images.

2.4.2 Moments/Principal Axes Methods

A frequently used approach to image registration is based on *moments* matching techniques [34,51,105,112]. Moment functions can be used to derive the affine transformation between two images. General moments of the gray value function $f(x,y)$ are of the form:

$$m_{pq} = \sum_x \sum_y x^p y^q f(x,y) \tag{2.4}$$

When moments are related to the centroid of an image, they are often referred to as central moments. Central moments are invariant under translation. The central moments can be expressed by the equation:

$$\mu_{pq} = \sum_x \sum_y (x - \bar{x})^p (y - \bar{y})^q f(x,y) \tag{2.5}$$

In Equation (2.5), $\bar{x} = \frac{m_{10}}{m_{00}}$ and $\bar{y} = \frac{m_{01}}{m_{00}}$ define the centroid of an image. The centroid, called the "center of mass" is the balance point of the image function *f(x,y)* such that the mass of *f(x,y)* left and right of $\bar{x}$ and above and below $\bar{y}$ is equal. The central moments μ_{pq} defined in Equation (2.4) can also be expressed in terms of the moments m_{pq} defined in Equation (2.3). A moment can be normalized with the zero-order (*p=q=0*) moments so that it is invariant to changes in scale. Normalized central moments denoted η_{pq} are defined as:

$$\eta_{pq} = \frac{\mu_{pq}}{\mu_{00}^{\gamma}} \qquad \gamma = (p+q+2)/2 \tag{2.6}$$

Hu [41,84] has derived moments that are invariant with respect to the rotation of an image. From the second- and third-order normalized central moments, a set of seven moments invariant to changes in translation, rotation and scaling have been derived:

$$\begin{aligned}
\phi_1 &= \eta_{20} + \eta_{02} \\
\phi_2 &= (\eta_{20} - \eta_{02})^2 + 4\eta_{11}^2 \\
\phi_3 &= (\eta_{30} - 3\eta_{12})^2 + (3\eta_{21} - \eta_{03})^2 \\
\phi_4 &= (\eta_{30} + \eta_{12})^2 + (\eta_{03} + \eta_{21})^2 \\
\phi_5 &= (\eta_{30} - 3\eta_{12})(\eta_{30} + \eta_{12})\left[(\eta_{30} + \eta_{12})^2 - 3(\eta_{03} + \eta_{21})^2\right] + (3\eta_{21} - \eta_{03})(\eta_{03} + \eta_{21})\left[3(\eta_{30} + \eta_{12})^2 - (\eta_{03} + \eta_{21})^2\right] \\
\phi_6 &= (\eta_{20} - \eta_{02})\left[(\eta_{30} + \eta_{12})^2 - (\eta_{03} + \eta_{21})^2\right] + 4\eta_{11}(\eta_{30} + \eta_{12})(\eta_{03} + \eta_{21}) \\
\phi_7 &= (3\eta_{21} - \eta_{03})(\eta_{30} + \eta_{12})\left[(\eta_{30} + \eta_{12})^2 - 3(\eta_{03} + \eta_{21})^2\right] - (\eta_{30} - 3\eta_{12})(\eta_{21} + \eta_{03})\left[3(\eta_{30} + \eta_{12})^2 - (\eta_{03} + \eta_{21})^2\right]
\end{aligned} \tag{2.7}$$

Goshtasby [41] uses these normalized invariant moments together with circular templates to register two images in a similar way to correlation methods. Flusser and Suk [28] have derived a new set of moment invariants, that are invariant under a general affine or low-degree polynomial transformation. Moments matching techniques produce approximating transformations because they are based on statistical principals.

If two images are similarly shaped, they may be registered approximately by matching their *principal axes* [2]. The principal axes of an image are those orthogonal axes about which the moments of inertia are minimized [24]. Therefore the principal axes of two different images can be used to calculate the affine transformation between the two images. Two images may be related rotationally by their principal axes and translationally by their centroids. To be related in scale, the relative magnitudes of the principal axes must be determined. The Hough transform is used by Cideciyan and Nagel [18] to calculate the best fitting ellipse in two-dimensional brain images, from which the transformation relating the principal axes of the ellipses can be determined.

2.4.3 Point Matching Methods

This technique registers two images by finding a transformation to represent the relationship between corresponding point features or "control-points" within the images. The point-matching method is the primary approach currently taken to register two images in which the source of distortion is unknown. The registration of multimodality images also relies on such methods due to the inability of statistical methods to register images containing differing radiometric (intensity) values. The general methodology associated with this method is outlined in Section 2.5. The

remaining chapters deal with the three major aspects relating to point-matching, namely, control-point selection, control-point matching and geometric transformation.

2.4.4 Elastic Matching Methods

An elastic matching method involves extracting and matching corresponding contours from two images [72,73,89]. This method, first introduced by Burr [15], models the distortion in an image as the deformation of an elastic body. The similarity between points in the two images act as external forces which "stretch" the body. Contour matching is performed on all corresponding contour pairs, and results in correspondence along the contours. These represent local displacement vectors. A two-stage transformation is calculated from these vectors. A global image shift is first determined from these vectors and then the residual vectors, which represent local non-linear distortions along the contours are calculated.

Distortion vectors in the image are approximated by interpolating the residual vectors onto the whole image. A mean weighting interpolation function is used, where the weighting function decreases asymptotically to zero for large distances. The distortion vectors are then applied to the deformed image to correct for the deformation. The general elastic transformation is defined by:

$$T[(x,y)] \rightarrow (x',y') \tag{2.8}$$

In Equation (2.8), $x' = x + a$ and $y' = y + b$ where a and b represent displacements in the elastic plane. Tang and Suen [104] introduce three models for elastic transformation including general, semi-elastic and complete elastic models. Lin and Huang [62], use an "elastic" mapping algorithm to match tomographic images.

2.5 Methodology

Numerous point-matching registration techniques have been proposed [13,43,112] from which the following general four-step methodology [34] can be defined:

1. Select points from each image. These are known as the *control points*.
2. Establish a correspondence between the points from both images. The corresponding points are called control-point pairs.
3. Determine a mapping function using the known control points.
4. Geometrically align the two images by means of the mapping function.

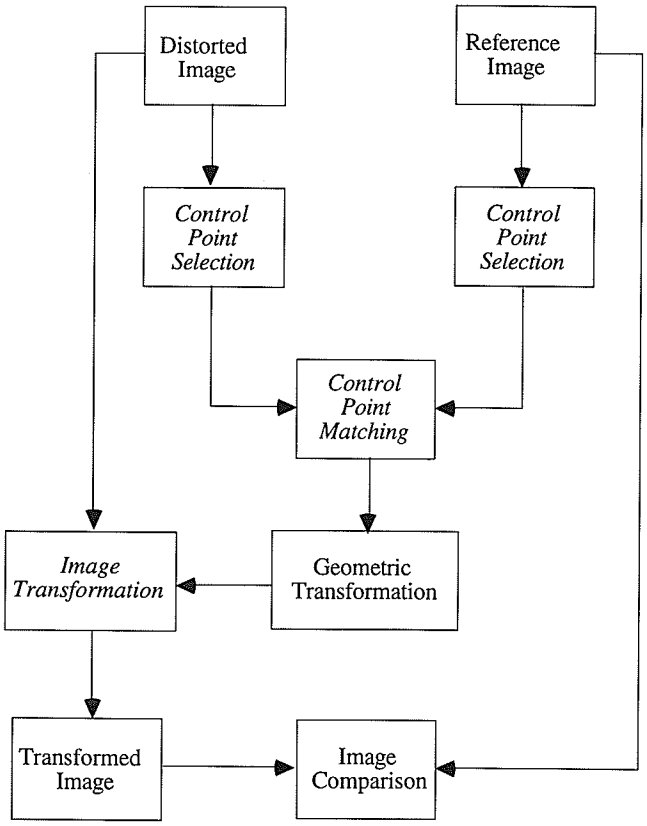

Figure 2-2. General Schema for a Point-Matching Method

This general methodology is illustrated in Figure 2-2, showing the entire process involved with registering two images.

2.6 Image Distortion

When selecting a transformation method it is important to consider the source of misregistration in an image. The source of misregistration is the cause of the distortion between images. *Distortion* in an image is the amount of geometrical displacement suffered by a pixel when compared to its correct location. Distortion is often characterized by a two-dimensional map of the observed distorted grid with respect to a perfectly generated grid. Distortions contained in medical images may be the result of a modality dependent image distortion (e.g., section thickness, pixel size), sensor deviations (e.g., distortions in MR images are due to inhomogeneities in the magnetic field and non-linearities in the gradients), elasticity of body parts or movement of organs.

Two major types of distortion are distinguished. The first type is the source of misalignment between two images. The second type of distortion are those which are not the source of misregistration, and may be the result of radiometric distortion (differing intensity values) between multiple modalities or natural changes such as the movement or *deformation* of features within the image. Since a common objective of registration is to detect a change between two images, it is important that images are matched only with respect to the misregistration source, otherwise the change of interest will be removed at the same time. Distortion can be classified as both linear/geometric and local/global.

2.6.1 Linear Distortion

Linear distortion causes an image to be geometrically similar to the original, yet contain some form of linear difference. Linear distortions are usually in the form of affine differences in the images such as rotation, translation, scaling and shearing. Figure 2-3 shows three forms of linear distortion. Both Figures 2-3(a) and 2-3(b) depict a 75% compression of the chest image in Figure 1-2, in the horizontal and vertical directions respectively, while Figure 2-3(c) depicts a 23° rotational distortion.

(a) (b)

(c)

Figure 2-3. Examples of Linear Distortion
(a) Horizontal Scaling, (b) Vertical Scaling, (c) 23° Rotation

2.6.2 Geometric Distortion

Geometric, or non-linear distortion is an aberration that causes an image to be geometrically dissimilar to the original image. Such distortions are usually in the form of image skew or warping. Some geometric distortions apparent in medical images may be due to variations in patient positioning. For example, the actual orientations of "transverse" CT and MR tomographs usually differ 10°-20°, and the section centres may be positioned quite differently in relation to the patient's anatomy.

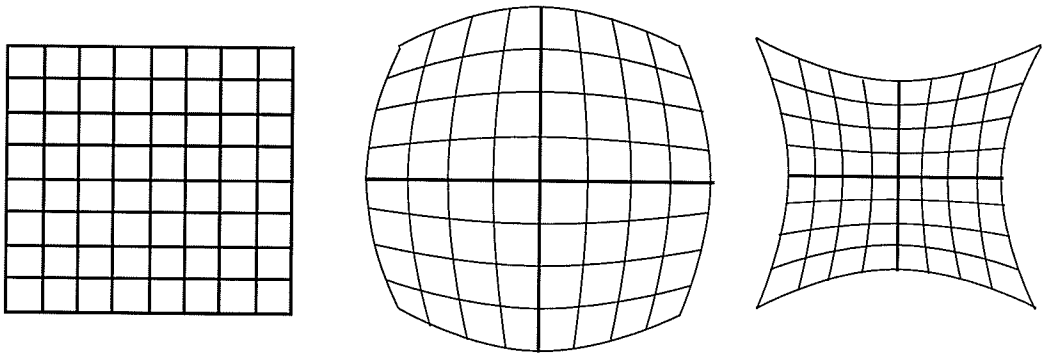

Figure 2-4. Examples of Geometric Distortion
(a) Original, (b) Barrel, (c) Pincushion

Photometric distortions are a form of geometric distortion usually caused by sensor deviations and imperfections. The most obvious photometric distortions can be observed as *barrel* (convex) or *pin-cushion* (concave) shaped images, as shown above in Figure 2-4(b) and 2-4(c) respectively.

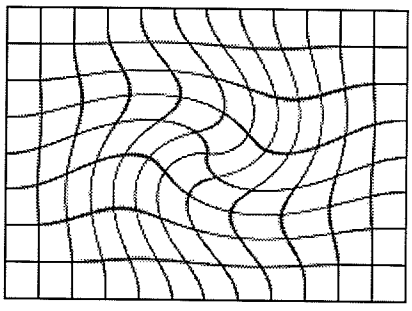

Figure 2-5. Grid or "rubber sheet" Distortion

The distortion contained in an image can often be modelled as rubber sheets or grids, as shown in Figure 2-5.

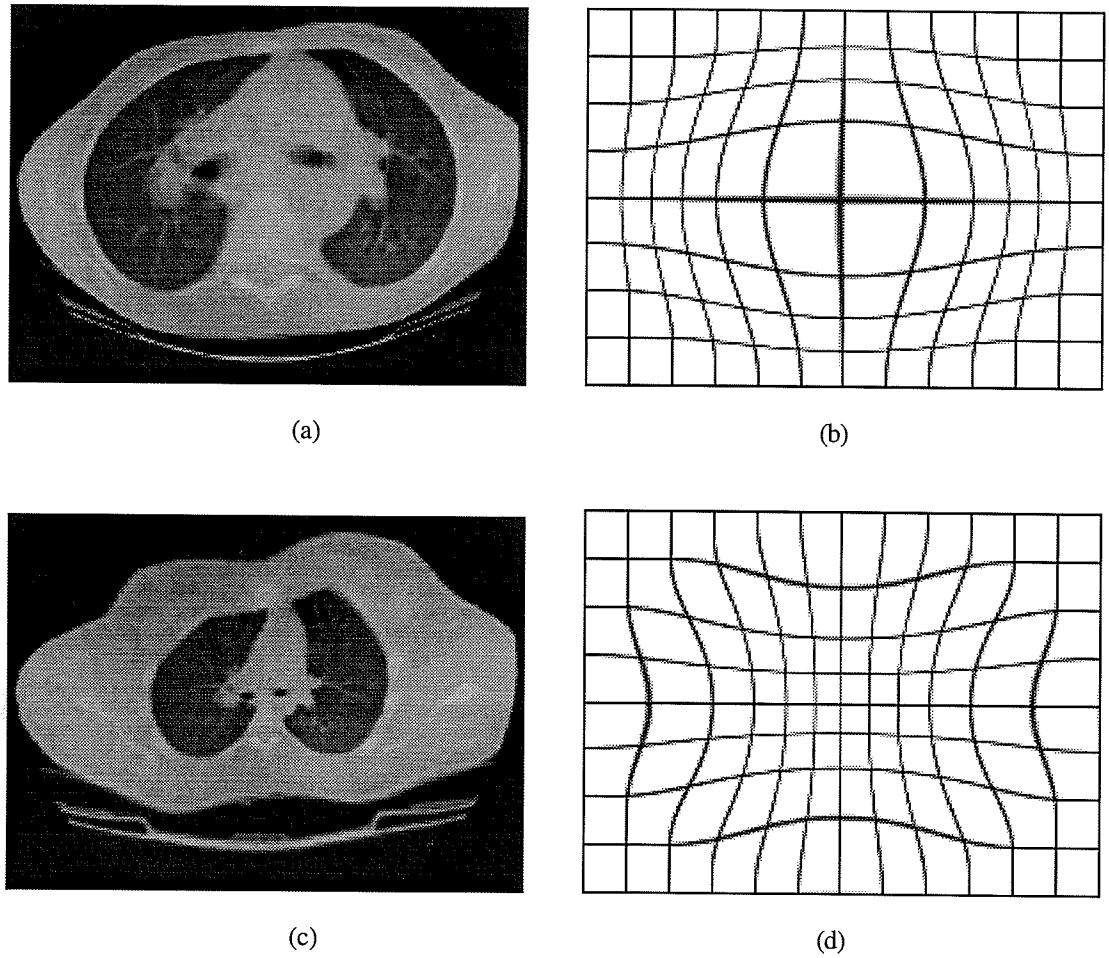

(a) (b)

(c) (d)

Figure 2-6. Examples of Geometric Distortion and their respective Distortion Grids
(a,b) Barrel, (c,d) Pincushion

Both Figures 2-6 and 2-7 show examples of geometric distortion and their associated distortion grids. Figures 2-6(a) and 2-6(c) are barrel and pincushion photometric distortions of Figure 1-2. Figures 2-7(a) and 2-7(c) are forms of geometric distortion known as *radial* distortion.

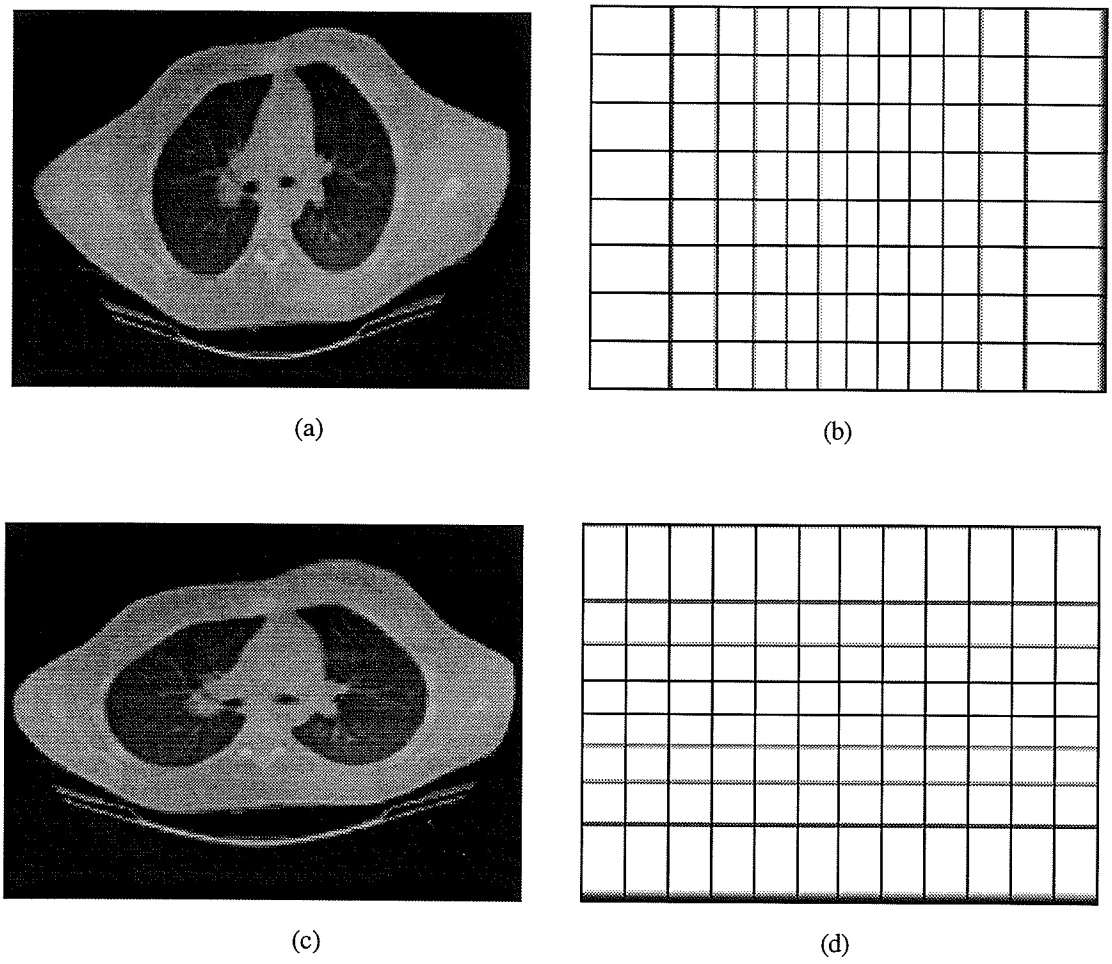

Figure 2-7. Examples of Radial Distortion and their respective Distortion Grids
(c,d) Horizontal Distortion (e,f) Vertical Distortion

2.6.3 Local/Global Distortion

The distortion that deforms an image can be either global or local. In a *local* distortion, a linear or geometric distortion influences only part of the image. Therefore different parts of an image may exhibit differing kinds of distortion. A distortion is called *global* when the whole image is influenced by the same form of distortion. Examples of global and local distortions are shown below in Figure 2-8 (a) and 2-8(b) respectively.

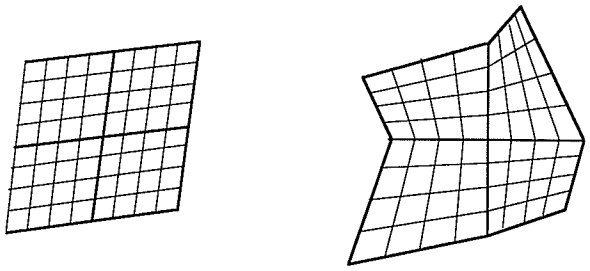

(a) (b)

Figure 2-8. Global/Local Distortion: (a) Global , (b) Local

There is a distinct correlation between the distortions contained within the image and the registration method used. In general, images that contain linear distortion are registered with either an affine or low (first or second) degree polynomial transformation, while images which contain non-linear or geometric distortion are registered using a 3rd- or 4th-degree polynomial or surface-spline transformation. It is assumed that the kind of transformation used in registration is adequate to describe the actual distortion. These techniques are described in Chapter 5.

Chapter 3

Control-Point Selection

3.1 Introduction

The first step in the registration of two images is the selection of control-points from each of the images. There are three steps involved in the selection of control points from an image. The first step involves the extraction of primary features from an image by means of image segmentation. The second step involves deriving secondary features from the primary features and the third step involves finding control points from within the secondary features. This chapter is divided into six sections. Section 3.2 discusses the concept of a control point and its association with medical images. The general methodology which has been proposed is discussed in Section 3.3. Methods of feature extraction are outlined in Section 3.4 and Section 3.5 outlines the kinds of significant points related to secondary features and briefly describes various significant point detection methods including both polygonal approximation and angle detection. Finally Section 3.6 integrates the methods of Sections 3.4 and 3.5.

3.2 Control-Points

A control point, sometimes known as a "dominant" point is an identifiable point selected from an image. Control points can be either intrinsic or extrinsic [13]. *Extrinsic* control points are markers on the image placed specifically for the purpose of image matching. In medical images, fiducial chemical markers are widely used; these are identifiable structures placed in known positions such as plastic "N" shaped tubing filled with a paramagnetic compound (e.g. $CuSO_4$) [64] visible with magnetic resonance (MR) or a γ-emitting radioisotope (e.g. $Na^{99m}TcO_4$) visible with SPECT although agents appropriate for other modalities (e.g. CT, PET) may also be used. Other markers from which control points can be obtained may include stereotactic frames, a reference frame usually used in obtaining neurological images (e.g. lesion biopsies) and skin markers (e.g. radiopaque markers). Materials administered to the patient for diagnostic purposes are considered extrinsic. Examples of these are radiopharmaceuticals for SPECT and contrast media for angiograms [112]. There are a number of disadvantages associated with the use of extrinsic control points. Although external markers attached to the patient's skin have been used to register nuclear medicine images to MR or CT images [88], they are not sufficiently accurate for registering CT and MR images to each other because of skin movement. There are not always extrinsic points that can be used, such as in the case of internal diagnostic images. Extrinsic points are less suited for matching, for example, internally deforming parts of the body, such as the abdomen. A more flexible approach to control point selection is to use anatomical features [50] visible in each image, rather than extrinsic features such as external markers or frames to achieve registration. Such control points are *intrinsic*. Various anatomical features have been proposed as control points for registering medical images. The points may exist as

geometric points such as corners, line intersections, curvature extrema (maxima and minima), curvature discontinuities or shape points such as centroids. Nuclear medicine images contain very limited anatomical information. As a result, image registration techniques based on the use of anatomical features are of little use with such images and there external fiducial markers attached to the skin surface are often used.

3.3 Methodology

The generalized control-point selection methodology can be described by the following three-steps, which is shown diagramatically in Figure 3-1.

1. Primary features are selected from the two images. This is usually achieved through segmentation techniques such as edge detection and thresholding, which may be preceded by an image enhancement technique to attenuate features within an image.

2. Secondary features are extracted from the primary features. These usually take the form of straight lines, curves and corners.

3. A set of uniquely identifiable points, known as control points are selected from the secondary features. These may take the form of corners, line intersections, end-points, and curvature points such as maxima and minima, points of inflection and discontinuities in curvature.

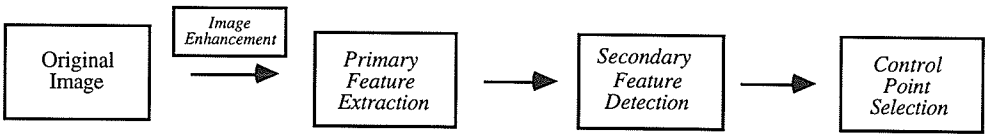

Figure 3-1. General Schema for Control Point Selection

3.4 Feature Extraction

A key problem in the selection of control-points is the extraction of meaningful features from images. This is especially difficult with certain types of medical images due to their lack of distinct features. Methods of feature extraction from a medical image vary according to the imaging modality and the content of the image. Two methods used to extract features are image segmentation and image enhancement. Image Segmentation is commonly associated with the extraction of primary features. Figure 3-2 shows the general schema for feature extraction.

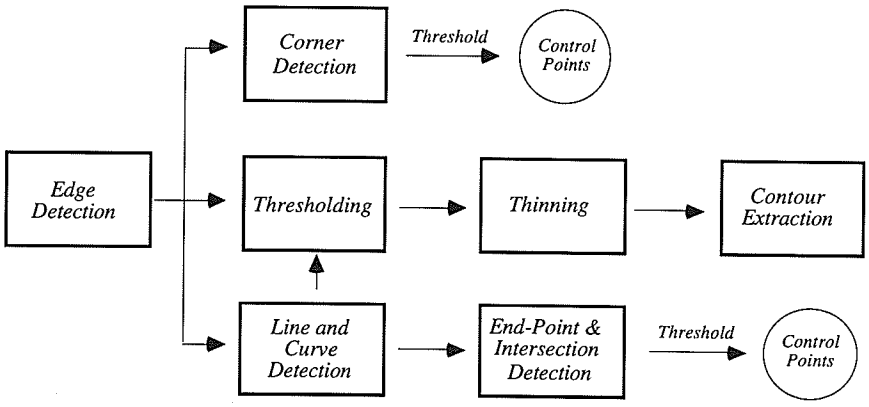

Figure 3-2. General Schema for Feature Extraction

3.4.1 Preliminaries

The discussion on feature extraction techniques focuses on grayscale images, typically composed of 256 differing intensities of gray (zero intensity to maximum intensity), associated with 8-bit digital images [46]. The term *pixel* refers to a point on the 2-D grid of an image, and has an intensity value associated with it. This preliminary discussion focuses on two related concepts associated with images, namely, an image region and an image mask. An image *mask*, like that shown in Figure 3-3(b), usually consists of an $n \times n$ (where n is odd) template containing specific weights at each position $p(i,j)$ which are used to transform a region of an image. An *image region* is the corresponding $n \times n$ region of an image.

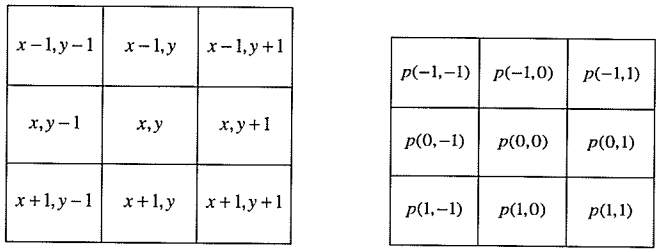

Figure 3-3. (a) A 3x3 Image Region (b) A general 3x3 mask

In general, the result of the mask shown in Figure 3-3(b) on a 3×3 image region, as shown in Figure 3-3(a) is defined as:

$$g(x,y) = \sum_{i=-1}^{1} \sum_{j=-1}^{1} f(x+i, y+j) p(i,j) \tag{3.1}$$

In Equation (3.1), $f(x+i, y+j)$ is the gray level of the pixel associated with the mask coefficient at position $p(i,j)$. The result of the mask is defined with respect to

its centre location *(x,y)*. When a mask is centred on a boundary pixel, the result is derived using the appropriate partial neighborhood of the mask, which is normalized.

3.4.2 Image Enhancement

Medical images always contain some form of noise. Noise becomes a problem when performing edge detection because it may result in the improper detection of an edge. Regardless of the kind of filter used, the basic approach is to sum the products between the mask coefficients and the gray levels of the points under the mask at a specific location in the image. Any combination of the three filters discussed below can be employed.

3.4.2.1 Low Pass Filters

A low-pass filter attenuates or eliminates high-frequency components in an image, while leaving the low-frequency components intact. Low-pass filters are commonly used to reduce the noise in an image. For a 3×3 filter, the simplest form is a mask in which all coefficients have a value of $\frac{1}{9}$, such that the sum of the mask coefficients is 1. The use of a masks of the form shown in Figure 3-4 is often referred to as neighborhood averaging. The gray level of each pixel is replaced by the average of the gray levels in the neighborhood of that pixel.

$\frac{1}{9}$	$\frac{1}{9}$	$\frac{1}{9}$
$\frac{1}{9}$	$\frac{1}{9}$	$\frac{1}{9}$
$\frac{1}{9}$	$\frac{1}{9}$	$\frac{1}{9}$

$1/25$	$1/25$	$1/25$	$1/25$	$1/25$
$1/25$	$1/25$	$1/25$	$1/25$	$1/25$
$1/25$	$1/25$	$1/25$	$1/25$	$1/25$
$1/25$	$1/25$	$1/25$	$1/25$	$1/25$
$1/25$	$1/25$	$1/25$	$1/25$	$1/25$

Figure 3-4. 3x3 and 5x5 Low-Pass Masks

For a 3×3 region, the averaging function is of the form shown below in Equation (3.2).

$$g(x,y) = \frac{1}{9}\sum_{i=-1}^{1}\sum_{j=-1}^{1} f(x+i, y+j) \tag{3.2}$$

3.4.2.2 Median Filters

The median filter is an enhancement technique used to reduce noise while preserving the edge structure of an image. This filter smoothes ragged edge regions to eliminate false edge detection responses. The gray level of each pixel is replaced by the median of the gray levels in a neighborhood of that pixel, instead of by the mean. The median of a set of values, m, is that member of the set such that half the values in the set are less than m and half are greater than m [36]. For example, in a 3x3 neighborhood, the median is the 5th largest value.

3.4.2.3 High Pass Filters

High pass filters attenuate or eliminate low-frequency components in an image. They are used to deblur or sharpen images. A high pass filter should have positive coefficients near its centre, and negative coefficients in the outer periphery. Figure 3-5 shows two classic implementations of a 3x3 mask [36]. Note that the sum of coefficients is 1.

−1	−1	−1
−1	9	−1
−1	−1	−1

1	−2	1
−2	5	−2
1	−2	1

Figure 3-5. Sample 3x3 High-Pass Masks

When the mask is over an area in the image, of constant or slowly varying gray level, the resulting mask operation doesn't change the image very much.

3.4.3 Image Segmentation

Descriptions of an image generally refer to significant parts (regions, curves, lines) of which the image is composed. Image segmentation is the division of an image into different regions, each having certain properties [32]. Segmentation is based on the two fundamental properties related to gray-level images: discontinuity and similarity [36]. Segmentation techniques can be categorized into three classes:

(1) thresholding

(2) edge detection

(3) region extraction

The extraction of primary features from medical images will focus primarily on the use of edge detection and thresholding or a combination of the two methods. Region extraction is a technique used to divide an image into regions. A region is an area of an image whose points have a common property. It usually consists of region merging, region dividing or a combination of the two. A survey of region extraction techniques can be found in Zucker [123] and Davis *et al.* [23]. Image segmentation has been used on biomedical images for such purposes as the identification of lung diseases and detection of cancerous cells [32] and tissue classification [61]. The method of segmentation employed depends on the kind of image. A review of image segmentation techniques can be found in Haralick and Shapiro [45] and Fu and Mui [32].

3.4.4 Grayscale Edge Detection

Edge detection is an image segmentation technique based on the detection of discontinuity. Edges may arise from a variety of discontinuities in an image: occluding edges are discontinuities in range; convex or concave edges are discontinuities in surface slope; shadow edges are discontinuities in illumination [93]. Edge detection produces edge points which may describe a feature. In a grayscale image, an edge corresponds to changes in gray level. These changes can take several forms [84]; as shown by Figure 3-6. The first form (Figure 3-6(a)) occurs when the gray levels differ between two adjacent regions, but are consistent within a region. This is known as a *step edge*.

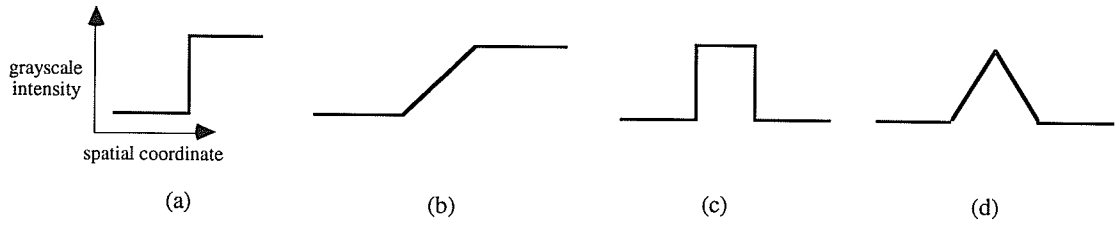

Figure 3-6. Edges: (a) step edge, (b) ramp edge, (c) spike edge, (d) roof edge

If the grayscale change occurs over a greater area, it is referred to as a *ramp edge* (Figure 3-6(b)). Alternatively this change may take the form of a line or curve, where gray levels are relatively constant within an area except for a thin strip which differs significantly. Such an edge is called a *spike edge* (Figure 3-6(c)). If the grayscale change occurs over a wider area, it is called a *roof edge* (Figure 3-6(d)). There are two major classes of differential edge detection: first-order derivative (gradient) and second-order derivative (Laplacian).

3.4.4.1 Gradient Edge Detection

A common method used for edge detection is the *gradient* [22,36]. This approach uses first derivatives in two or more directions, such as horizontal, vertical or diagonal. The gradient vector G of a function $f(x,y)$ is defined as:

$$G[f(x,y)] = \begin{bmatrix} f_x(x,y) \\ f_y(x,y) \end{bmatrix} \tag{3.3}$$

where $f_x(x,y) = \frac{\partial f}{\partial x}$ *and* $f_y(x,y) = \frac{\partial f}{\partial y}$ are the partial derivatives of f taken in any pair of perpendicular directions. The quantities f_y and f_x represent the row and column gradients respectively. The gradient is a vector function whose direction at a given point is the direction of maximum rate of change of the function at that point and whose magnitude is the rate of change in that direction. The equation used to determine the gradient magnitude, denoted by G_M, is given by the square root of the sum of squares of f_x and f_y shown below in Equation (3.4).

$$G_M(x,y) = \left[f_x(x,y)^2 + f_y(x,y)^2 \right]^{\frac{1}{2}} \tag{3.4}$$

Common practice is to approximate the magnitude of the gradient with absolute values as shown in Equation (3.5).

$$G_M(x,y) \approx \left| f_x(x,y) \right| + \left| f_y(x,y) \right| \tag{3.5}$$

The gradient direction, denoted by G_D, is given by the inverse tangent of the ratio of f_y and f_x (Equation (3.6)).

$$G_D(x,y) = \arctan\left(f_y(x,y) / f_x(x,y) \right) \tag{3.6}$$

Quite a few proposed edge detection techniques are based on variations of Equation (3.4), which produce a high magnitude where there is a significant change in gray level and a low magnitude where there is little change in gray level.

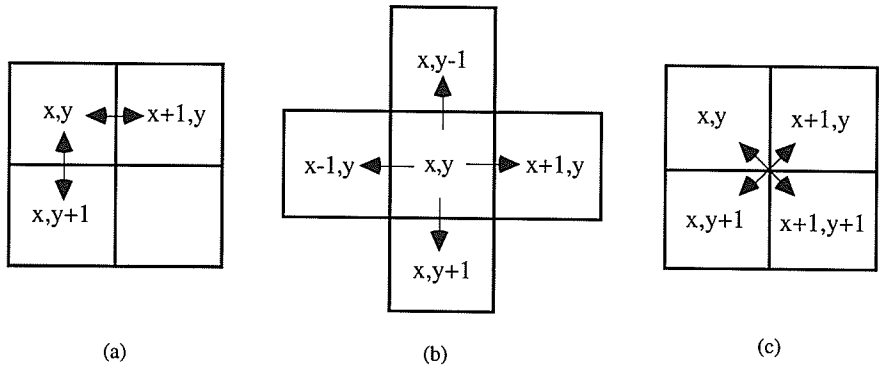

Figure 3-7. Gradients: (a) Non-Symmetric, (b) Symmetric, (c) Robert's Cross Gradient

The gradient vector components can be approximated with first differences (Figure 3-7(a)). The row and column gradients are approximated by Equations (3.7a) and (3.7b) respectively.

$$f_y(x,y) = f(x,y+1) - f(x,y) \tag{3.7a}$$

$$f_x(x,y) = f(x+1,y) - f(x,y) \tag{3.7b}$$

The disadvantage of this method is that the differences are not symmetric with respect to *(x,y)*. They are instead centred at $(x+1/2, y)$ and $(x, y+1/2)$ respectively (See Figure 3-7(a)). This can be avoided using the row and column gradients as approximated by Equation (3.8a) and (3.8b) respectively.

$$f_y(x,y) = f(x,y+1) - f(x,y-1) \tag{3.8a}$$

$$f_x(x,y) = f(x+1,y) - f(x-1,y) \tag{3.8b}$$

which is symmetric about (x,y) as shown in Figure 3-7(b). Another approach to approximating Equation (3.3) is to use cross-differences (Figure 3-7(c)):

$$f_1(x,y) = f(x,y) - f(x+1,y+1) \tag{3.9a}$$

$$f_2(x,y) = f(x,y+1) - f(x+1,y) \tag{3.9b}$$

The gradient requires that there be a distinct change in intensity between two adjacent points, so only very sharp edges with high contrast between the surfaces which form the edges will be detected. The magnitude is therefore defined as Equation (3.10) whilst the gradient direction is given by Equation (3.11).

$$G_M(x,y) = \left[f_1(x,y)^2 + f_2(x,y)^2\right]^{\frac{1}{2}} \tag{3.10}$$

$$G_D(x,y) = \arctan\left(\frac{f_2(x,y)}{f_1(x,y)}\right) \tag{3.11}$$

Equations (3.10) and (3.11) can be implemented using masks of size 2x2 as shown in Figure 3-8. These masks are called the Robert's Cross-Gradient operators. They are symmetric about $(x+1/2, y+1/2)$.

1	0
0	−1

0	1
−1	0

Figure 3-8. Roberts Cross-Gradient Mask

Sobel, Prewitt, and Frei and Chen [84] propose gradients which are based on a 3×3 neighborhood. The main difference among these three methods are the weights assigned to each element of the 3×3 mask. The row and column gradients are defined by Equations (3.12a) and (3.12b) respectively.

$$f_y(x,y) = [f(x-1,y+1) + Kf(x,y+1) + f(x+1,y+1)] - [f(x-1,y-1) + Kf(x,y-1) + f(x+1,y-1)] \quad (3.12a)$$

$$f_x(x,y) = [f(x+1,y-1) + Kf(x+1,y) + f(x+1,y+1)] - [f(x-1,y-1) + Kf(x-1,y) + f(x-1,y+1)] \quad (3.12b)$$

where the coefficient K defines the weight. Prewitt uses Equation (3.12) with K=1. Sobel uses K=2 to weigh each pixel with respect to its spatial gradient. Frei and Chen use weights of $K = \sqrt{2}$ so that the gradient is the same for horizontal, vertical and diagonal edges. The Prewitt operator is more sensitive to horizontal and vertical edges than diagonal edges; the reverse is true for the Sobel operator.

−1	0	1
−2	0	2
−1	0	1

−1	−2	−1
0	0	0
1	2	1

(a)

−1	0	1
−1	0	1
−1	0	1

−1	−1	−1
0	0	0
1	1	1

(b)

−1	0	1
$-\sqrt{2}$	0	$\sqrt{2}$
−1	0	1

−1	$-\sqrt{2}$	−1
0	0	0
1	$\sqrt{2}$	1

(c)

Figure 3-9. 3×3 Gradient Operator Masks
(a) Sobel, (b) Prewitt , (c) Frei and Chen

Equation (3.12) is implemented using the masks shown in Figures 3-9(a), 3-9(b) and 3-9(c) representing the Sobel , Prewitt, and Frei and Chen operators respectively. The operators are implemented as two 3×3 masks which are perpendicular to each other. These operators can be extended to extract the edge gradient along the diagonal directions. Another approach is to determine gradients in a number of directions. Kirsh [84], proposed a directional template gradient in eight directions, defined by the mask shown below in Figure 3-10.

5	5	5
−3	0	−3
−3	−3	−3

Figure 3-10. 3×3 Kirsh Operator

Each clockwise circular shift of the elements, of the mask in Figure 3-10, about the centre rotates the gradient direction by 45°, giving eight masks. Therefore the magnitude of the gradient denoted $G_M(x,y)$ is defined by Equation (3.13)

$$G_M(x,y) = \underset{k=1}{\overset{8}{\mathrm{MAX}}}\left[\left|\sum_{i=-1}^{1}\sum_{j=-1}^{1} f(x+i,y+j)P_k(i,j)\right|\right] \qquad (3.13)$$

where the $P_k(i,j)$ represent the eight rotated masks derived in this manner. Figure 3-11(a) and 3-11(b) shown below are the results of the Sobel operator applied to the CT and MR chest images of Figure 1-8(a) and (b) respectively.

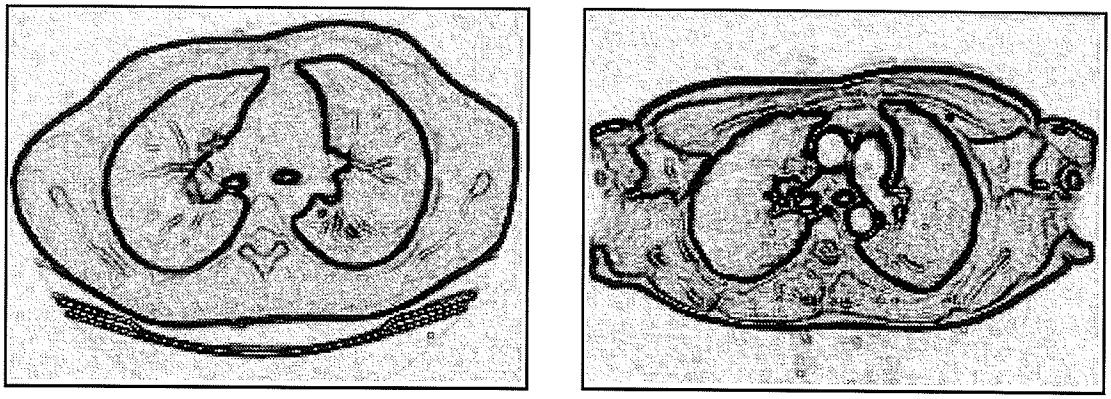

(a) (b)

Figure 3-11. Sobel Edge Detection of Figure 1-8 (a) CT and (b) MR Image

3.4.4.2 Laplacian Edge Enhancement

Laplacian edge enhancement is based on the Laplacian operator. The Laplacian L of a function $f(x,y)$ is the linear combination of second-order partial derivatives defined as:

$$L(f(x,y)) = \left(\frac{\partial^2 f}{\partial x^2} + \frac{\partial^2 f}{\partial y^2} \right) \tag{3.14}$$

For a discrete function the partial derivatives can be approximated by:

$$\frac{\partial^2 f}{\partial x^2} = f(x+1,y) - 2f(x,y) + f(x-1,y) \tag{3.15a}$$

$$\frac{\partial^2 f}{\partial y^2} = f(x,y+1) - 2f(x,y) + f(x,y-1) \tag{3.15b}$$

Therefore the Laplacian can be approximated by Equation (3.16).

$$g(x,y) = \{f(x-1,y) + f(x+1,y) + f(x,y-1) + f(x,y+1)\} - 4f(x,y) \tag{3.16}$$

Equation (3.16) can be expressed by the 3×3 mask shown in Figure 3-12(a). Figure 3-12(b) is another variation.

0	−1	0
−1	4	−1
0	−1	0

(a)

1	−2	1
−2	4	−2
1	−2	1

(b)

Figure 3-12. Laplacian Masks

The defining requirement of the Laplacian mask is that the coefficient associated with the point *(x,y)* is positive and the coefficients associated with its neighboring points be negative. An important attribute is that the sum of the coefficients is zero. This means $g(x,y)$ will be zero if $f(x,y)$ is of constant or linearly increasing pixel intensity. However the Laplacian has certain disadvantages, it produces double edges and is unable to detect edge direction.

3.4.5 Thresholding

Thresholding is a technique where all the pixels in an image f with N $(N>1)$ possible gray levels in the range $[G_{\min}, G_{\max}]$ are mapped into two levels, by some threshold function T. Therefore, all gray levels in a given range are mapped into one level (denoted, say, by gray level 1) and all others are mapped into another level (gray level 0) [118]. In a general , a threshold function T is of the form:

$$T(x, y, N(x, y), f(x, y))$$

where $f(x,y)$ is the gray level of the point (x,y) and $N(x,y)$ denotes some local property of the point (x,y), e.g. the average gray level over some neighborhood.

Weszka [118] divided thresholding into three classes, depending on the functional dependencies of the threshold function T. If T depends only on $f(x,y)$, the threshold is called *global*. If it depends on both $f(x,y)$ and $N(x,y)$ then the threshold is called *local*. If the function depends on the spatial values x and y as well as on $f(x,y)$ and $N(x,y)$ then the threshold is called *dynamic*. The simplest of all global thresholding techniques is to divide the image at a specified gray level t. This is known as *bilevel* thresholding. Given a gray level $t \in [G_{\min}, G_{\max}]$, each pixel (x,y) in the image is:

$$g(x,y) = \begin{cases} 1 & \text{if } f(x,y) > t \\ 0 & \text{if } f(x,y) \leq t \end{cases} \tag{3.17}$$

All gray levels greater than t are mapped into gray level 1 and all gray levels less than or equal to t are mapped into gray level 0. Thresholding can also be done with a range of gray levels:

$$g(x,y) = \begin{cases} 1 & \text{if } u \leq f(x,y) \leq v \\ 0 & \text{otherwise} \end{cases} \tag{3.18}$$

for given gray levels $u, v \in [G_{\min}, G_{\max}]$. A variation on thresholding is semi-thresholding. Gray levels below a threshold become 0, whilst all others are left unchanged. *Multilevel* thresholding uses a set of k thresholds $\{t_1, t_2, \ldots, t_k\}$ to threshold an image at differing levels (Equation 3.19).

$$g(x,y) = \begin{cases} 0 & \text{if } f(x,y) \leq t_1 \\ i & \text{if } t_i < f(x,y) \leq t_{i+1} \ (i = 1,..,k-1) \\ k & \text{if } f(x,y) > t_k \end{cases} \tag{3.19}$$

A survey of thresholding techniques for image segmentation can be found in Fu and Mui [32], Weszka [118] and Sahoo *et al.* [96]. Figure 3-13 shows the CT and MR images of Figure 1-8(a) and (b) respectively after thresholding.

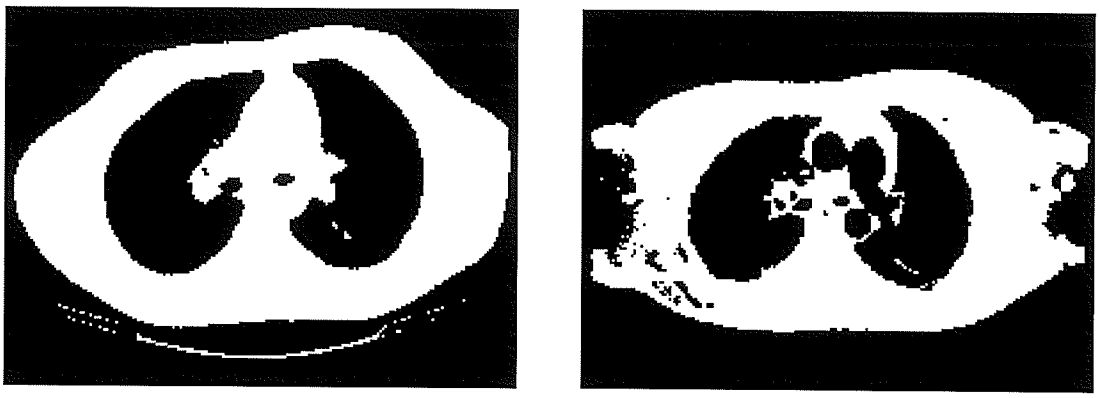

(a) (b)

Figure 3-13. Thresholding: (a) CT Image (b) MR Image of Figure 1-8

Both images have been thresholded using the bilevel thresholding technique of Equation (3.17), where t=145 for Figure 1-8(a) produced Figure 3-13(a), and t=180 for Figure 1-8(b) produced Figure 3-13(b).

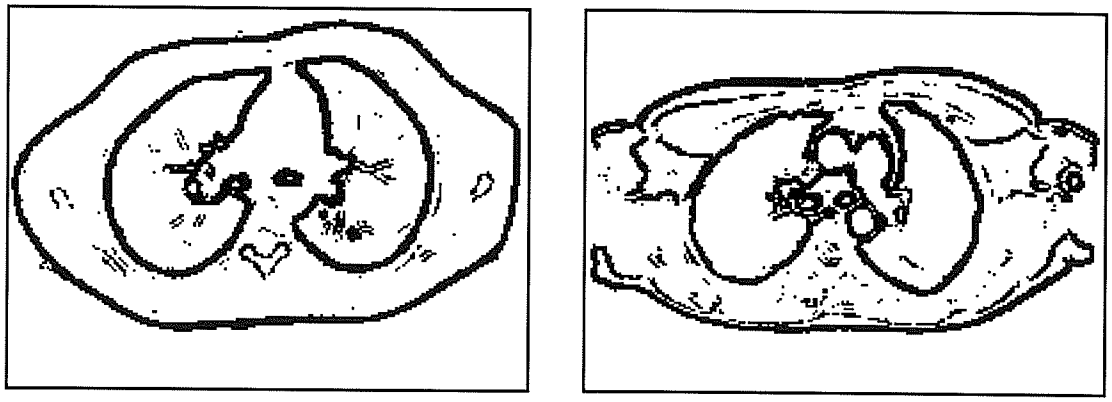

(a) (b)

Figure 3-14. Thresholding the Images of Figure 3-11 (a) and (b)

After the edge gradient is found using the edge detection methods of Section 3.4.3.1, the gradient is compared to a threshold to determine if an edge exists. Figure 3-14 shows the CT and MR images of Figure 3-11(a) and (b) after thresholding with t=100 and t=175 respectively.

3.4.6 Thinning

Once the edges within the image have been found and the image is converted into a binary image by thresholding, the features contained within the image are often reduced to thin lines, curves and points. This reduction may be accomplished by obtaining the skeleton of an image via a *thinning* (also called *skeletonizing*) algorithm [36]. This produces lines and curves which are one-pixel in width.

The reduction of an image to its essentials can eliminate some contour distortions while retaining significant topological and geometric properties. In practical terms, thin-line representations of lines and curves are more amenable to the extraction of significant points such as end-points, intersections, critical points and discontinuities in curvature. Lam *et al.* [58] offer a comprehensive reference on techniques relating to thinning methodologies.

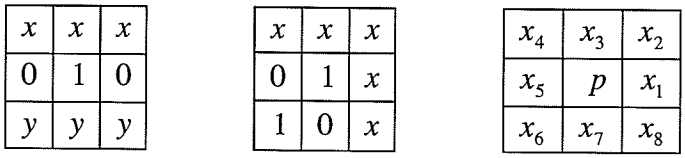

Figure 3-15. Classical Thinning Algorithm Masks

The algorithm functions by deleting successive layers of pixels on the contour until only a skeleton remains. The deletion or retention of a pixel, p, would depend on the

configuration of pixels in the local neighborhood containing p (Figure 3-15(c)). The classical thinning algorithm, mentioned by Pavlidis [78] uses the 3×3 masks shown in Figure 3-15(a) and (b), together with their 90° rotations to determine skeletal pixels. At least one pixel in each group x or y must be non-zero.

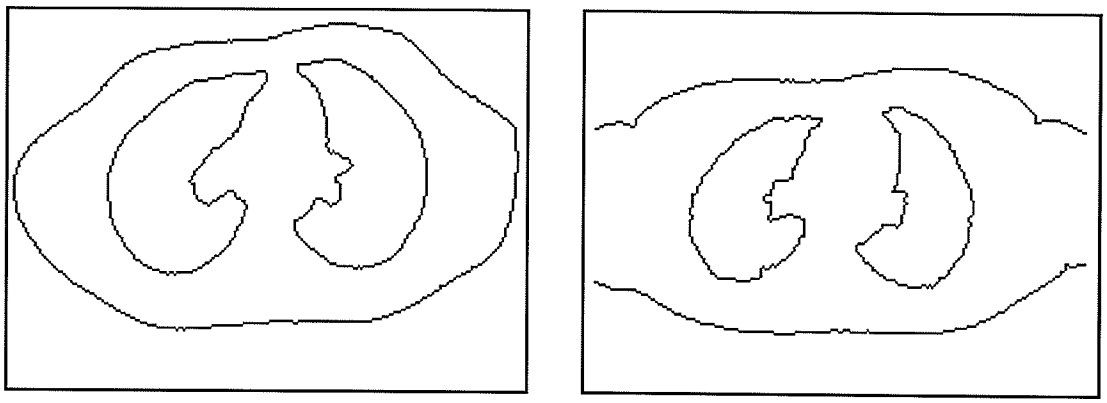

(a) (b)

Figure 3-16. Thinning of Figures 3-14(a) and (b)

Figures 3-16(a) and 3-16(b) show the thresholded images of Figures 3-14(a) and (b) respectively, after skeletonization, clearly depicting the two lungs and the front and back body contours.

3.4.7 Detecting Secondary Features

Secondary features within medical images predominantly take the form of straight lines and curves, derived from edges. Straight lines have a number of significant points associated with them, namely, the end-points, line intersections and corners. Distinct corners within the image can be derived directly from edges. Curves also contain a multitude of significant points which usually take the form of either critical points or discontinuities in curvature. The extraction of secondary features can be approached in a number of ways, as depicted in Figure 3-2. The first technique

involves simply thresholding the edge image and thinning the resulting image. The second technique involves attenuating the edges in the edge image before thresholding. The particular technique chosen is dependent on the content of the image, so no generalized method has been proposed.

3.4.7.1 Line and Curve Detection

There are two ways to extract lines and curves from an image, namely template operators and gradient operators.

Template-Detection

Lines and curves are extended edges. Line detection can be accomplished by threshold detecting a line gradient, using:

$$g(x,y) = \underset{m=1}{\overset{4}{\text{MAX}}}\left\{\left|f(x,y) \times H_m(x,y)\right|\right\} \tag{3.20}$$

where $H_m(x,y)$ is a 3×3 mask corresponding to a specific line orientation, as shown below in Figure 3-17.

H_1

−1	2	−1
−1	2	−1
−1	2	−1

H_2

−1	−1	−1
2	2	2
−1	−1	−1

H_3

−1	−1	2
−1	2	−1
2	−1	−1

H_4

2	−1	−1
−1	2	−1
−1	−1	2

(a)

−1	2	−1
−2	4	−2
−1	2	−1

−1	−2	−1
2	4	2
−1	−2	−1

−2	−1	2
−1	4	−1
2	−1	−2

2	−1	−2
−1	4	−1
−2	−1	2

(b)

Figure 3-17. Line Masks: (a) Unweighted (b) Weighted

Figure 3-17 shows two sets of masks, called weighted and unweighted, which are analogous to the Prewitt and Sobel edge detectors. These patterns are used to detect, not only straight lines, but also arbitrary smooth curves. The patterns can be altered to detect branchings or intersections as well.

Gradient-Detection

The gradient-based detection method proposed by Shu [98] uses the edge image derived in Section 3.4.4. and essentially thins the edges. If *G(x,y)* represents the image after edge detection has been performed, then a thinning edge operation can be performed to yield thinned edges. If $[G(x,y) \geq G(x-1,y)]$ and $[G(x,y) \geq G(x+1,y)]$, then the gradient is given by Equation (3.21), else it is 0. Similarly if $[G(x,y) \geq G(x,y-1)]$ and $[G(x,y) \geq G(x,y+1)]$ then the gradient is given by Equation (3.22), else it is 0. Equation (3.21) reduces edge width in the horizontal direction by increasing the gray value of those edge pixels which have a local maximum gray value and zeroing the gray values of those pixels which do not have a local maximum gray value. Equation (3.22) reduces edge width by the same manner in the vertical direction.

$$G_x(x,y) = G(x-1,y) + G(x,y) + G(x+1,y) \tag{3.21}$$

$$G_y(x,y) = G(x,y-1) + G(x,y) + G(x,y+1) \tag{3.22}$$

Then the image containing the thinned edges (lines and curves) is obtained by substituting Equations (3.21) and (3.22) into Equation (3.23) below.

$$G_{thin} = \left\{ G_x(x,y)^2 + G_y(x,y)^2 \right\}^{\frac{1}{2}} \tag{3.23}$$

Any calculated value which is greater than 255 is truncated to 255.

3.4.7.2 End-Points and Intersections Detection

Once lines and corners have been detected from the primary features of an image, end-points and intersections can be automatically extracted. End-points require no special effort for their detection, they are available directly from the line or curve, assuming the curve is open, as a closed curve has no distinct end-points. An intersection or junction may take one of the forms as shown in Figure 3-18.

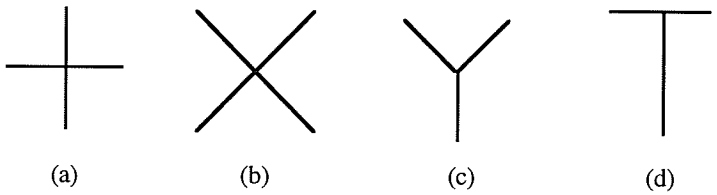

Figure 3-18. Types of Intersection
(a) "+" (b) "×" (c) "Y" (d) "T"

Each of these intersections includes rotational variants. To detect intersections within an image, a template matching technique may be employed using the 3×3 masks shown below in Figure 3-19, each of which corresponds to an intersection in Figure 3-18. These masks are analogous to Sobel edge detectors. To obtain a complete set of intersection detection masks, both Figure 3-19(c) and (d) would have to be rotated through 45° and 90° respectively.

−2	1	−2
1	4	1
−2	1	−2

(a)

1	−2	1
−2	4	−2
1	−2	1

(b)

2	−2	2
−2	4	−2
−2	2	−2

(c)

1	4	1
−2	1	−2
−2	1	−2

(d)

Figure 3-19. Intersection Masks (a) "+" (b) "×" (c) "Y" (d) "T"

Intersection detection is accomplished by threshold detecting an intersection gradient, using Equation (3.20) where $H_m(x,y)$ is a 3×3 mask corresponding to a specific intersection mask as shown in Figure 3-19.

3.4.8 Detecting Corners

A corner is defined as the intersection point or junction point between two or more straight line edges (i.e. edges which have discontinuities along a straight line) [77]. There are two basic approaches to corner-detection: template-based and gradient-based [100]. A review of corner detection techniques can be found in Mehrotra and Nichani [69] and Liu and Srinath [63].

3.4.8.1 Template-Based

Template-based corner detection involves determining the similarity between a given template of size $n \times n$ and all sub-images of size $n \times n$ in a given image. Examples of 3×3 templates representing an "ideal" right-angled corner is shown below in Figure 3-20.

4	4	4
4	−5	−5
4	−5	−5

−4	−4	−4
−4	5	5
−4	5	5

Figure 3-20. Examples of 3x3 Corner Templates

Corner detection can be accomplished by threshold detecting a corner gradient, using Equation (3.20) where $H_m(x,y)$ is a 3×3 mask corresponding to a specific corner orientation, as shown in Figure 3-20. The difficulty with this method is that many different templates must be used, one for each desired orientation and for each possible corner shape. For example, a clockwise shift of the eight boundary elements

of both templates in Figure 3-20 gives a 45° rotation of the corner, resulting in eight separate templates.

3.4.8.2 Gradient-Based

Gradient-based corner-detection is similar to the gradient-based gray-level edge detection discussed earlier in Section 3.4.4. Gradient based methods rely on measuring the curvature of an edge that passes through a neighborhood [100]. In simplified terms, a noticeable change in direction on an edge denotes a corner. It is generally a function of the edge strength and the gradient of the edge direction.

First a gradient-based edge detection technique using Equations (3.5) and (3.6) with an appropriate mask is used to derive the magnitude $G_M(x,y)$ and direction $G_D(x,y)$ of each point in the image respectively. Kitchen and Rosenfeld [55] denote a "cornerity measure" of the form given below in Equation (3.24).

$$G_C(x,y) = G_M(x,y) \times G_{CM}(G_D(x,y)) \tag{3.24}$$

In Equation (3.24) $G_{CM}(G_D(x,y))$ is the gradient magnitude of the gradient direction $G_D(x,y)$ (or change of direction along an edge), which is associated with the point *(x,y)*. It is derived by using a gradient-operator on the "gradient-direction image" obtained from Equation (3.6). If $g_x(x,y)$ and $g_y(x,y)$ represent the partial derivatives of $G_D(x,y)$ the direction image, derived using Equation (3.12), then $G_{CM}(G_D(x,y))$ is derived by substituting g_x and g_y into Equation (3.25).

$$G_{CM}(G_D(x,y)) = \left[g_x(x,y)^2 + g_y(x,y)^2\right]^{\frac{1}{2}} \tag{3.25}$$

3.4.9 Contour Extraction

Each line or curve can be represented by a set of boundary points, more commonly known as a *contour*. A contour is described by n integer points of the form $C = \{p_i = (x_i, y_i), i = 1,...,n\}$, where p_{i+1} is a neighbor of p_i (*modulo n*) for a closed curve, and p_{i+1} is a neighbor of p_i until $i+1=n$ for an open curve. The contour is extracted by tracing the curve in an anti-clockwise direction, using the concept of an N-neighbor. Pavlidis [79] defines the term N-neighbor where 0≤N≤7 is used to denote that pixel whose position is marked with N in Figure 3-21 (Freeman Chain Code).

3	2	1
4	*p*	0
5	6	7

Figure 3-21. Freeman Chain Code

Select an initial point p_i on the contour, such that its 4-neighbor is not part of the contour. Then starting with direction S=6 and current point $c_i = p_i$, check the (S-1), S and (S+1) neighbors of p_i. If the (S-1) neighbor belongs to the contour, set the current point to (S-1) and decrement S by 2. Else if the S neighbor belongs to the contour, set the current point to S, else if the (S+1) neighbor belongs to the contour, set the current point to (S+1). If none of these conditions holds increment S by 2. Continue until the current point is the same as the initial point (closed curve) or the curve ends (open curve). This traversal produces an i-contour, that is a contour composed of indirect neighbors, which includes both vertical, horizontal and diagonal neighbors of p, as in Figure 3-21.

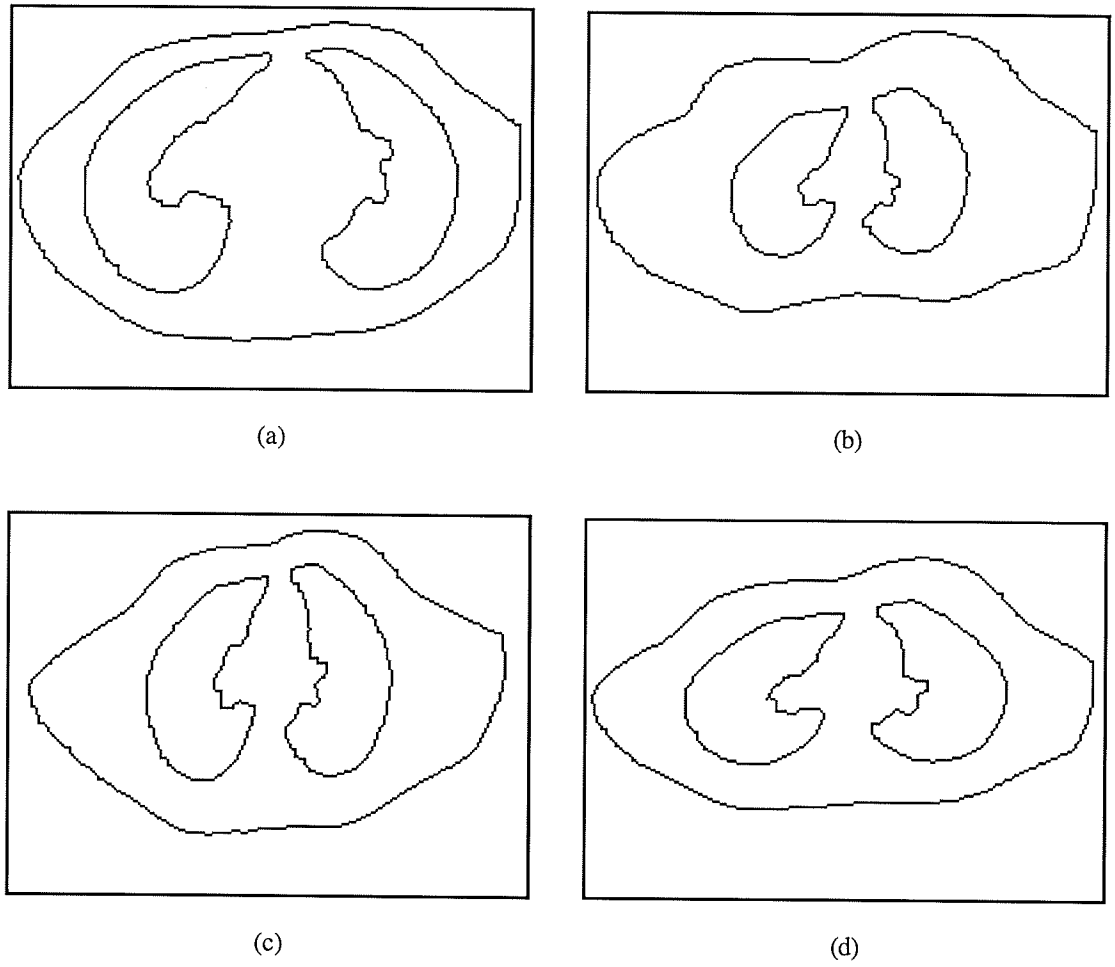

Figure 3-22. Contours of Geometrically Distorted Images
(a) Barrel ,(b) Pincushion, (c) Radial (horizontal), (d) Radial (vertical)

The CT images shown in Figure 3-22 and Figure 3-23 show the contours extracted from the distorted images described in Section 2.6. The largest contours have been extracted from the images, namely the left and right lung boundaries and the front and back body contours.

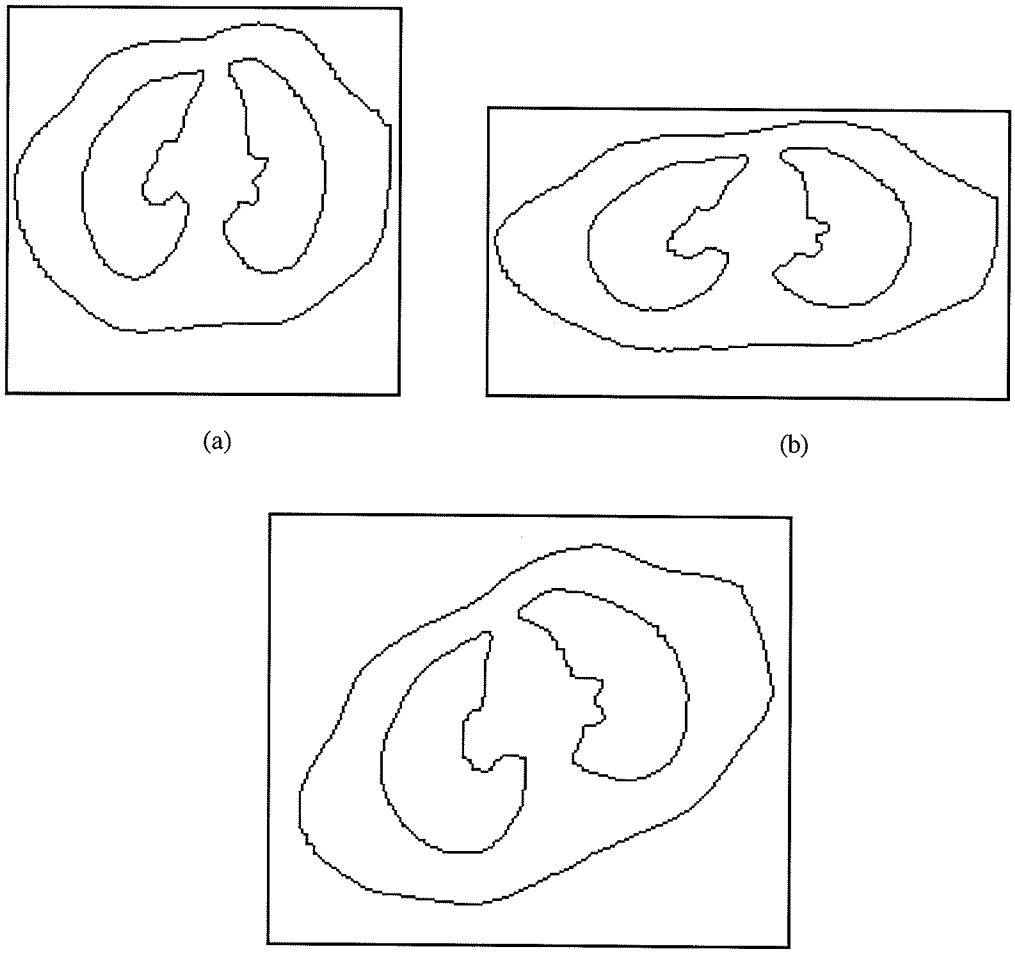

Figure 3-23. Contours of Linearly Distorted Images
(a) Horizontal Scaling , (b) Vertical Scaling, (c) 23° Rotation

3.5 Control-Point Detection

Once secondary features have been extracted from an image (i.e. lines and curves) control-points, can be detected. Many authors have addressed the problem of selecting control points from images. Stockman *et al*. [102] used line intersections as control-points, Goshtasby *et al*. [43] and Ton and Jain [110] used shape points in the form of centers of gravity of closed boundary regions as control points. Kanal *et al.* [54] used high curvature points in an image as control points. Control-point detection

techniques depend on the nature of the feature which has been extracted and therefore no general method for finding control-points has been proposed. For example, a contour which lacks distinct curvature discontinuities might be better suited to a polygonal approximation method, rather than one which detects discontinuities in curvature. Figure 3-24 shows the general schema related to control-point detection.

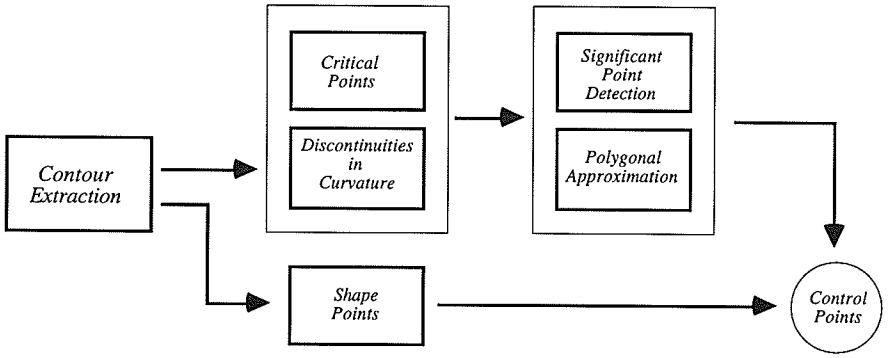

Figure 3-24. Schema for Control Point Detection

3.5.1 Significant Points

The significant points of a curve are classified as its critical points (curvature maxima, minima and points of inflection) and discontinuities in curvature ("corners"), often referred to by the acronym DIC. Additional significant points may include end points, intersections (junctions) and points of tangency. Of all the significant points, DIC's are the most sharply and most reliably defined. The next best significant points to use are points of inflection and points of extreme curvature (maxima or minima).

To a varying degree, these points are all well defined and relatively invariant under rotation and scale. Many methods have been suggested for detecting critical points. They fall into two categories - one is to find the critical points through significant-point detection, and the other is to obtain a piecewise linear polygonal

approximation of the curve [4]. Both methods are discussed here. Most of these methods require a parameter which is used to determine the *region of support* for each point. Too large a region will smooth out fine features and too small a region will generate a large number of unwanted points.

Shape is a property of a curve and refers to the manner in which the curve deviates from some norm, such as a straight line. The kind of curve topologies are shown in Figure 3-25 [47]. A closed curve, (Figure 3-25(a)) is a curve without an end (i.e. $p_1 = p_n$); an open curve, (Figure 3-25(b)) has two distinct end points (i.e. $p_1 \neq p_n$).

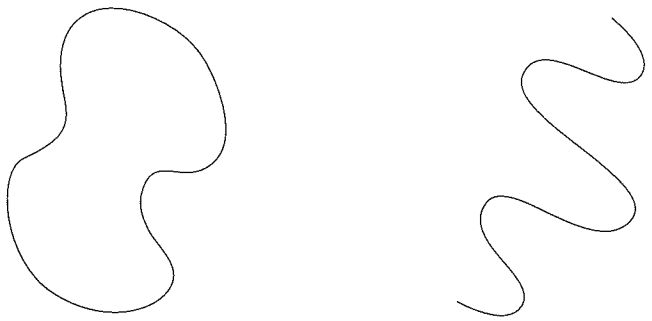

(a) (b)

Figure 3-25. Curve Topologies (a) Closed (b) Open

3.5.1.1 Curvature

Curvature describes how much a curve "bends" at some point. On a Euclidean plane, curvature κ is defined as the rate of change of the angle of the slope of the tangent line as a function of arc length. For a curve defined parametrically in terms of two functions $x(s)$ and $y(s)$, $C = \{x(s), y(s)\}$, where s is the arc length of the curve, the curvature κ of C at a point P is defined as the instantaneous rate of change of the slope angle θ of the tangent line at point P with respect to arc length s, as measured

along the curve. In addition it can be shown that the curvature of C at P is equal to the inverse of the radius ρ of the circle of curvature at point P. The circle of curvature at point P is a circle tangent to the curve at point P whose centre lies on the concave side of the curve and whose curvature is the same as that of the curve at point P. Thus, κ can be expressed as:

$$\kappa = \frac{d\theta}{ds} = \frac{1}{\rho} \tag{3.26}$$

Indeed, if C is given explicitly by a relation of the form $y = f(x)$, then the derivatives $y' = \frac{dy}{dx}$ and $y'' = \frac{d^2y}{dx^2}$ may be used to determine the curvature κ by:

$$\kappa = \frac{y''}{\left[1 + (y')^2\right]^{\frac{3}{2}}} \tag{3.27}$$

However, if C is given parametrically in terms of some parameter t, then y' and y'' can be expressed in terms of the first and second derivatives of $x(t)$ and $y(t)$. In particular, using:

$$x_1 = \frac{dx}{dt}, \quad x_2 = \frac{d^2x}{dt^2}, \quad y_1 = \frac{dy}{dt}, \quad y_2 = \frac{d^2y}{dt^2} \quad \text{and} \quad y' = \frac{y_1}{x_1}, \quad y'' = \frac{y_2}{x_2}$$

it can be shown that

$$\kappa = \frac{x_1 y_2 - y_1 x_2}{\left(x_1^{\,2} + y_1^{\,2}\right)^{\frac{3}{2}}} \tag{3.28}$$

In a digital curve however, it is not clear how to define an equivalent measure of slope as successive points on the curve can only differ in slope by a multiple of 45°, and therefore, small changes in slope cannot be evaluated.

3.5.1.2 Critical Points and Points of Inflection

Points at which the derivative (slope of the tangent line at that point) $\frac{d\kappa}{dt} = 0$ are termed *critical points* [115]. Freeman [29] and Thapa [107] define the critical points of a curve as its curvature extrema (See Figure 3.26). The term extremum (*pl.* extrema) is used to describe a value that is a maximum or a minimum. Curvature *maxima* occur when the curvature at a point p_i is greater (in magnitude) than that of its two immediate neighbors p_{i-1} and p_{i+1} ($\frac{d\kappa}{dt} > 0$ to the left of p_i and $\frac{d\kappa}{dt} < 0$ to the right of p_i). Curvature *minima* occur when the curvature at a point p_i is less (in magnitude) than that of its two immediate neighbors p_{i-1} and p_{i+1} ($\frac{d\kappa}{dt} < 0$ to the left of p_i and $\frac{d\kappa}{dt} > 0$ to the rightof p_i). An *infection point* is a point p_i on a curve where the tangent intersects the curve (i.e. at a point p_i the curvature is negative to one side and positive on the opposite side). It often corresponds to points with zero curvature.

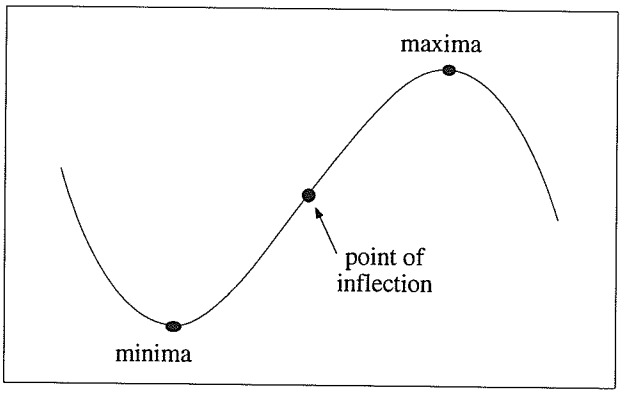

Figure 3-26. Examples of Critical Points and Points of Inflection

3.5.1.3 Discontinuities in Curvature (DIC)

Discontinuities in curvature, identified by the acronym DIC, may take the form of "corners" in a curve. Asada and Brady [6] define a "corner", as a point where the tangent to the curve (and hence the curvature) is discontinuous. An example of a discontinuity in curvature is shown in Figure 3-26.

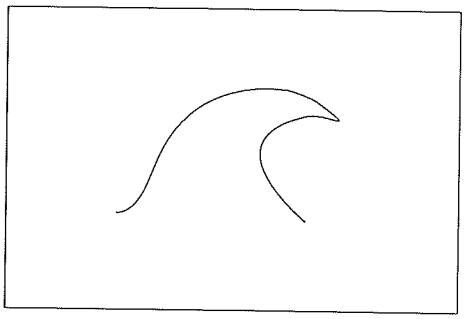

Figure 3-26. Example of a DIC - "Corner"

3.5.2 Polygonal Approximation

Polygonal approximation is the representation of a curve by a polygon. In polygonal approximation, significant points correspond approximately to the actual or extrapolated intersections of any two adjacent line segments. These points are known as the vertices or "break points" of the closed curve. A common property shared by most polygonal approximation methods is the detection of collinearity, which determines if points along the curve are collinear with respect to a straight line segment. Collinearity is determined by the maximum perpendicular distance from a point p_i of the curve to a chosen straight line segment. If this distance is within a given tolerance, that curve portion is approximated by the straight line segment. Otherwise the point becomes a new vertex. Two methods of polygonal approximation are considered here, for an overview of various methods refer to Meek and Walton [68].

3.5.2.1 Bisection

The bisection method is a 'divide and conquer' strategy. Let P_j and P_k represent two points on a curve. Represent all the points from P_j to P_k by a line segment joining P_j to P_k. Determine whether all the points P_i from P_j to P_k, $j \le i \le k$ are within a given tolerance ε (See Figure 3-28) of the line segment which joins P_j to P_k. If all the points are within the tolerance, then P_jP_k is considered a segment. The tolerance, ε, is given by Equation (3.29), with respect to Figure 3-28.

$$\varepsilon = P_iP_k \sin\theta \tag{3.29}$$

$$\theta = \cos^{-1}\left(\frac{P_iP_k^2 + P_jP_k^2 - P_iP_j^2}{2\left(P_iP_k \times P_jP_k\right)}\right) \tag{3.30}$$

If however, one or more of the points exceeds the tolerance, the curve is bisected at m, such that $m = Int\left(\frac{j+k}{2}\right)$ or the index of the point midway between the indices of the end points. Each line segment P_jP_m and P_mP_k is then separately tested.

The initial division is different for open and closed curves. For an open curve, the two end-points can be used. However, for a closed curve, there are no obvious candidates for end-points. Here, two oppositely located extremal points are selected (e.g. highest left-most and lowest right-most).

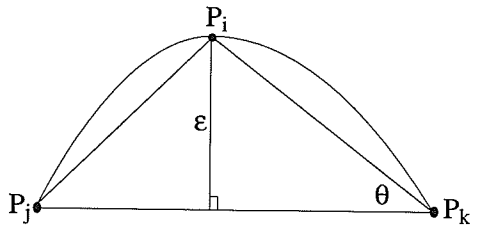

Figure 3-28. Estimation of Tolerance: ε

Figures 3-29 shows the control points extracted from the curves in Figures 3-16 using normal bisection.

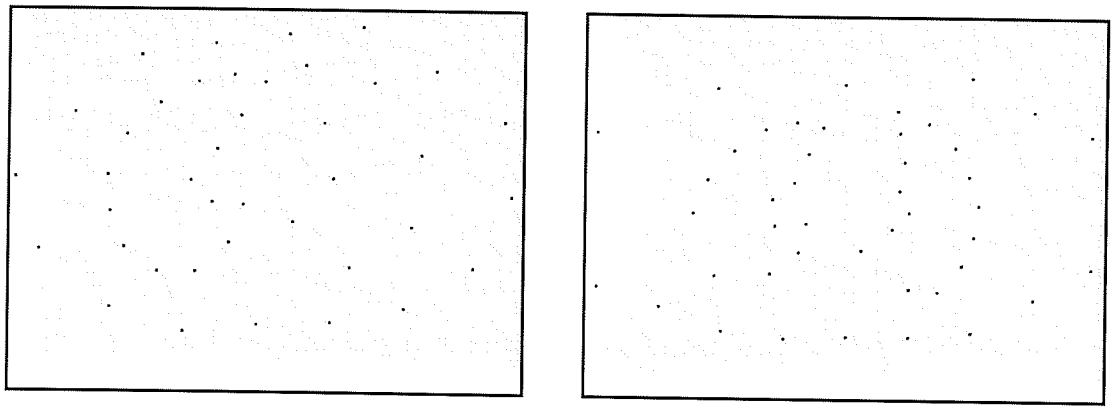

(a) (b)

Figure 3-29. Control Point Sets derived using Normal Bisection
(a) Original CT Image (b) Original MR Image

3.5.2.2 Farthest Point Bisection

An adaptation of the Bisection Method, this method uses the point farthest from the line, instead of the middle point, to bisect the curve. Figures 3-30 shows the control points extracted from the curves in Figures 3-16 using farthest point bisection.

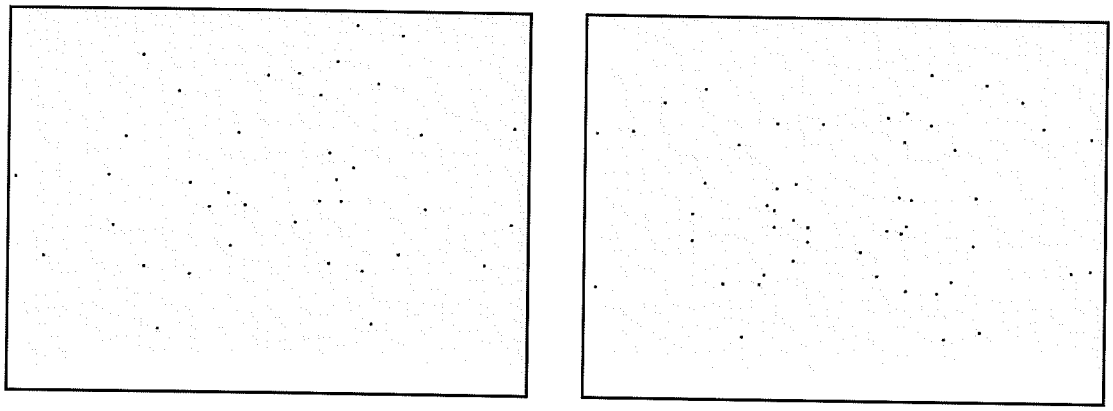

(a) (b)

Figure 3-30. Control Points selected using Farthest Point Bisection
(a) Original CT Image (b) Original MR Image

The farthest-point bisection method is more receptive to curvature extrema and is better suited for extracting control points than is normal bisection.

3.5.3 Significant-Point Detection Methods

The methods discussed here detect critical points by measuring the changes in the angle (curvature) of the contour points. The angle is related to the curvature. The smaller the angle, the larger the curvature. There are two major problems with detecting significant points in digital curves. One is the discrete version of the curvature, the other is the determination of the *region of support* for the computation of the curvature. If the curvature at a point p_i is defined by simply replacing the derivatives in Equation (3.27) by the first differences, the succesive slope angles on the digital curve can differ only by multiples of 45° and therefore small changes in slope cannot be evaluated. The problem is alleviated in various point detection methods by using $k>1$ differences, rather than simply using the first differences ($k=1$). This is essentially a smoothed version of discrete curvature, where k is viewed as a region of support. If too large a region of support is selected, some significant points will be missed, and conversely if it is too small extra insignificant points may be detected.

Three methods to detect significant points are discussed here, the Rosenfeld-Johnston method, the Freeman-Davis method and the Ray-Ray method. All three provide the groundwork for other methods. Teh and Chin [105] offer an overview of various dominant point detection methods, as well as presenting a method motivated by the Rosenfeld-Johnston method, where the region of support, and hence the smoothing factors of each point are determined based on its local properties.

3.5.3.1 Rosenfeld-Johnston Method

Rosenfeld and Johnston [63,94,106] detect significant points as curvature extrema points using a measure of significance known as a k-cosine. The k-vectors a_{ik} and b_{ik} at some point p_i for some smoothing factor, $k>0$ can be defined as:

$$\begin{aligned} a_{ik} &= (x_i - x_{i+k}, y_i - y_{i+k}) \\ b_{ik} &= (x_i - x_{i-k}, y_i - y_{i-k}) \end{aligned} \tag{3.31}$$

The cosine c_{ik} of the angle between the two k-vectors a_{ik} and b_{ik} is defined as:

$$c_{ik} = \frac{(a_{ik} \bullet b_{ik})}{|a_{ik}||b_{ik}|} \tag{3.32}$$

These k-cosines contain the curvature properties such that $-1 \le c_{ik} \le 1$, and $c_{ik} = +1$ for the sharpest angle (0°) and $c_{ik} = -1$ for a straight line (180°). At each point (x_i, y_i) on the curve, calculate c_{ik} for a range of values of k such that $1 \le k \le m$, for some fixed smoothing factor m (either $n/10$ or $n/15$ [94]), based on the level of detail in the curve. A region of support, h, and a k-cosine c_{ih} is assigned to each point such that

$$c_{i,m} < c_{i,m-1} < \ \ldots \ < c_{i,h} \ge c_{i,h-1}$$

The value of h and the corresponding c_{ih} are used to detect dominant points. There is a curvature maximum or minimum at point p_i if $c_{ih} \ge c_{jh}$ for all j such that $|i - j| \le h/2$.

Rosenfeld and Weszka [95] presented an improved version of the Rosenfeld-Johnston method, which involved averaging the k-cosine, c_{ik}, prior to the selection of sizes, h.

$$\begin{aligned} \bar{c}_{ik} &= \frac{2}{k+2}\sum_{j=k/2}^{k} c_{ij} \quad (for\ k\ even) \\ &= \frac{2}{k+3}\sum_{j=(k-1)/2}^{k} c_{ij} \quad (for\ k\ odd) \end{aligned} \tag{3.33}$$

The $\bar{c}_{ik}$'s are then treated just like the c_{ik}'s in the Rosenfeld-Johnston method to find the local maximum and minimum as the points of high curvature.

3.5.3.2 Freeman-Davis Method

Freeman and Davis [30,63] define a discontinuity in curvature as an isolated discontinuity in the mean slope. The method detects local curvature maxima points as significant points. Consider representing a closed curve as a series of n vectors, $c_i = \overline{p_{i-1}p_i}$ each of which can be represented by an integer $f = 0,..,7$ as shown in Figure 3-21. Often called the Freeman Chain [106], this is defined $\{c_i, i = 1,...,n\}$ where the vector $c_i \in \{(1,0),(1,1),(0,1),(-1,1),(-1,0),(-1,-1),(0,-1),(1,-1)\}$.

Define a straight line segment L_{is} that connects the initium of c_{i-s+1} to the terminus of c_i. The length of L_{is} is given by:

$$l_{is} = \left[(X_{is})^2 + (Y_{is})^2\right]^{\frac{1}{2}} \tag{3.34}$$

In Equation (3.34), the x and y components are given by:

$$\begin{aligned} X_{is} &= \sum_{j=i-s+1}^{i} c_{jx} \\ Y_{is} &= \sum_{j=i-s+1}^{i} c_{jy} \end{aligned} \tag{3.35}$$

where the c_{jx} and c_{jy} are the x and y components respectively and $c_{jx}, c_{jy} \in \{-1,0,1\}$. The angle L_{is} makes with the x-axis is given by:

$$\theta_{is} = \tan^{-1}\left(\frac{Y_{is}}{X_{is}}\right) \quad if \ |X_{is}| \geq |Y_{is}|$$
$$\theta_{is} = \cot^{-1}\left(\frac{X_{is}}{Y_{is}}\right) \quad if \ |X_{is}| < |Y_{is}| \tag{3.36}$$

The incremental curvature δ_{is} is defined as twice the mean over two adjacent angular differences:

$$\begin{aligned}\delta_{is} &= 2\left[\frac{\left(\theta_{i+1,s} - \theta_{i,s}\right) + \left(\theta_{i,s} - \theta_{i-1,s}\right)}{2}\right] \\ &= \theta_{i+1,s} - \theta_{i-1,s}\end{aligned} \tag{3.37}$$

The incremental curvature is a smoothed measure of curvature, the greater the value of s, the region of support, the greater the smoothing. Normally, s, ranges from a minimum of 5 to a maximum of 13 [105]. For a fairly straight section of curve, δ_{is} will hover about zero. For a gentle curve to the left or right, δ_{is} will maintain a small positive or negative value, respectively. At a point of inflection, δ_{is} will change sign. At a significant curvature discontinuity, δ_{is} will take a succession of relatively large values, all of the same sign. Note that the actual position of the discontinuity is s/2 positions earlier, since δ_{is} is labeled according to its leading node. Freeman and Davis define the measure of significance as the "cornerity" or discontinuity in curvature κ_i at point i as:

$$\kappa_i = \ln(t_1) \times \sum_{j=i}^{i+s} \delta_{js}^2 \times \ln(t_2) \tag{3.38}$$

where

$$t_1 = \max\left\{t : \delta_{i-v} \in (-\Delta, \Delta), \ \forall \ 1 \leq v \leq t\right\}$$
$$t_2 = \max\left\{t : \delta_{i+s+v} \in (-\Delta, \Delta), \ \forall \ 1 \leq v \leq t\right\}$$

and

$$\Delta = \tan^{-1}\left(\frac{1}{(s-1)}\right)$$

The $\ln(t_1)$ and $\ln(t_2)$ terms in Equation (3.38) are the lengths of the δ_{is} sequences to either side of the discontinuity and the $\sum_{j=i}^{i+s}\delta_{js}^2$ term is a measure of the slope discontinuity. Retain those points p_i where $|K_i| \geq |K_j|$ for all j such that $|i-j| \leq s$.

If a point of inflection is prominent, that is, if there is a clear and abrupt shift of the radius of curvature, the Freeman-Davis Method will locate it. If however, the curve changes from convex to concave curvature in a slow and meandering fashion, the point of inflection cannot be determined in this way. An alternative is to connect two points of opposing maximum curvature with a straight line and take its intersection with the chain as the point of inflection.

Beus and Tiu [11] provide two modifications to the Freeman-Davis method. First, κ_i is determined as the average of the k-values obtained at a particular point by letting s vary between two values $s1$ and $s2$.

$$\kappa_i = \left(\sum_{s=s1}^{s2}\left[\ln(t_1)\times\sum_{j=i}^{i+s}\delta_{js}^2\times\ln(t_2)\right]\right)\Big/(s2-s1) \tag{3.39}$$

where

$$t_1 = \max\left\{t: \delta_{i-v} \in (-\Delta,\Delta),\ \forall\ 1 \leq v \leq t\ \ and\ \ t \leq N\right\}$$
$$t_2 = \max\left\{t: \delta_{i+s+v} \in (-\Delta,\Delta),\ \forall\ 1 \leq v \leq t\ \ and\ \ t \leq N\right\}$$

Secondly, a new variable N is introduced which determines the maximum cutoff value of t_1 and t_2. $N = C \times F$ where C is the chain length and F is a fraction such that $(0 < F \leq 1)$.

3.5.3.3 Ray-Ray Method

Ray and Ray [86,87], propose a technique to detect significant points using a measure of significance known as a k-l-cosine. The k-l-cosine is defined as the cosine of the angle between the k-vectors and l-vectors, denoting the right and left vectors at some point p_i respectively. The size of the right vector is denoted by k and that of the left vector by l. Define two vectors, R_i and R_{ij} at a point p_i by:

$$R_i = (x_{i+1} - x_i, y_{i+1} - y_i) \tag{3.40a}$$

$$R_{ij} = (x_j - x_i, y_j - y_i) \tag{3.40b}$$

In Equation (3.40b) $j = i+2, i+3, i+4, \ldots$ If θ_j denotes the angle between R_i and R_{ij}, then θ_j can be calculated using:

$$\theta_j = \cos^{-1}\left(\frac{R_i \bullet R_{ij}}{|R_i||R_{ij}|}\right) \tag{3.41}$$

θ_j is calculated increasing j until for some j, $\theta_{j-1} < \theta_j \leq \theta_{j+1}$. Then $k = j - i - 1$ is the right region of support. Similarly, define two vectors, L_i and L_{ij} at a point p_i by:

$$L_i = (x_{i-1} - x_i, y_{i-1} - y_i) \tag{3.42a}$$

$$L_{ij} = (x_j - x_i, y_j - y_i) \tag{3.42b}$$

In Equation (3.42b) $j = i-2, i-3, i-4, \ldots$ If ϕ_j denotes the angle between R_i and R_{ij}, then ϕ_j can be calculated using:

$$\phi_j = \cos^{-1}\left(\frac{L_i \bullet L_{ij}}{|L_i||L_{ij}|}\right) \tag{3.43}$$

ϕ_j is calculated decreasing j until for some j, $\phi_{j+1} < \phi_j \leq \phi_{j-1}$. Then $l = i - j - 1$ is the left region of support. Once the left and right regions of support are determined, define the left and right vectors at p_i. The right and left vectors at p_i are denoted by a_{ik} and b_{il} respectively:

$$\begin{aligned} a_{ik} &= (x_{i+k} - x_i, y_{i+k} - y_i) \\ b_{il} &= (x_{i-l} - x_i, y_{i-l} - y_i) \end{aligned} \tag{3.44}$$

The cosine c_{ikl} of the angle between the two k-vectors a_{ik} and b_{il} is defined as:

$$c_{ikl} = \frac{(a_{ik} \bullet b_{il})}{|a_{ik}||b_{il}|} \tag{3.45}$$

Once the k-l-cosine of each point is determined, a two-stage method is applied to detect significant points. At the first stage, all points whose k-l-cosine $\leq$ -0.8 are discarded. Secondly, if c_{ikl} lies between $c_{i-1,kl}$ and $c_{i+1,kl}$, then discard p_i, else p_i is a dominant point.

The major difference between the Ray-Ray method and both the methods of Rosenfeld-Johnston and Freeman-Davis is that the region of support and cosine in the latter two are symmetric with respect to a point p_i, i.e., the region of support consists of the same number of points on either side of p_i. The Ray-Ray method uses an asymmetric region of support and a asymmetric cosine.

3.5.4 Shape Points

Some contours are not closed or do not necessarily start at the same location, for example, some contours start at the edge of the image rather than at a specific feature. A shape point is a description of the shape of a feature. Many different shape points [70] can be used to describe various characteristics of a contour. Mitchie and

Aggarwal [71] used the centroid (unweighted mean point) and weighted mean radius as shape points. Both the centroid and radius weighted mean point are in general found very close to one another.

3.5.4.1 Centroid

Bartoo and Hanson [9] register MR, CT and SPECT images of the brain using the centroids of anatomical features such as the head (including skull), the brain, the ventricles (which hold cerebral spinal fluid), eyeballs and sinuses. If the gray level at each point (x,y) in an image is regarded as its "mass", then the centroid (or "centre of gravity") can be defined as:

$$\begin{aligned} X &= \frac{1}{n}\sum_{i=1}^{n} x_i \\ Y &= \frac{1}{n}\sum_{i=1}^{n} y_i \end{aligned} \tag{3.46}$$

In Equation (3.46), n is the number of points on the contour of the selected feature.

3.5.4.2 Radius Weighted Mean Point

The radius weighted mean point is essentially a weighted form of the centroid and can be defined by the point (X,Y) where the X and Y components are defined as:

$$\begin{aligned} X &= \frac{1}{R}\sum_{i=1}^{n} r_i x_i \\ Y &= \frac{1}{R}\sum_{i=1}^{n} r_i y_i \end{aligned} \tag{3.47}$$

where r_i is the distance from the centroid, derived from Equation (3.46), to the point (x_i,y_i) on the shape and $R = \sum_{i=1}^{n} r_i$.

3.6 Discussion

The methods described above were applied to each of the images in Figures 2-3, 2-6 and 2-7. The general technique used is illustrated in Figure 3-31. Firstly, Sobel edge detection was applied to the image in question to attenuate significant anatomical features, in this case body and lung contours. This was followed by bilevel thresholding, and thinning to produce an image containing the required contours. Once the contours were extracted, control points were detected using the Farthest-Point Bisection polygonal approximation method. The polygonal approximation method was chosen for detecting significant points from the contours due to the unpredictable nature of the angle detection methods.

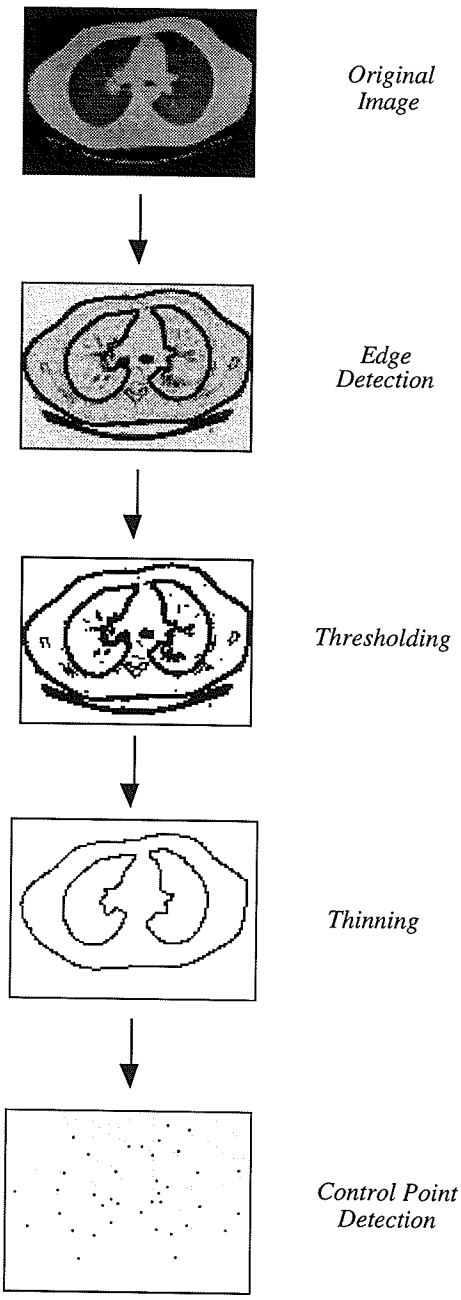

Figure 3-31. Example of Control-Point Selection

Chapter 4

Control Point Matching

4.1 Introduction

The second step in the point-matching registration methodology outlined in Section 2.5 is the establishment of a correspondence between the control points from both images. The problem of control-point matching can be stated as follows. Given a set of "reference" points in one image and "match" points in another image, find the control-point pairs [82]. This chapter is divided into five sections and deals with the theoretrical aspects of control-point matching. Section 4.2 deals with a preliminary discussion on the topic of control-point matching, including the methodology associated with it. Section 4.3 discusses various methods of control-point matching, whilst Section 4.4 focuses on Goshtasby and Stockman's algorithm [42] for control-point matching via *Convex Hulls.* Finally, Section 4.5 focuses on improvements which could be made to the Convex Hull Matching method.

4.2 Preliminaries

As a preliminary note, a brief explanation of terminology follows. *Corresponding points* refers to control points in the two images that match. *Matching* refers to the process that determines corresponding points. *Match* and *mismatch*, respectively, refer to two points that are correctly selected as corresponding points and two points that are mistakenly selected as corresponding points [44]Registration requires that both images coincide at the control points. Therefore the problem of control-point matching can be stated as follows. The first image contains a set of m points. The second image contains a set of points similar to the first set, except that some of the points from the first set are missing and some new points, not in the first set, are present. The second set contains n points: typically, m and n have values in the range 10-50. The positions of the common points in the second set are, within a given tolerance, the same as common points in the first set. The problem then has three parts:

1. Find all points in the first image which do not have a match in the second image.

2. Find all points in the second image which do not have a match in the first image.

3. For all points in the first image which have a common point in the second image find the correct match: these correctly matched control-points are the corresponding points.

Though the problem is to match different images of the "same" scene, the control-points selected from one image will not in general be just a translation, rotation and

scaling of those from the other. The underlying assumption of any control point matching algorithm is that there exists a mapping function between the two sets of points, characterized by some invariant property. If this property does not exist, then a point in the first set could be matched with any point in the second set with an equal chance of it being the "correct" match. Unlike control-point selection techniques, control-point matching techniques do not depend on the image content, rather on the type of distortion contained within the image.

4.3 Methods of Control Point Matching

Various algorithms have been proposed for point matching. Ranade and Rosenfeld [85] proposed a relaxation method for matching two sets having translational differences, based on the support received by a match from other pairs. This method deals primarily with sets of points that contain translational differences only. Given two sets of control points, $P=(P_1,P_2,...,P_m)$ and $Q=(Q_1,Q_2,...,Q_n)$, for each displacement, δ, of P relative to Q, the number of pairs (P_i,Q_j) that lie closer together than some threshold value are counted. If P and Q have many points in common, this will yield a large match value for δ, while other δ's will yield low match values where a few pairs happen to coincide. Wang *et al.* [117] modified the relaxation algorithm in reference [85] to include rotational differences in addition to translational differences.

Stockman *et al.* [102] developed a method of control-point matching based on *clustering*. For each possible pair of matching points, the translational, rotational and scaling differences are determined which represent a point in the cluster space. By finding the best cluster of these points, using statistical methods, the corresponding points can be found. A major problem associated with all these methods is that the

form of distortion is limited to linear distortion, because in general, the methods only allow translational, rotational and scaling differences.

4.4 Convex Hull Matching

Goshtasby and Stockman [42] proposed a method of control-point matching using convex hull edges. This method is based on a patterned search of subsets determining the transformation parameters that can match the largest number of points in the two sets. Subsets are chosen selectively in order to maximize the number of common points in the two subsets. In this approach, points falling on the boundary of the convex hull in each set are chosen as a subset for matching. Once each set has been reduced to a subset, matching is carried out between the two subsets for estimation of transformation parameters .

4.4.1 Methodology

The general methodology associated with the method is as follows:

1. For each two sets of points, S_1 and S_2, determine the convex hull and choose the points on the boundary of the convex hull, denoted C_1 and C_2 respectively, as the representative subsets.

2. Determine the transformation parameters T_α needed for matching a pair of points in C_1 to a pair of points in C_2.

3. For each matching transformation determine the number of points in S_1 that match with points in S_2 within a given threshold value D.

4. Let T_m be the transformation parameters that match the most points in S_1 and S_2, then take T_m as an estimate for the transformation parameters.

5. Using T_m map one set into another and determine the corresponding points in the two sets that match by the threshold value D.

4.4.2 Properties of a Convex Hull

A *convex hull* is a mathematical name for the natural boundary of a point set [97]. The natural boundary of a point set depends on a geometric property called *convexity*. A convex polygon has the simple property that any line connecting any two points within the polygon must itself lie entirely inside the polygon. The convex hull of a set of points is defined to be the smallest convex polygon containing them all. Given n points, some of them will form a convex polygon within which all the others are contained.

The convex hull is invariant under changes in rotation, translation and scaling [42]. Depending on the set of points, at least three points (two in the degenerate case), and at most all the points in the point set will occur on the boundary of the convex hull (BCH). The images in Figures 4-1(b) and (d) show two examples of convex hulls, constructed from the control-point sets in Figures 4-1(a) and (c) respectively.

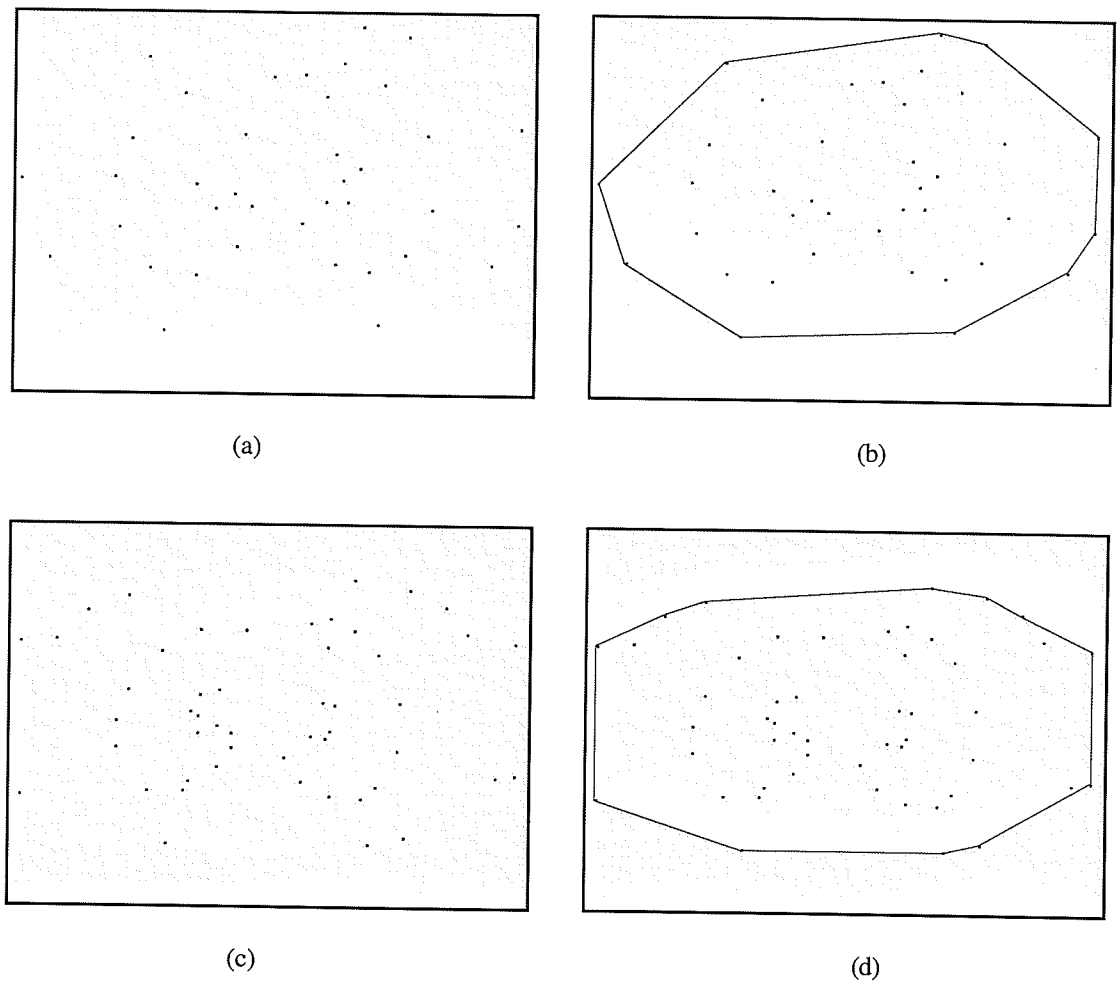

Figure 4-1. Examples of a Convex Hulls
(a,c) Control-Point Sets, (b,d) Convex Hulls

Determination of the convex hull of a set of points will not be discussed here. Efficient methods already exist [97] that can determine the convex hull of a set of points in a plane.

4.4.3 Matching Transformations

First of all it is assumed that *T*, the transformation which maps two sets of points in a plane with translational, rotational and scaling differences is an RST (Rotation, Scaling, Translation) transformation of the form given in Section 5.4.2. The

assumption made in the majority of point matching methods [42,102] is that scaling is uniform, yet many distorted images contain non-uniform scaling. Therefore it should be noted that the methods cited here could use other transformations in place of the general RST transformation given in Section 5.4.2 The matching transformation could also be extended to include other transformations such as a general low-degree polynomial warping.

4.4.4 Threshold Selection

The threshold distance D can be thought of as a circle constructed around each point in the set S_2. If a transformed point from S_1 is contained within the area of the circle then it is considered a match. The Euclidean distance between the two points is given by:

$$E = \left\{ \left[u_i - x_i' \right]^2 + \left[v_i - y_i' \right]^2 \right\}^{\frac{1}{2}} \tag{4.1}$$

where (x_i', y_i') is the transformed point associated with the point (x_i, y_i) in set S_1 and (u_i, v_i) is the corresponding point in set S_2.

4.4.5 Matching Methods

4.4.5.1 Complete Convex Hull Point Matching

This method determines the transformation between two sets of points S_1 and S_2 by matching all the edges in the complete graphs from the convex hulls, C_1 and C_2, of the two sets. The first step is to determine the complete graphs of C_1 and C_2. If there are m points in C_1 and n points in C_2, then there exist $t_1 = m(m-1)/2$ edges in C_1 and $t_2 = n(n-1)/2$ edges in C_2 (See Figure 4-2(a)). Since there are two ways to

match a pair of edges directionally, for every edge in C_2, the edge is reversed and matched with the edges in C_1 again, giving $t_2 = n(n-1)$ directed edges in C_2.

Let E_i $(1 \le i \le t_1)$ and E_j $(1 \le j \le t_2)$ represent an edge in C_1 and C_2 respectively. Match edge E_i to each edge E_j in C_2 to determine T_{ij}, where T_{ij} represents the transformation associated with transforming the edge E_i to the edge E_j. Knowing the parameters of T_{ij} determine the number, N_{ij} of other points in S_1 and S_2 that match within a small threshold distance D by successively transforming points of S_1 and checking a corresponding point in S_2. Finally, let N_{IJ} equal the maximum value of N_{ij}, that is the maximum number of point matches. Knowing the transformation parameters between the two sets, one set can be mapped into another and points can be found from S_1 that fall within a threshold distance of points in S_2. If more than one point from S_1 falls within the threshold value of a point in S_2, the closest point is taken as the corresponding one.

4.4.5.2 Convex Hull Edge Point Matching

The second approach is to determine the transformation parameters between the two sets S_1 and S_2 by matching edges of the BCHs C_1 and C_2 of the two sets. The first step is to determine the edges falling on the BCHs of C_1 and C_2. If there are m points in C_1 and n points in C_2, then there exist $t_1 = m$ non-directional edges in C_1 and $t_2 = 2(n)$ directional edges in C_2 (See Figure 4-2(b)).

Let E_i $(1 \le i \le t_1)$ and E_j $(1 \le j \le t_2)$ represent an edge in C_1 and C_2 respectively. Match edge E_i to each edge E_j in C_2 and determine T_{ij}. Knowing the parameters of T_{ij} determine the number, N_{ij} of other points in S_1 and S_2 that match within a small threshold distance D by successively transforming points of S_1 and checking a corresponding point in S_2. Finally, let N_{IJ} equal the maximum value of

N_{ij} , that is the maximum number of point matches. Knowing the transformation parameters between the two sets, one set can be mapped into another and points can be found from S_1 that fall within a threshold distance of points in S_2 . If more than one point from S_1 falls within the threshold value of a point in S_2 , the closest point is taken as the corresponding one.

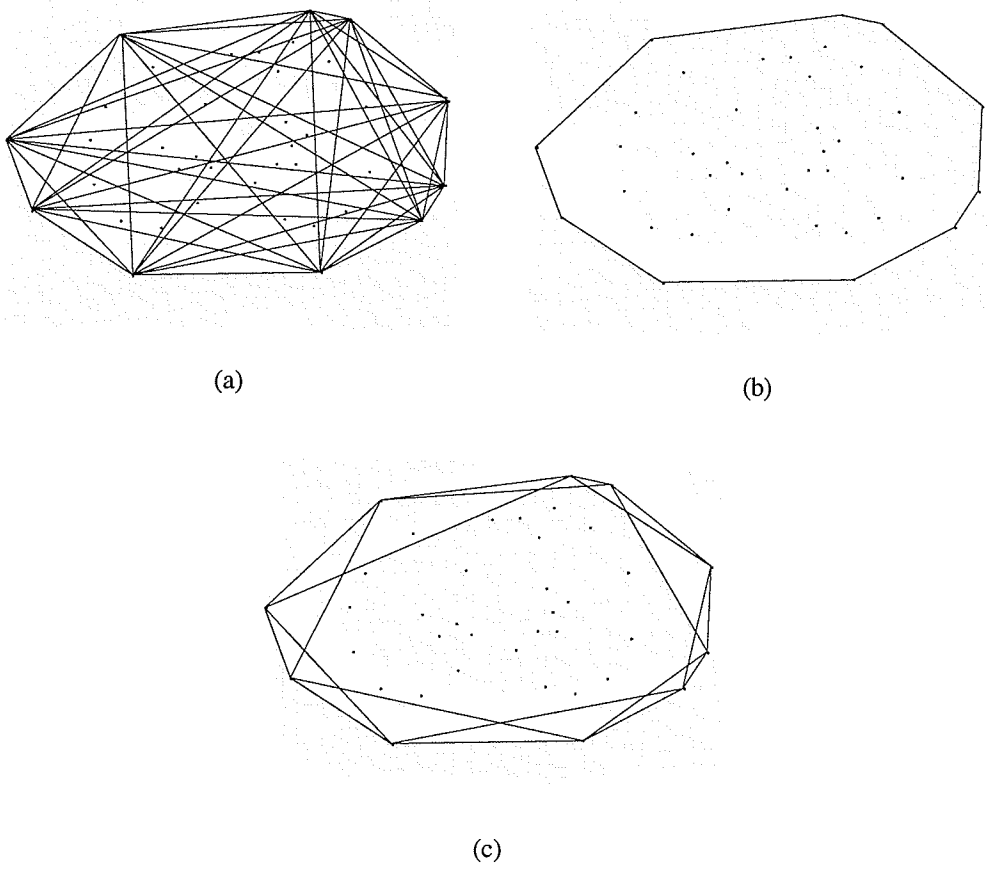

Figure 4-2. Different Convex Hull Configurations
(a) Complete Convex Hull Graph, (b) BCH, (c) Convex Hull Triangulation

4.4.5.3 Convex Hull Triangulation Point Matching

The third method determines the transformation between two sets of points S_1 and S_2 by matching triangles derived from three consecutive points on the convex hull of C_1 and C_2 . For example, at a point p_i on the convex hull of C_1 , a triangulation can be performed such that p_{i-1}, p_i, p_{i+1} form a triangle Δ_i. If there are m points in C_1 and n points in C_2, then there exist m triangles in C_1 and n triangles in C_2 (See Figure 4-2(c)).

Let Δ_i $(1 \le i \le m)$ and Δ_j $(1 \le j \le n)$ represent a triangle in C_1 and C_2 respectively. Match the triangle Δ_i from C_1 to a triangle Δ_j in C_2 and determine T_{ij}. Knowing the parameters of T_{ij} determine the number, N_{ij} of other points in S_1 and S_2 that match within a small threshold distance D by successively transforming points of S_1 and checking a corresponding point in S_2. Finally, let N_{IJ} equal the maximum value of N_{ij} , that is the maximum number of point matches.

Compared to the first method that matched all convex hull complete graph edge combinations, the second method matches only the convex hull edge combinations, whilst the third method is a combination of the first two methods. The differences are seen in Figure 4-2. There are cases, where the second method may fail to estimate the correct transformation parameters, but the first algorithm will succeed (such as when two convex hulls have some common points, but no common edges). Figure 4-3 shows the convex hulls of the control-point sets derived from the images in Figure 2-3.

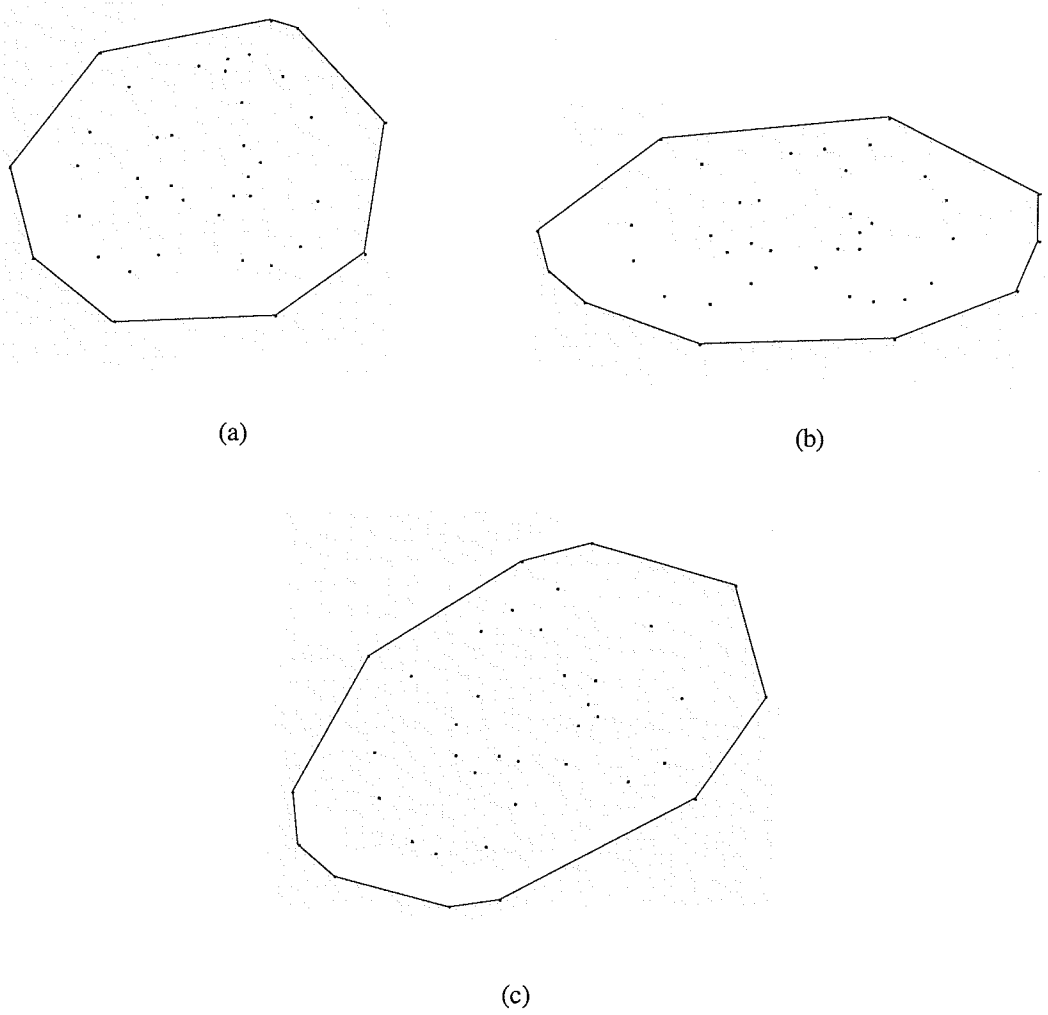

Figure 4-3. Examples of Convex Hulls from Control-Point Sets

4.5 Discussion

Control-point matching methods are based on some form of exhaustive search, that is checking every possible combination of points within two images. Most methods for point-matching become very slow as the number of points in the set increases. The convex hull method overcomes this by using subsets of points for matching. Three methods of convex hull matching have been proposed and there are undoubtedly numerous other variations which could be contrived. For the majority of medical

images which contain linear distortions, or small geometric distortions, these methods would seem adequate.

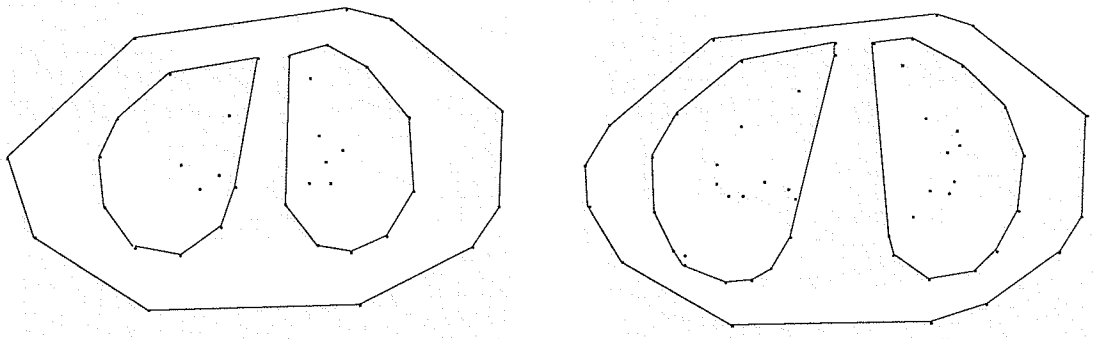

(a) (b)

Figure 4-4. Local Convex Hull Matching
(a) Reference Image, (b) Geometrically Distorted Image

For medical images containing forms of geometric distortion, the methods described may match global areas, such as the body contours, where the convex hulls are similar, but may fail to match points in areas where the geometric distortion is more apparent, such as the lungs (See Figure 4-4). In medical images where the features of interest take the form of the contours of major anatomical features such as the body and lung contours shown in the sample images, a modification of the convex hull method to allow for matching each contour separately might result in a better point-match (Figure 4-4). This would imply a form of *local convex hull matching*. Therefore, with respect to the two images shown in Figure 4-4, each of the convex hulls representing the body and left and right lung contours would be matched separately.

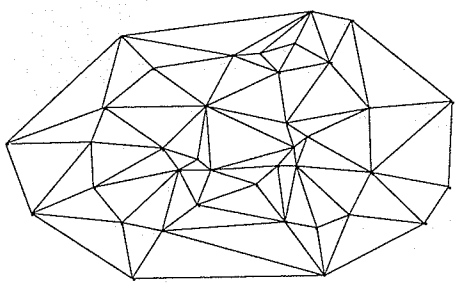

Figure 4-5. Delaunay Triangulation of a Point Set

Another alternative would be to triangulate all the points within a given point set using Delaunay Triangulation [97], whereby a line is drawn between each point and all the points "closest to" it. (See Figure 4-5). The same concept of matching triangles from one set to the other could then be employed.

Chapter 5

Geometric Transformations

5.1 Introduction

The most fundamental characteristic of any image registration technique is the kind of transformation or mapping function needed to align two images [13]. Once control-point pairs have been obtained from the control-point matching algorithm, a mapping function is generated to transform one image into another image, or register the two images.

This chapter is divided into eight sections. Some distorted medical images and their properties are outlined in Section 5.2. Section 5.3 deals with a general overview of transformation methods. Sections 5.4 and 5.5 describe affine and polynomial mapping functions, dealt with using the classical problem of least squares fitting. In Section 5.6, image transformation as a surface fitting problem is formulated, and surface-spline mapping functions are derived. Section 5.7 deals with the registration error associated with the accuracy of the transformation methods and finally Section 5.8 shows the results of transforming the distorted images in Section 5.2.

5.2 Transformation of Medical Images

Medical images can be divided into two categories. The first category includes "flat" two-dimensional images such as computed tomography (CT) and magnetic resonance (MR) images which represent body regions as a stack of transaxial "slices" [13,113]. The second category represents three-dimensional images taken either directly from 3-D modalities such as positron emission tomography (PET) [67], or reconstructed from tomographic images such as CT or MR [16].

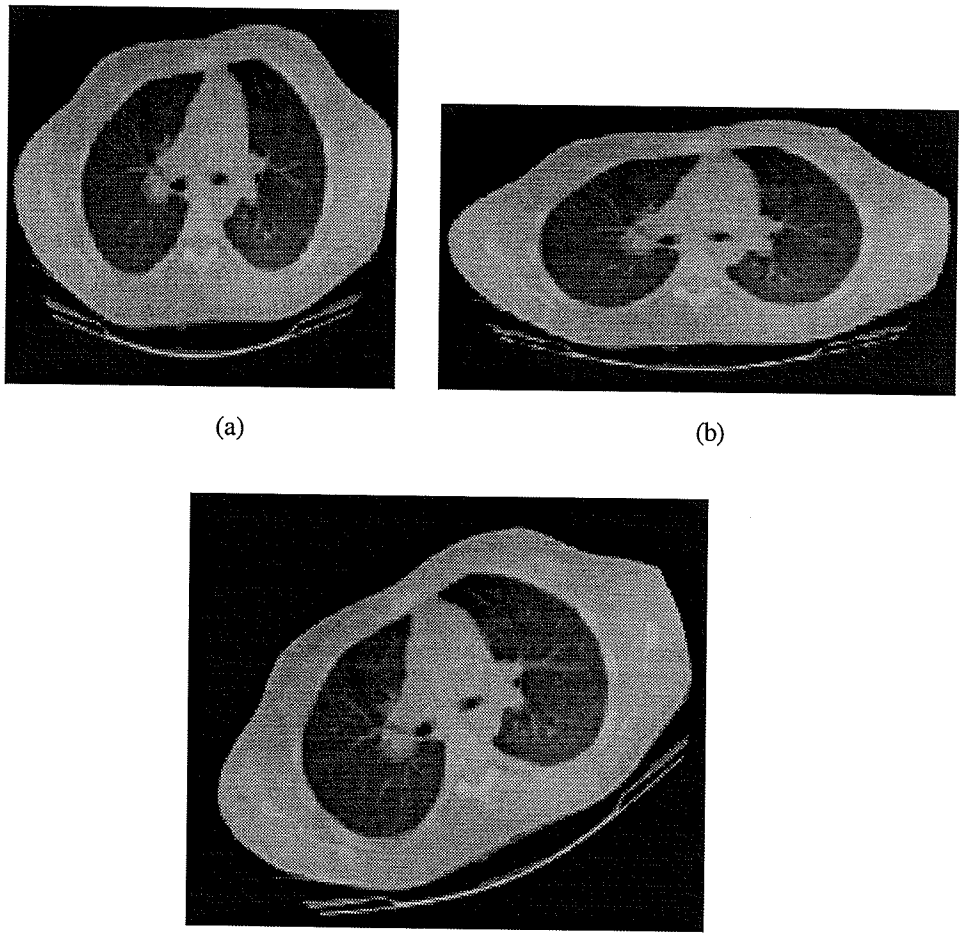

(a) (b)

(c)

Figure 5-1. CT Images of the Thorax (Figure 1-8(a)) containing Linear Distortion
(a) 75% Horizontal Scaling, (b) 75% Vertical Scaling, (c) 23° Rotation

The medical images dealt with here are in the two-dimensional realm. Figure 5-2 shows three images which contain linear distortion. These images are referred to as *distorted images* and will be used in Section 5.9 to illustrate affine and low-degree polynomial transformations.

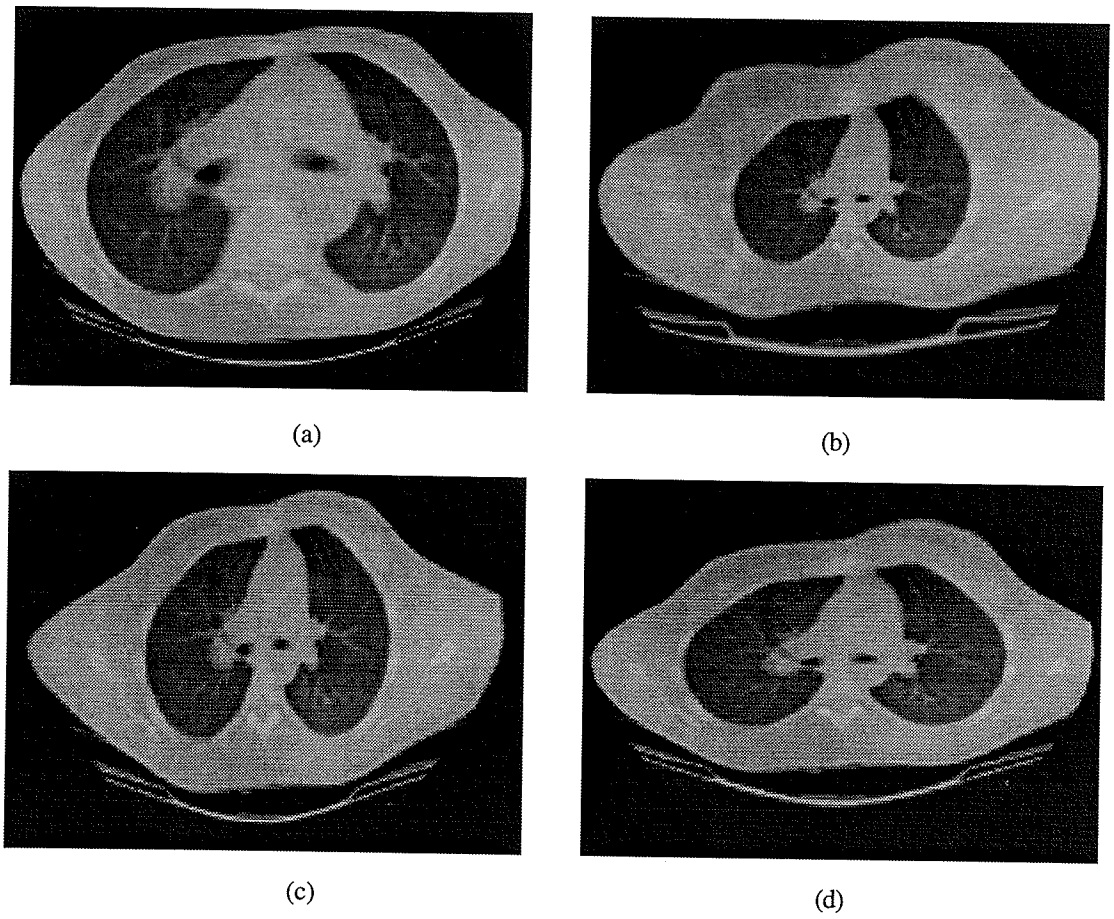

Figure 5-2. CT Images of the Thorax containing Geometric Distortion
Photometric: (a) Barrel, (b) Pincushion; Radial: (c) Horizontal (d) Vertical

Figure 5-2 shows four images which contain differing types of geometric distortion. These images will be used in Section 5.9 to illustrate high-degree polynomial and surface-spline transformations. Figures 5-2(a) and (b) contain photometric distortion, whilst Figures 5-2(c) and (d) containing differing types of radial distortion. When

registering two multimodel images, provision must be made for matching any combination of CT, MR and PET images. For instance when a PET image containing physiological information is combined with a CT image containing anatomic features [67,109], a transformation method must be chosen which will deal with the local distortions contained within the PET image. Conversely, when dealing with matching two CT images, an affine transformation can be used as the distortion contained within the image is usually in the form of misalignment or linear distortion.

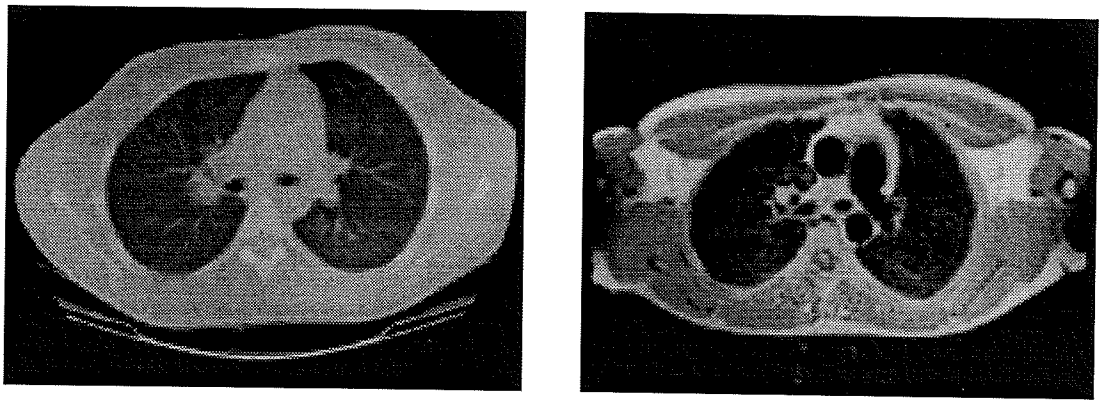

Figure 5-3. Multimodal Images of the Thorax
(a) Computed Tomography, (b) Magnetic Resonance

Figure 5-3(a) shows a CT image of the thorax, which will be used as the *reference image*. Figure 5-3(b) shows the corresponding MR image of the thorax, which will be used to illustrate multimodal registration.

5.3 Methods of Transformation

If P_i denotes a point on a plane, consider a transformation of the plane that causes this point to be displaced to P_i'. Point P_i is said to be *transformed to* or *mapped onto* P_i'. A *geometric transformation* maps the set of n control points (x_i, y_i), $i = 1,...,n$ from the *distorted image* to the corresponding set of control points (u_i, v_i), $i = 1,...,n$

in the *reference image* [70]. A transformation is usually composed of two mapping functions $u = f(x,y)$ and $v = g(x,y)$, that are used to map the distorted image into the reference image. The functions f and g represent the geometric difference between the images. Knowing the position of corresponding control points in the images, the mapping function parameters can be determined by solving the following set of equations.

$$\begin{aligned} u_i &= f(x_i, y_i) \rightarrow x_i' \\ v_i &= g(x_i, y_i) \rightarrow y_i' \qquad i = 1,\ldots,n \end{aligned} \tag{5.1}$$

In Equation (5.1), x_i' and y_i' represent the x and y coordinates in the transformed image respectively. Many differing methods have been proposed to geometrically transform an image. Goshtasby *et al.* [43] and Merickel [70] use the affine transformation as a mapping function, Goshtasby *et al.* [43] and Goshtasby [37] use low-degree polynomials as mapping functions. Goshtasby [39,40] uses piecewise linear and piecewise cubic mapping functions and Flusser [27] and Goshtasby [38] use surface spline mapping functions. Transformation methods are classified as approximation/interpolation and local/global [13][37]. The transformation that maps one image onto the other can be either local or global.

5.3.1 Interpolation

Given the position of a control point (x,y) in the distorted image, an *interpolation* method determines the transformation functions f and g which provide the exact position of the same point in the reference image.

$$\begin{aligned} u &= f(x,y) \\ v &= g(x,y) \end{aligned} \tag{5.2}$$

In interpolating methods, it is assumed that the control points used for matching are located precisely. Any error made in locating a control point will deteriorate the resulting transformation proportionally over the image. Interpolating methods need more transformation parameters as the number of control points in the image increases.

5.3.2 Approximation

Given the position of a control point (x,y) in the distorted image, an *approximation* method determines the transformation functions f and g which approximate the position of the same point in the reference image.

$$\begin{aligned} u &\approx f(x,y) \\ v &\approx g(x,y) \end{aligned} \tag{5.3}$$

In approximating methods, it is assumed that the errors in the location parameters of the control points have zero mean.

5.3.3 Global Methods

A matching transformation is called *global* if a single pair of transformation functions are used to map one image onto the other [13]. Therefore a change in any one of the matching parameters influences the transformation of the image as a whole. Global transformation methods are commonly used to register images which contain little or no local geometric distortion. Given a sufficient number of control points, the parameters of any transformation can be derived, either through approximation or interpolation. The problem with methods using globally defined transformation functions is that a single local mismatch will influence the whole transformation.

5.3.4 Local Methods

In a global method, only one pair transformation functions is needed to align two images. However, one pair of transformation functions may not be able to describe geometric differences between the two images at every point. A local method uses a number of local mapping functions which are combined to obtain a global mapping function. Only control points sufficiently close, or perhaps weighted by their proximity, influence the mapping transformation.

Goshtasby [39,40] has proposed several types of locally-sensitive mapping functions. Piecewise linear [39] and piecewise cubic [40] mapping functions assume triangulation of both images. Given n points in an image, divide the convex hull of the points into triangular regions. Each triangle characterizes local geometric differences between the images and the vertices of the triangles are used as control points. A corresponding linear or cubic mapping function is then found for each triangle. Burr [15] modeled a locally sensitive transformation function by an elastic grid. Table 5-1 compares five differing transformation methods, to be discusssed in the forthcoming sections, with respect to the properties discussed in Sections 5.3.1 to 5.3.4.

Transformation Method	*Local/Global*	*Interpolation / Approximation*
Affine	Global	Approximation
Polynomial	Global	Approximation
Surface-Spline	Local	Interpolation
Weighted Polynomial	Local	Approximation
Polynomial Fitting	Global	Interpolation

Table 5-1. A Comparison of Transformation Methods

5.3.5 Geometric Nature of Transformations

The term "*elasticity*" is used to describe the geometric nature of the transformations. A matching transformation can be classified as either *rigid, affine*, *projective* or *curved* [112]. These categories, indicating the degree of elasticity of the transformation, have been selected to show a clear distinction in geometrical properties.

5.3.5.1 Rigid

A transformation is *rigid* if the distance between any two points in the first image is preserved when these two points are mapped onto the second image. Rigid transformations can be decomposed into translation and rotation. In 2-D, the point (x, y) is transformed into the point (x', y') using the formula:

$$[x' \quad y'] = [x \quad y] \begin{bmatrix} \cos\theta & \sin\theta \\ -\sin\theta & \cos\theta \end{bmatrix} + \begin{bmatrix} t_x \\ t_y \end{bmatrix} \tag{5.4}$$

where θ denotes the rotation angle, and $\begin{bmatrix} t_x \\ t_y \end{bmatrix}$ the translation vector.

5.3.5.2 Affine

A transformation is *affine* when any straight line in the first image is mapped onto a straight line in the second image, while parallelism is preserved. Affine transformations can be decomposed into a linear transformation and a translation. In 2-D, the transformation is described by the formula:

$$[x' \quad y'] = [x \quad y] \begin{bmatrix} a_{11} & a_{12} \\ a_{21} & a_{22} \end{bmatrix} + \begin{bmatrix} t_x \\ t_y \end{bmatrix} \tag{5.5}$$

In Equation (5.5), if the last term is absent, the resulting transformation is linear. Examples of non-rigid affine transformations include both uniform and non-uniform scaling and shearing.

5.3.5.3 Projective

A *projective* (or perspective) transformation maps any straight line in the first image onto a straight line in the second image; parallelism between straight lines is in general not preserved. Projective transformations can be represented by a linear transformation in a higher dimensional space. In 2-D, the transformation is described by the formula:

$$[x' \quad y' \quad 1] = [x \quad y \quad 1] \begin{bmatrix} a_{11} & a_{12} & a_{13} \\ a_{21} & a_{22} & a_{23} \\ a_{31} & a_{32} & a_{33} \end{bmatrix} \tag{5.6}$$

5.3.5.4 Curved

Curved transformations may map a straight line onto a curve. In 2-D this is formulated as follows:

$$(x', y') = F(x, y) \tag{5.7}$$

where F denotes any function mapping the points in the first image onto points in the second image. A well known class of curved transformation functions are polynomial transformations, described in Section 5.5.

The four kinds of transformation, illustrating both local and global variants, are shown in Figure 5-4. Note that the local transformations may induce gaps or overlaps.

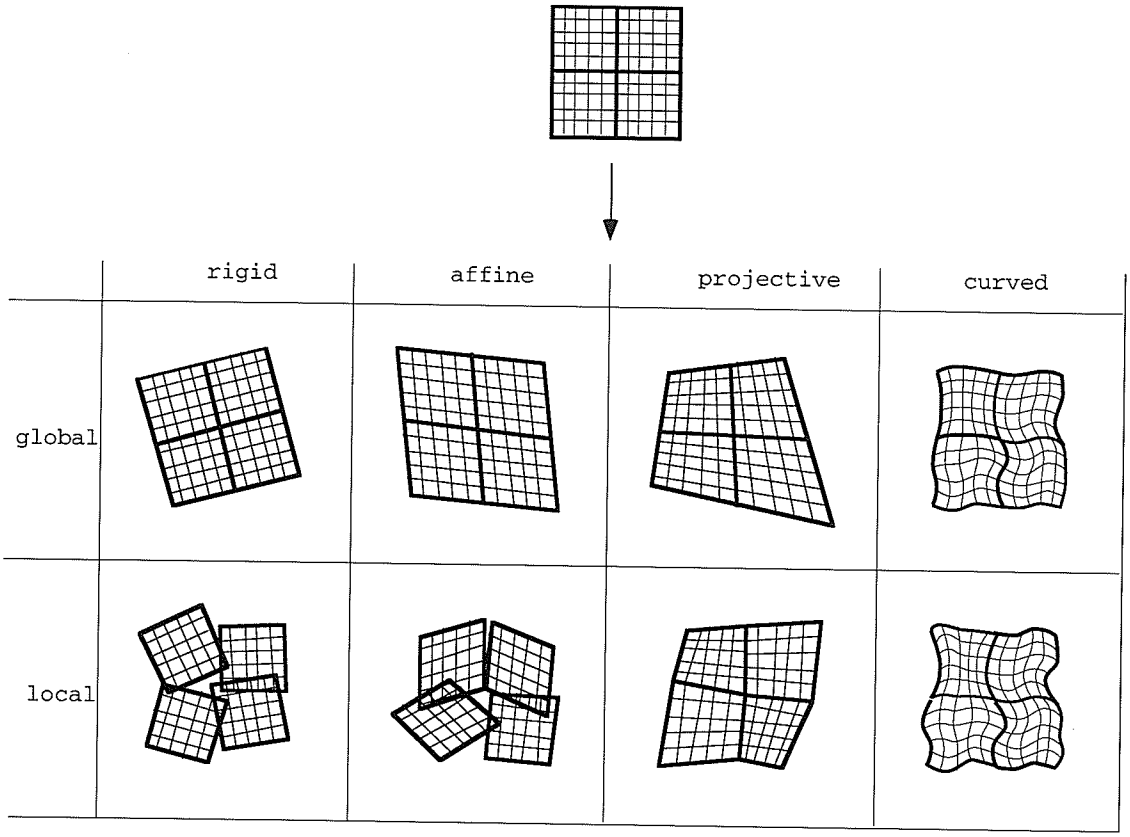

Figure 5-4. Examples of 2-D Transformations

A consequence of the above categorization into rigid, affine, projective and curved mappings is that rigid transformations are a subset of affine transformations which in turn are a subset of projective transformations, which in turn are a subset of curved transformations. For example, the 2-D projective transformation with $a_{13} = a_{23} = 0$ and $a_{33} = 1$ is affine, with $a_{31} = t_x$ and $a_{32} = t_y$.

It is assumed that the kind of transformation used in matching is adequate to describe the actual distortion in the image. If the selected transformations do not truly model the geometric difference between the images, an overall accurate match will not be obtained, even when accurate control-point correspondences are used in the matching. This may also result in a transformation introducing distortions that were

not present in the images beforehand. Global rigid transformations suffice when matching relatively stable areas such as cranial images from different modalities. Global affine matching is used in situations when image scaling or gantry tilt induces linear distortions. The use of local rigid and local affine transformations is resticted to certain categories of registration, such as temporal registration, because the transformed image contains gaps that are not present in the original images. Curved transformations are used when the distortion is geometric or non-linear, such as in modality induced distortion, or multimodal or template registration.

5.3.6 Least Squares Approximation

The set of parameters associated with a particular mapping function can be found by least-squares fitting [59], that is by minimizing:

$$E = \sum_{i=1}^{n} \left[\left(u_i - x_i'\right)^2 + \left(v_i - y_i'\right)^2 \right] \tag{5.8}$$

where $\left(u_i - x_i'\right)^2 + \left(v_i - y_i'\right)^2$ is the squared distance between the control point (u_i, v_i) in the reference image and the transformed point (x_i', y_i') in the distorted image. For details on Least Squares Approximation refer to Appendix A.1.

5.3.7 Weighted Methods

One limitation of the least squares method is that when the images have local geometric differences or the control points in a local neighborhood are inaccurate, the local measurement inaccuracy averages out equally over the whole image. Goshtasby [37] introduces Weighted Least Squares to minimize the problem of local geometric differences. To localize the least-squares method, define a weight function that

represents the contribution or influence of the ith control point on point (x,y) by the inverse distance of the ith control point to point (x,y) as:

$$W_i(x,y) = \left[(x - x_i)^2 + (y - y_i)^2\right]^{-\frac{1}{2}} \tag{5.9}$$

W_i would become infinity at the control points (when $x = x_i$ and $y = y_i$). Therefore instead of using Equation (5.9) the following weight function proposed by McLain [66] should be used:

$$W_i(x,y) = \left[\delta + (x - x_i)^2 + (y - y_i)^2\right]^{-\frac{1}{2}} \tag{5.10}$$

The parameter δ determines the influence of distant measurements (control points) on an approximating point. The smaller the value of δ, the smaller the influence of the distant control points; the approximating transformation function therefore follows the local measurements more rigorously. Conversely, the larger the value of δ, the less the influence of nearby control points on the approximating value. Incorporating the weighting function into the least-squares formula of Equation (5.8) gives an equation for weighted least squares:

$$E = \sum_{i=1}^{n}\left[(u_i - x_i')^2 + (v_i - y_i')^2\right] W_i(x,y) \tag{5.11}$$

5.4 Affine Transformations

For certain kinds of mapping function, the form of the distortion between the two images is known. This usually occurs in misaligned images or images containing linear distortion, i.e. images taken from the same viewing angle, but from a different position. This distortion usually takes the form of a change in scale, change in rotation angle, horizontal and/or vertical displacement or shear. Such images are usually aligned using an affine transformation [43,114,120]. It is considered a global transformation in general, since the overall geometric relationships between two points do not change.

5.4.1 Affine Differences

In *homogeneous* coordinates, an n-dimensional space is represented by $n+1$ dimensions; i.e., two-dimensions where the position of a point is given by the pair (x,y), is represented by three coordinates (x,y,h), where h , the homogeneous coordinate, is an arbitrary number [92]. Four kinds of affine differences will be described here, namely translation, rotation, scaling and shearing [92].

5.4.1.1 Translation

Translation is defined as a displacement of the plane in a horizontal and/or vertical direction. The transformation can be represented by the two equations $x' = x + t_x$ and $y' = y + t_y$. Assuming homogeneous coordinates, with h=1, the translation can be expressed in matrix form as follows:

$$[x' \quad y' \quad 1] = [x \quad y \quad 1] \begin{bmatrix} 1 & 0 & 0 \\ 0 & 1 & 0 \\ t_x & t_y & 1 \end{bmatrix} \tag{5.12}$$

The transformation matrix at the right is denoted by T_t.

5.4.1.2 Rotation

When a plane is rotated by an angle θ about the origin (clockwise), the transformation is known as *rotation* and can be represented by the two equations $x' = x\cos\theta - y\sin\theta$ and $y' = x\sin\theta + y\cos\theta$ which in matrix form becomes:

$$[x' \quad y' \quad 1] = [x \quad y \quad 1]\begin{bmatrix} \cos\theta & \sin\theta & 0 \\ -\sin\theta & \cos\theta & 0 \\ 0 & 0 & 1 \end{bmatrix} \tag{5.13}$$

The transformation matrix at the right is denoted by T_r.

5.4.1.3 Scaling

Distortion of a plane by stretching or compressing it is known as *scaling*. A scaling in the x and y directions can be represented by $x' = S_x x$ and $y' = S_y y$ respectively, where the constants S_x and S_y are the x and y scaling factors respectively. The scaling can be expressed in matrix form as follows:

$$[x' \quad y' \quad 1] = [x \quad y \quad 1]\begin{bmatrix} S_x & 0 & 0 \\ 0 & S_y & 0 \\ 0 & 0 & 1 \end{bmatrix} \tag{5.14}$$

The transformation matrix at the right is denoted by T_s. If the scaling factor is greater than 1, the scaling transformation is known as *stretching*, otherwise if it is between 0

and 1, it is known as *compression*. If both S_x and S_y are equal, then the scaling is considered *uniform* $(S = S_x = S_y)$ otherwise it is considered *non-uniform*.

5.4.1.4 Shear

A transformation is called a *shear* when either all its x-coordinates or all its y-coordinates remain constant while the other coordinates are increased in proportion to x or y respectively. A shearing in the x and y directions can be represented by $x' = x + h_x y$ and $y' = h_y x + y$ respectively, where the constants h_x and h_y are the x and y shearing factors respectively. A shearing can be expressed in matrix form as follows:

$$[x' \quad y' \quad 1] = [x \quad y \quad 1] \begin{bmatrix} 1 & h_y & 0 \\ h_x & 1 & 0 \\ 0 & 0 & 1 \end{bmatrix} \tag{5.15}$$

The transformation matrix at the right is denoted by T_{sh}.

5.4.2 RST Mapping Function

When two images have rotational, scaling and/or translational differences, corresponding points in the two images can be related to each other by an RST transformation. In order to obtain the entire RST transformation, it is necessary to combine the translation, rotation and scaling transformations of Section 5.4.1. Therefore, the transformation which maps the set of points from the distorted image to the corresponding set of points in the reference image involves a rotation, followed by uniform-scaling, followed by translation, or: $T = T_r T_s T_t$ [120]. Therefore, an RST transformation with parameters (S, θ, t_x, t_y) is defined as:

$$[x' \quad y' \quad 1] = [x \quad y \quad 1]\begin{bmatrix} S\cos\theta & S\sin\theta & 0 \\ -S\sin\theta & S\cos\theta & 0 \\ t_x & t_y & 1 \end{bmatrix} \tag{5.16}$$

or

$$x' = S(x\cos\theta - y\sin\theta) + t_x \tag{5.17a}$$

$$y' = S(x\sin\theta + y\cos\theta) + t_y \tag{5.17b}$$

S is the scaling factor, θ is the rotational difference and (t_x, t_y) are the translational differences of the distorted image with respect to the reference image. The transformation of images that have rotational, scaling and translational differences requires knowledge of at least two corresponding control points in each of the images. If n corresponding points from the two images are available, then S, θ, t_x and t_y can be estimated by minimizing the sum of squared errors. The least squares approximation involves estimating a set of parameters which minimizes the squared distance between the set of control points and the set of transformed points.

To minimize E with respect to S, θ, t_x and t_y, find the partial derivatives of E with respect to S, θ, t_x and t_y, then set them equal to zero (See Appendix A..2.1), and solve the set of linear equations. For simplicity replace $S\cos\theta$ by a, $S\sin\theta$ by b, t_x by h and t_y by k and minimize for a, b, h and k. Then Equation (5.8) becomes:

$$E = \sum_{i=1}^{n} \left\{ \left[u_i - (ax_i - by_i + h)\right]^2 + \left[v_i - (bx_i + ay_i + k)\right]^2 \right\} \tag{5.18}$$

This leads to the following set of linear equations (See Appendix A.2.1):

$$
\begin{aligned}
a\left(\sum_{i=1}^{n}(x_i^2+y_i^2)\right) + h\left(\sum_{i=1}^{n}x_i\right) + k\left(\sum_{i=1}^{n}y_i\right) &= \sum_{i=1}^{n}(u_i x_i + v_i y_i) \\
b\left(\sum_{i=1}^{n}(x_i^2+y_i^2)\right) - h\left(\sum_{i=1}^{n}y_i\right) + k\left(\sum_{i=1}^{n}x_i\right) &= \sum_{i=1}^{n}(v_i x_i - u_i y_i) \\
a\left(\sum_{i=1}^{n}x_i\right) - b\left(\sum_{i=1}^{n}y_i\right) + nh &= \sum_{i=1}^{n}u_i \\
a\left(\sum_{i=1}^{n}y_i\right) + b\left(\sum_{i=1}^{n}x_i\right) + nk &= \sum_{i=1}^{n}v_i
\end{aligned}
\tag{5.19}
$$

The system of linear equations can be expressed in matrix form in Figure 5-5 which can be solved using Gaussian elimination with back-substitution, LU decomposition or Singular Value Decomposition (SVD) [14].

$$
\begin{bmatrix}
\sum_{i=1}^{n}(x_i^2+y_i^2) & 0 & \sum_{i=1}^{n}x_i & \sum_{i=1}^{n}y_i \\
0 & \sum_{i=1}^{n}(x_i^2+y_i^2) & -\sum_{i=1}^{n}y_i & \sum_{i=1}^{n}x_i \\
\sum_{i=1}^{n}x_i & -\sum_{i=1}^{n}y_i & n & 0 \\
\sum_{i=1}^{n}y_i & \sum_{i=1}^{n}x_i & 0 & n
\end{bmatrix}
\begin{bmatrix} a \\ b \\ h \\ k \end{bmatrix}
=
\begin{bmatrix}
\sum_{i=1}^{n}(u_i x_i + v_i y_i) \\
\sum_{i=1}^{n}(v_i x_i - u_i y_i) \\
\sum_{i=1}^{n}u_i \\
\sum_{i=1}^{n}v_i
\end{bmatrix}
$$

Figure 5-5. Linear System for RST Transformation with Uniform Scaling

The terms h and k represent the respective x and y translations. However the scaling factor S and rotation angle θ must be obtained jointly from the two quantities, $S\cos\theta$ and $S\sin\theta$ If $a = S\cos\theta$ and $b = S\sin\theta$ then:

$$
S = \sqrt{a^2+b^2} \qquad \textit{and} \qquad \theta = \arctan(b/a)
$$

Now for each point *(x,y)* in the distorted image, Equation (5.17) has to be solved to determine the corresponding point in the transformed image.

The RST transformation could be expanded to include images containing non-uniform scaling. The transformation functions would have equations of the form given below in Equation (5.20).

$$x' = S_x(x\cos\theta - y\sin\theta) + t_x \tag{5.20a}$$

$$y' = S_y(x\sin\theta + y\cos\theta) + t_y \tag{5.20b}$$

Replacing $S_x\cos\theta$ by a, $S_x\sin\theta$ by b, $S_y\sin\theta$ by c, $S_y\cos\theta$ by d, t_x by h and t_y by k gives Equation (5.21).

$$E = \sum_{i=1}^{n}\left(\left[u_i - ax_i + by_i - h\right]^2 + \left[v_i - cx_i - dy_i - k\right]^2\right) \tag{5.21}$$

Find the partial derivatives of E with respect to a, b, c, d, h and k and set them equal to zero, to obtain the following set of linear equations (See Appendix A.2.2), expressed in matrix form, shown in Figure 5-6.

$$\begin{bmatrix} \sum x_i^2 & -\sum x_iy_i & 0 & 0 & \sum x_i & 0 \\ -\sum x_iy_i & \sum y_i^2 & 0 & 0 & -\sum y_i & 0 \\ 0 & 0 & \sum x_i^2 & \sum x_iy_i & 0 & \sum x_i \\ 0 & 0 & \sum x_iy_i & \sum y_i^2 & 0 & \sum y_i \\ \sum x_i & -\sum y_i & 0 & 0 & n & 0 \\ 0 & 0 & \sum x_i & \sum y_i & 0 & n \end{bmatrix} \begin{bmatrix} a \\ b \\ c \\ d \\ h \\ k \end{bmatrix} = \begin{bmatrix} \sum x_iu_i \\ -\sum y_iu_i \\ \sum x_iv_i \\ \sum y_iv_i \\ \sum u_i \\ \sum v_i \end{bmatrix}$$

Figure 5-6. Linear System for RST Transformation with Non-Uniform Scaling

5.5 Polynomial Transformation

In images where the precise form of the distortion is not known, a general transformation is required. This usually occurs in images containing geometric or non-linear distortion, taken from different viewpoints or from different sensors. For this reason curved transformations such as *polynomial* transformations are used. The polynomials may be defined as first-, second-, third-, fourth- or fifth degree. The most common forms of polynomial are first, second and third degree polynomials, known as linear, quadratic and cubic polynomials respectively. First-degree polynomials include only translational, scaling and rotational distortions, whereas second-degree polynomials include shear and third-degree polynomials include non-linear distortions [72], shown in Equations (5.22a), (5.22b) and (5.22c) respectively.

$$a_0 + a_1 x + a_2 y \tag{5.22a}$$

$$a_0 + a_1 x + a_2 y + a_3 xy + a_4 x^2 + a_5 y^2 \tag{5.22b}$$

$$a_0 + a_1 x + a_2 y + a_3 xy + a_4 x^2 + a_5 y^2 + a_6 x^2 y + a_7 xy^2 + a_8 x^3 + a_9 y^3 \tag{5.22c}$$

Steiner and Kirby [101] used polynomials of degree one, Nack [74] used polynomials of degree two, and Van Wie and Stein [114] used polynomials of degree three. Traditionally the polynomial transformation is a global approximation method, but coupled together with weighted least squares, some of the limitations of global methods can be overcome.

5.5.1 Surface Fitting with Polynomials

Transformations involving surface polynomials, more commonly called *bivariate* polynomials (i.e. polynomials in two variables) have the following general form:

$$x' = \sum_{i=0}^{m}\sum_{j=0}^{i} \alpha_{ij} x^j y^{i-j} \tag{5.23a}$$

$$y' = \sum_{i=0}^{m}\sum_{j=0}^{i} \beta_{ij} x^j y^{i-j} \tag{5.23b}$$

where (x,y) denotes the position of the control points in the distorted image, (x', y') denotes the position of the control points in the transformed image, and α_{ij} and β_{ij} are the constant polynomial coefficients. The order of the polynomial is represented by m.

This error, E, is a function of parameters α_{ij} and β_{ij}, so to find the parameters that produce the least error, determine the partial derivatives of E with respect to the parameters and set them equal to zero. This gives a set of $T = (m+2)(m+1)/2$ linear equations, known as the *normal* equations. As an example, consider a polynomial of degree 2, i.e. $m = 2$. The Equations in (5.23), when expanded assume the simplified form:

$$x' = a_0 + a_1 x + a_2 y + a_3 xy + a_4 x^2 + a_5 y^2 \tag{5.24a}$$

$$y' = b_0 + b_1 x + b_2 y + b_3 xy + b_4 x^2 + b_5 y^2 \tag{5.24b}$$

where for convenience sake, the coefficients α_{ij} and β_{ij} have been replaced respectively by a_k and b_k, for $k = 0,\ldots,l-1$ with $l = \sum_{i=0}^{m}\sum_{j=0}^{i} 1$. Using n corresponding control points in the images, the parameters of the mapping function are determined by minimizing the sum of squared errors:

$$E = \sum_{i=1}^{n} \left\{ \begin{array}{l} \left[u_i - \left(a_0 + a_1 x_i + a_2 y_i + a_3 x_i y_i + a_4 x_i^2 + a_5 y_i^2 \right) \right]^2 \\ + \left[v_i - \left(b_0 + b_1 x_i + b_2 y_i + b_3 x_i y_i + b_4 x_i^2 + b_5 y_i^2 \right) \right]^2 \end{array} \right\} \tag{5.25}$$

To minimize E from Equation (5.25) with respect to the parameters $a_0, a_1, a_2, a_3, a_4, a_5$ and $b_0, b_1, b_2, b_3, b_4, b_5$, find the partial derivatives of E with respect to each of the aforementioned parameters, then set each equal to zero (See Appendix A.3), and solve the set of linear equations. This leads to the following set of linear equations for a_0, a_1, a_2, a_3, a_4 and a_5 expressed in matrix form in Figure 5-7.

$$\begin{bmatrix} n & \sum x_i & \sum y_i & \sum x_i y_i & \sum x_i^2 & \sum y_i^2 \\ \sum x_i & \sum x_i^2 & \sum x_i y_i & \sum x_i^2 y_i & \sum x_i^3 & \sum x_i y_i^2 \\ \sum y_i & \sum x_i y_i & \sum y_i^2 & \sum x_i y_i^2 & \sum x_i^2 y_i & \sum y_i^3 \\ \sum x_i y_i & \sum x_i^2 y_i & \sum x_i y_i^2 & \sum x_i^2 y_i^2 & \sum x_i^3 y_i & \sum x_i y_i^3 \\ \sum x_i^2 & \sum x_i^3 & \sum x_i^2 y_i & \sum x_i^3 y_i & \sum x_i^4 & \sum x_i^2 y_i^2 \\ \sum y_i^2 & \sum x_i y_i^2 & \sum y_i^3 & \sum x_i y_i^3 & \sum x_i^2 y_i^2 & \sum y_i^4 \end{bmatrix} \begin{bmatrix} a_0 \\ a_1 \\ a_2 \\ a_3 \\ a_4 \\ a_5 \end{bmatrix} = \begin{bmatrix} \sum u_i \\ \sum x_i u_i \\ \sum y_i u_i \\ \sum x_i y_i u_i \\ \sum x_i^2 u_i \\ \sum y_i^2 u_i \end{bmatrix}$$

Figure 5-7. Linear System for a Quadratic Polynomial Transformation

The parameters $b_0, b_1, b_2, b_3, b_4, b_5$ are similarly derived. Goshtasby [37] has introduced adaptations to the basic polynomial transformation, including the use of orthogonal polynomials and weighted orthogonal polynomials as the terms of the polynomial mapping.

5.5.2 Polynomial Interpolation

One alternative to the polynomial mapping function described above, is a polynomial using interpolation. Given n non-collinear control points in each image, this methods fits a polynomial with n coefficients to the points, such that $\sum_{j=0}^{m}\sum_{k=0}^{j}1=n$. The polynomials take the same general form as those shown previously in Equation (5.11). The n coefficients of the polynomial can be derived by substituting the control points into Equation (5.23) and solving the set of n linear equations:

$$\sum_{j=0}^{m}\sum_{k=0}^{j}\alpha_{jk}x_i^k y_i^{j-k} = u_i \qquad (i=1,\ldots,n) \tag{5.26a}$$

$$\sum_{j=0}^{m}\sum_{k=0}^{j}\beta_{jk}x_i^k y_i^{j-k} = v_i \qquad (i=1,\ldots,n) \tag{5.26b}$$

Although the transformation function of Equation (5.26) maps control points from the images to fall exactly on top of each other, as n increases, the degree of the polynomial also increases. For example if n=21, then $\sum_{j=0}^{m}\sum_{k=0}^{j}1=21$, therefore the degree of the polynomial m=5, contains 21 coefficients. If the number of control points to be used in the transformation is large, polynomial interpolation transformations behave erratically as the degree of the polynomial increases, introducing high fluctuations in the interpolated values. Polynomial fitting is therefore not recommended for determining transformation functions in general, it is preferable to use least-squares approximation, splines or other piecewise interpolation methods.

5.5.3 Bilinear Transformation

A classical transformation known as a *bilinear* transformation [112] is derived from Equation (5.27) when the degree of the polynomial is two, i.e. $m = 2$. The resulting transformation function, shown in Equation (5.28) maps horizontal and vertical lines in the distorted image onto straight lines in the reference image, however a line in any other direction will become curved. It is neither an affine transformation, nor a bivariate polynomial, but it has been included in this section because it introduces a curved warp. Figure 5-8 shows examples of both the local and global variants of a bilinear transformation.

$$x' = \sum_{i=0}^{m}\sum_{j=0}^{m} a_{ij} x^i y^j \tag{5.27a}$$

$$y' = \sum_{i=0}^{m}\sum_{j=0}^{m} b_{ij} x^i y^j \tag{5.27b}$$

$$x' = a_{00} + a_{10}x + a_{01}y + a_{11}xy \tag{5.28a}$$

$$y' = b_{00} + b_{10}x + b_{01}y + b_{11}xy \tag{5.28b}$$

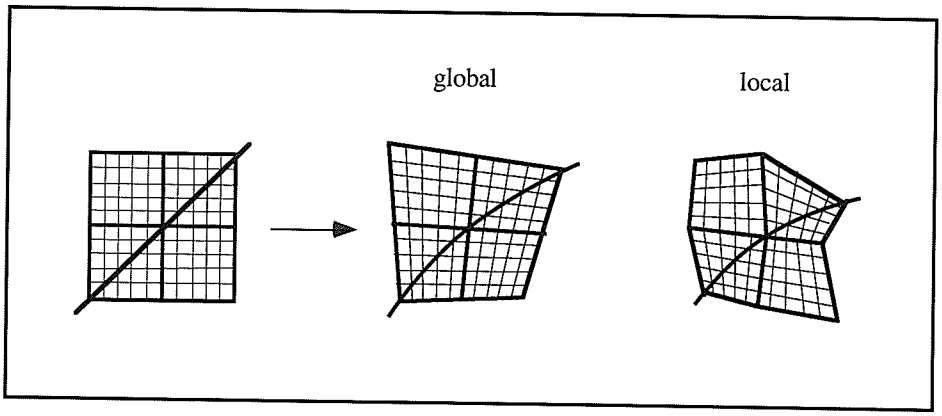

Figure 5-8. Examples of Bilinear Transformations

5.6 Surface-Spline Transformation

The *surface-spline* transformation, sometimes known as a *thin-plate spline*, is a local method using piecewise interpolation. Goshtasby [38], Flusser [27] and Barrodale *et al.* [8] define a surface-spline mapping function to represent the transformation of an image. This method uses two splines to represent the X-component and the Y-component of a mapping function. The mapping function maps corresponding control points in the two images exactly on top of each other and maps other points in the images by interpolation. A mapping function determined in this manner would be sensitive to local geometric distortion between the images because the value of a surface at a point *(x,y)* is determined by the nearby control points and the influence of the control point decreases as the distance between it and the point *(x,y)* increases. In order to use a surface-spline, three or more non-collinear points must be specified. The spline-function can be decomposed into an affine transformation together with *principal warps* [12] which are affine-free geometric deformations of progressively smaller geometrical scale.

5.6.1 Surface Fitting with Splines

Let *(x,y)* and *(u,v)* denote the positions of corresponding points in the distorted and reference images respectively. Given the positions of n corresponding control points in the images $\{(x_j, y_j), (u_j, v_j), j = 1,\ldots,n\}$, define two mapping functions *f(x,y)* and *g(x,y)* such that:

$$u_j = f(x_j, y_j) \quad \text{and} \quad v_j = g(x_j, y_j) \qquad j = 1,\ldots,n \tag{5.29}$$

The equation of the surface spline function as given by Harder and Desmarais [47] is:

$$f(x_j, y_j) = a_0 + a_1 x_j + a_2 y_j + \sum_{i=1}^{n} F_i r_{ij}^2 \ln r_{ij}^2 \tag{5.30}$$

where

$$r_{ij}^2 = (x_j - x_i)^2 + (y_j - y_i)^2 \tag{5.31}$$

In Equation (5.30), (x_j, y_j) is the position of the *jth* control point in the distorted image and $f(x_j, y_j)$ is the X-component of the point corresponding to (u_j, v_j) in the reference image. Note that when $i = j$, use 0 instead of $r_{ij}^2 \ln r_{ij}^2$.

The coefficients of Equation (5.30) $a_0, a_1, a_2, F_i;\ i = 1,\ldots,n$ are determined by substituting the coordinates of corresponding control points into Equation (5.30) and using Gaussian Elimination to solve the resulting set of *(n+3)* linear equations given in Figure 5-9, known as the *equilibrium* equations.

$$\begin{aligned} &f(x_j, y_j) = u_j \qquad j = 1,\ldots,n \\ &\sum_{j=1}^{n} F_j = \sum_{j=1}^{n} F_j x_j = \sum_{j=1}^{n} F_j y_j = 0 \end{aligned} \tag{5.32}$$

$$\begin{bmatrix} 0 & 0 & 0 & 1 & 1 & \cdots & 1 \\ 0 & 0 & 0 & x_1 & x_2 & \cdots & x_n \\ 0 & 0 & 0 & y_1 & y_2 & \cdots & y_n \\ 1 & x_1 & y_1 & 0 & r_{21}^2 \ln r_{21}^2 & \cdots & r_{n1}^2 \ln r_{n1}^2 \\ 1 & x_2 & y_2 & r_{12}^2 \ln r_{12}^2 & 0 & \cdots & r_{n2}^2 \ln r_{n2}^2 \\ \cdot & \cdot & \cdot & \cdot & \cdot & & \cdot \\ \cdot & \cdot & \cdot & \cdot & \cdot & & \cdot \\ \cdot & \cdot & \cdot & \cdot & \cdot & & \cdot \\ 1 & x_n & y_n & r_{1n}^2 \ln r_{1n}^2 & r_{2n}^2 \ln r_{2n}^2 & \cdots & 0 \end{bmatrix} \begin{bmatrix} a_0 \\ a_1 \\ a_2 \\ F_1 \\ F_2 \\ \cdot \\ \cdot \\ \cdot \\ F_n \end{bmatrix} = \begin{bmatrix} 0 \\ 0 \\ 0 \\ u_1 \\ u_2 \\ \cdot \\ \cdot \\ \cdot \\ u_n \end{bmatrix}$$

Figure 5-9. Linear System for the Surface-Spline Transformation

The surface which is obtained represents the X-component mapping function because the surface value at a control point in the distorted image is equal to the X-component of the corresponding control point in the reference image. The surface $g(x_j, y_j)$, representing the Y-component mapping function, is similarly determined:

$$g(x_j, y_j) = b_0 + b_1 x_j + b_2 y_j + \sum_{i=1}^{n} G_i r_{ij}^2 \ln r_{ij}^2 \tag{5.33}$$

$$\begin{aligned} & g(x_j, y_j) = v_j \qquad j = 1, \ldots, n \\ & \sum_{j=1}^{n} G_j = \sum_{j=1}^{n} G_j x_j = \sum_{j=1}^{n} G_j y_j = 0 \end{aligned} \tag{5.34}$$

Now the distorted image can be transformed pixel by pixel using the functions f and g. This mapping function is sensitive to local geometric distortions between the two images and the matching error at the control points is zero. For a brief mathematical analysis of surface-splines, refer to Appendix B.

It should be noted that Harder and Desmarais [47] proposed two modifications of Equation (5.30) in the form of smoothing with elastic springs and distributed loads. Flusser [27] proposes three adaptive variants of the surface-spline mapping algorithm; namely Projective Mapping, Bilinear Mapping and Affine Mapping. Each mapping algorithm divides the distorted image into smaller sub-regions of simple shapes (squares, triangles etc.). Each sub-region is then separately transformed by a simple local transformation.

5.7 Registration Error

To determine the accuracy of the above-mentioned techniques, the error between the transformed control points (x_i', y_i') and the reference control points (u_i', v_i') $(i = 1,...,n)$ is calculated. The registration error between each pair of corresponding control points after the transformation is defined as the *square-root-error* (SRE), denoted by E_{SRE} :

$$E_{SRE} = \left\{ \left[u_i - x_i' \right]^2 + \left[v_i - y_i' \right]^2 \right\}^{\frac{1}{2}} \tag{5.35}$$

The square-root-error is essentially the Euclidean distance between corresponding control points in the distorted and reference images. A measure of the overall match between corresponding control points after the transformation can be given by the *mean-square-root-error* (MSRE), denoted E_{MSRE}:

$$E_{MSRE} = \frac{1}{n} \sum_{i=1}^{n} \left\{ \left[u_i - x_i' \right]^2 + \left[v_i - y_i' \right]^2 \right\}^{\frac{1}{2}} \tag{5.36}$$

The MSRE represents the normalized sum of the Euclidean distances calculated in Equation (5.34). Such an error estimate allows a comparison of transformations involving different numbers of control points.

5.8 Gray Level Resampling

Resampling is a gray-level interpolation which deals with the assignment of intensity values (gray levels) to pixels in the transformed image. Depending on the coefficients of the mapping functions, the geometric transformation of coordinates from the distorted image to the transformed image may yield non-integer values for x' and y'.

Because the transformed image, denoted D', is digital, its pixels are defined only at integer coordinates. Thus using non-integer values for x' and y' causes a mapping into locations of D' for which no gray levels are defined. The interpolation of gray level intensities can be represented by a function of the form:

$$D(x,y) \approx D'(x',y') \tag{5.37}$$

Where $D(x,y)$ is the grayscale intensity of the pixel at position (x,y) in the distorted image and $D'(x',y')$ is the grayscale intensity of the pixel at position (x',y') in the transformed image. There are two approaches to resampling, *gray-level transformation* and *reverse transformation*.

5.8.1 Reverse Transformation

In a *reverse transformation*, pixels from the transformed image are mapped onto the distorted image one at a time to establish their gray levels. This is achieved by using the reverse transformation, denoted T^{-1} to generate the spatial coordinates of each pixel in the distorted image:

$$T^{-1}(x',y') \rightarrow (x^*,y^*) \tag{5.38}$$

If a pixel in the transformed image falls between four pixels in the distorted image (See Figure 5-10(a)), when the reverse transformation is applied, then it's gray level is determined by an interpolation of the intensities at these four pixels.

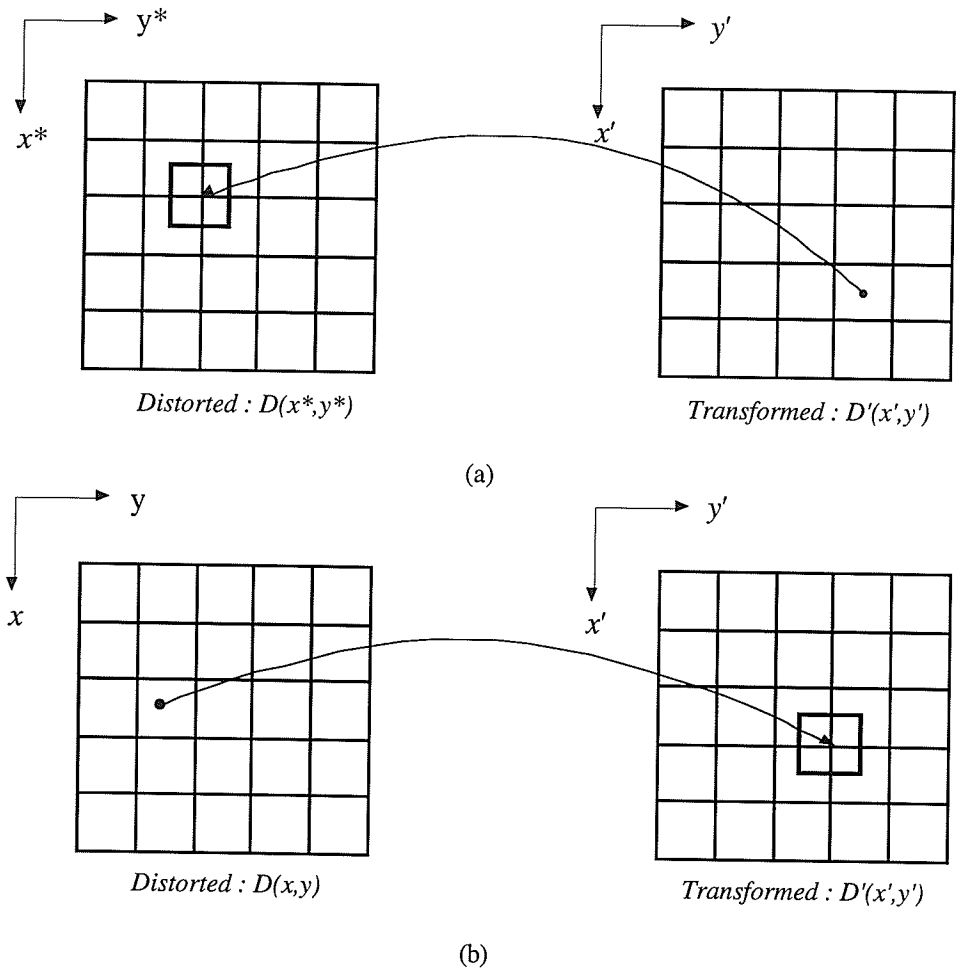

Figure 5-10. Forms of Resampling: (a) Reverse Transformation
(b) Gray-Level Transformation

5.8.2 Gray-Level Transformation

If a pixel in the distorted image maps to a position between four pixels in the transformed image, then its gray-level intensity is divided among the four pixels using an interpolation method, as shown in Figure 5-10(b).

5.8.3 Interpolation

The simplest method for interpolation is based on a nearest-neighbor approach. This method, also known as *zero-order interpolation*, selects the closest integer coordinate

neighbor to (x^*, y^*) and assigns the gray-level of this nearest neighbor to the pixel located at coordinates (x', y') in the transformed image (See Figure 5-11(a)).

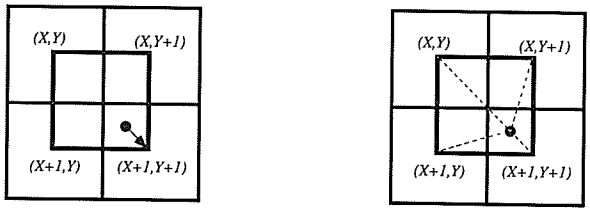

Figure 5-11. Forms of Interpolation: (a) Zero-Order Interpolation
(b) Bilinear Interpolation

A bilinear interpolation approach uses the gray levels of the four nearest neighbors to (x^*, y^*). The gray-level value of (x', y'), denoted $D'(x', y')$ can then be interpolated from the values of its neighbors by using the relationship:

$$\begin{aligned} D'(x', y') = (1-r_x)(1-r_y)D(X,Y) + (1-r_x)r_y D(X,Y+1) \\ + r_x(1-r_y)D(X+1,Y) + r_x r_y (X+1,Y+1) \end{aligned} \tag{5.39}$$

where r_x and r_y represent the non-integer components of x^* and y^* respectively. Zhou [121] proposed a number of methods for resampling gray levels including gray level interpolation and gray level approximation methods.

5.9 Results

To measure the performance of the three transformation methods discussed in the previous sections, consider the following examples, based on the synthetically distorted images introduced in Section 5.2. The goal was to transform the distorted

CT images of Figures 5-1, 5-2 and the MR image of Figure 5-3(b) to match the CT *reference image* shown below in Figure 5-12.

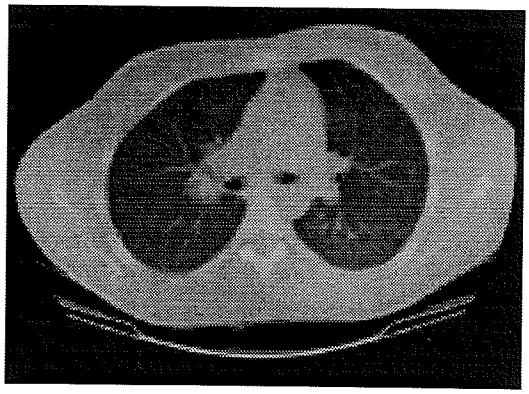

Figure 5-12. Reference Image

5.9.1 Images with Linear Distortion

The linear distortion contained within the image in Figure 5-1(c) is in the form of a 23° counterclockwise rotation. The affine transformation function of Section 5.4.1 incorporating uniform scaling was used to remove the distortion from Figure 5-1(c) , the resulting resampled image is shown in Figure 5-13.

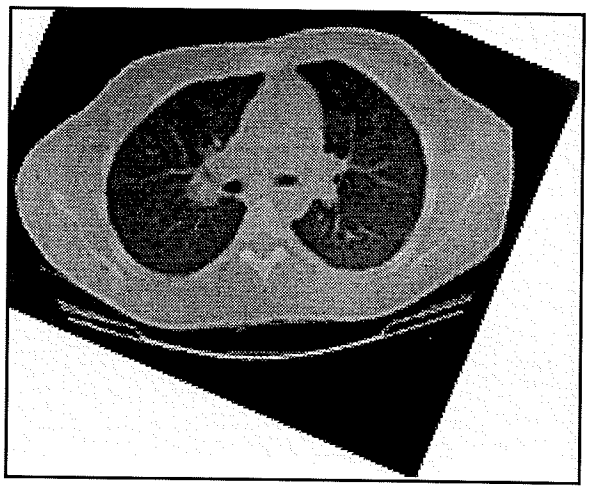

Figure 5-13. Transformed Image of Figure 5-1(c)

The transformation parameters are determined to be S=1.00, θ=-22.31, t_x=-53.26 and t_y=40.36. To determine the accuracy of this technique, the MSRE was calculated between the corresponding control points, both before and after registration. The error for the corresponding control-points in the reference and distorted images is MSRE=20.68. The error for the corresponding control-points in the reference and transformed images is MSRE=2.09, showing a definite improvement.

The distorted images of Figures 5-2(a) and 5-2(b) were transformed using the quadratic polynomial described in Section 5.5.1 which deals with affine distortions such as non-uniform scaling. The results are shown in Figures 5-14(a) and 5-14(b) respectively. The images could also have been resampled using a non-uniform version of the affine transformation described in Section 5.4.2, as using the affine transformation with uniform scaling would result in an inaccurate matching.

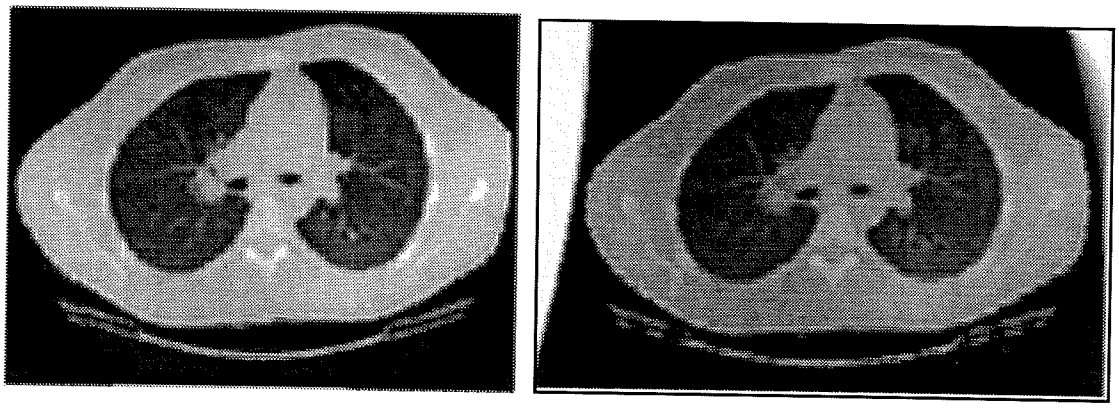

(a) (b)

Figure 5-14. Transformed Image using Quadratic Polynomial Warping
(a) Horizontal Scaling, (b) Vertical Scaling

The images were also resampled using the surface-spline mapping function of Section 5.6, with comparable results. The transformed images are shown in Figures 5-15(a)

and 5-15(b). The MSRE's for each of the control-points in the transformed images with respect to the control-points in the reference image are shown in Table 5-2.

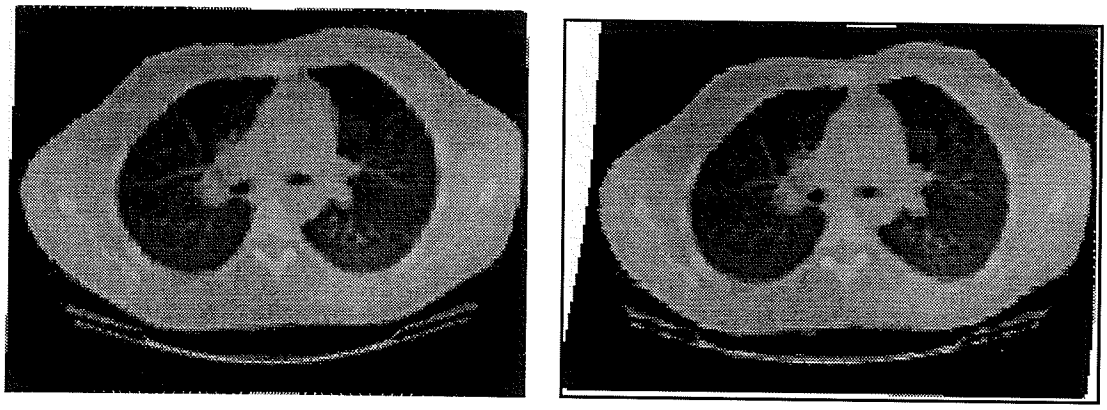

(a) (b)

Figure 5-15. Transformed Image using the Surface-Spline
(a) Horizontal Scaling, (b) Vertical Scaling

Distorted Image	*Transformation Method*	*MSRE before the Transformation*	*MSRE after the Transformation*
Horizontal Scaling (Figure 5-1(a))	Quadratic Polynomial (Figure 5-14(a))	28.98	2.01
	Surface-Spline (Figure 5-15(a))	28.98	0.63
Vertical Scaling (Figure 5-1(b))	Quadratic Polynomial (Figure 5-14(b))	16.20	1.61
	Surface-Spline (Figure 5-15(b))	16.20	0.0

Table 5-2. MSRE Estimates for the Linearly Distorted Images

It should be noted in Table 5-2 that the surface-spline transformation produces a MSRE at or near zero, as is consistent with a transformation method using interpolation. The MSRE for the quadratic polynomial is substantially reduced when compared to the MSRE of the images before the transformation.

5.9.2 Images with Geometric Distortion

The four images of Figure 5-2 all contain some form of local geometric distortion, so it would be inappropriate to attempt to transform them using a global approach such as polynomial approximation using a quadratic polynomial, as described in Section 5.5.1. Instead, all four images have been resampled using the interpolating surface-spline transformation described in Section 5.6, with the results shown in Figures 5-16 and 5-17 along with their associated distortion grids. These warped grids or "plates" give an indication of the type of transformation needed to transform the distorted image.

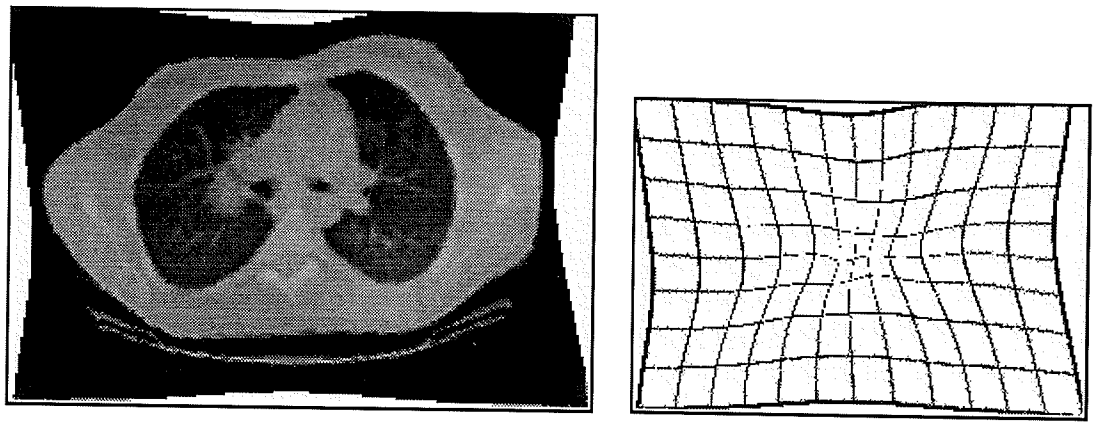

(a)

Figure 5-16. Transformed Image using Surface-Spline
Photometric Distortion: (a) Barrel

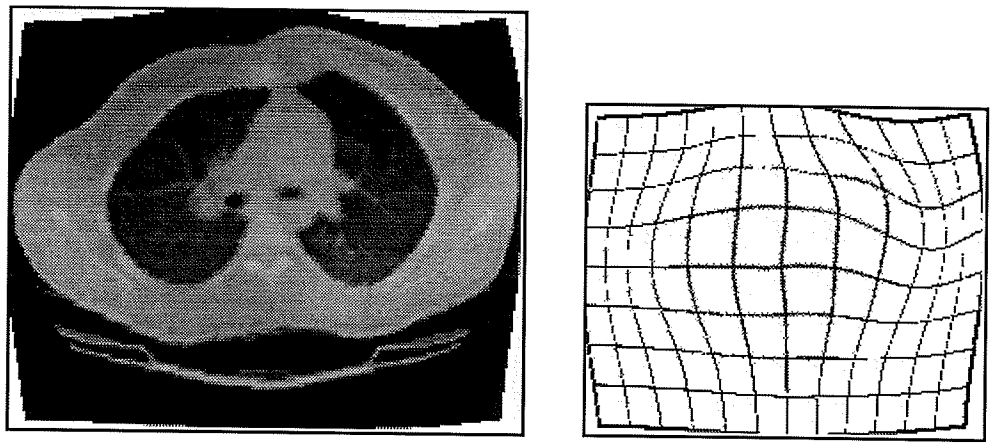

(b)

Figure 5-16. Transformed Image using Surface-Spline
Photometric Distortion: (b) Pincushion

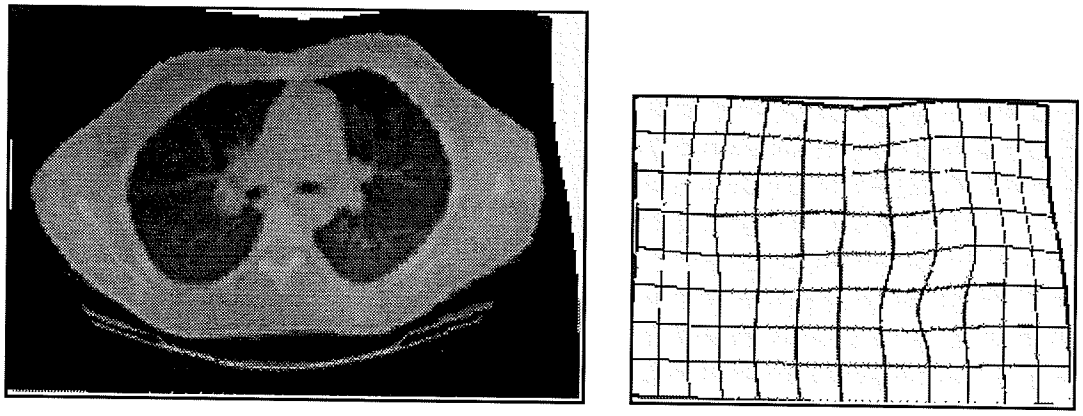

(a)

Figure 5-17. Transformed Image using Surface-Spline
Radial Distortion: (a) Horizontal

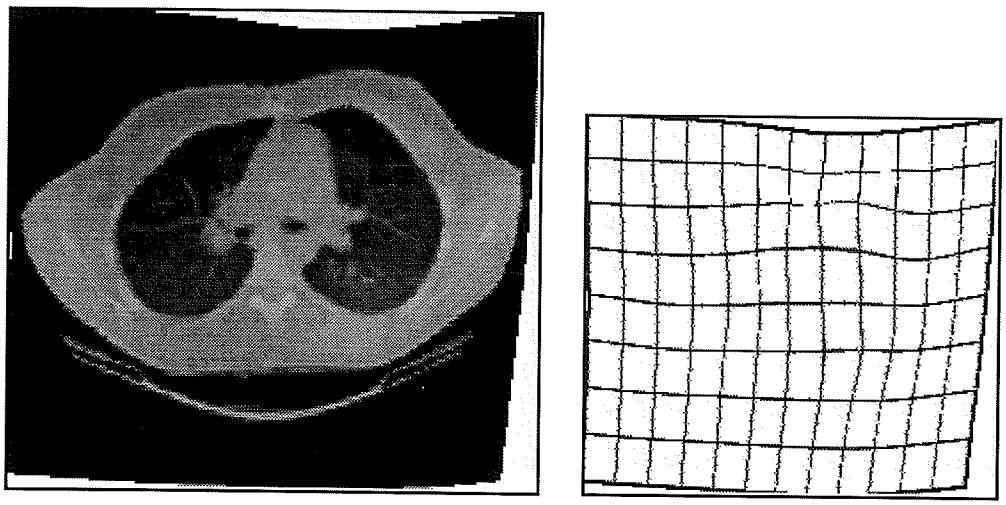

(b)

Figure 5-17. Transformed Image using Surface-Spline Radial Distortion: (b) Vertical

In most cases the results of the transformations seem to be adequate, although the accuracy of this method is dependent on the number of evenly distributed control points used. If the control-points are concentrated in one part of the image and sparse in the other, then the resulting transformation may provide an inaccurate registration. For example, Figures 5-16(b) contains an area to the top-right of the image where the matching has not been totally successful on the front body contour. The accuracy of this technique inceases substantially when the number of control-points used in the matching is increased. The images have also been resampled using a cubic polynomial which allows for geometric distortion, but which is global in nature and would have to be weighted to provide similar results allowing for local distortions.

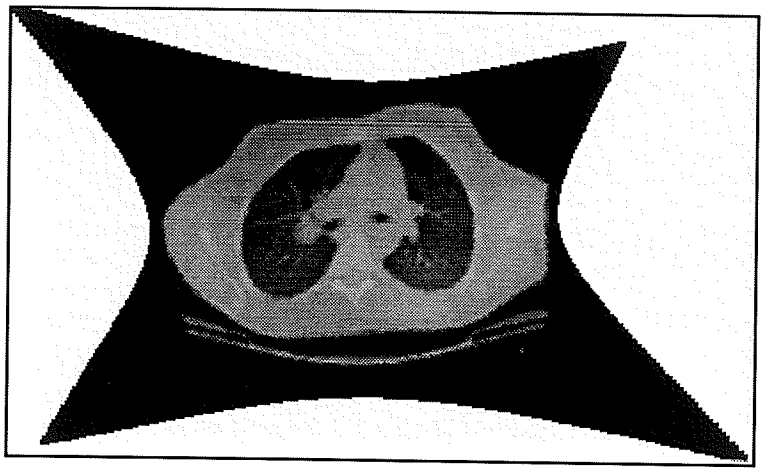

(a)

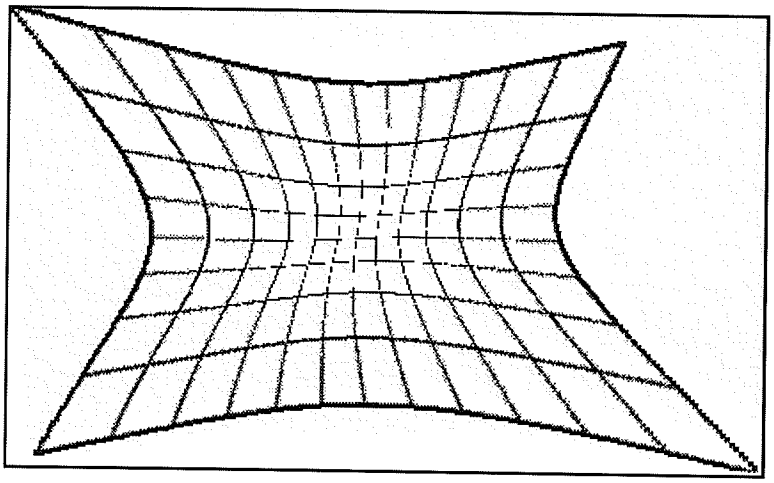

(b)

Figure 5-18. Transformed Image using a Cubic Polynomial Warping Photometric Distortion: (a) Barrel, (b) Distortion Grid

Figure 5-17(a) shows the result of transforming the image in Figure 5-2(a) using a cubic polynomial transformation. Figure 5-17(b) shows the corresponding distortion grid. Figures 5-18(a) and (b) show the result of transforming the image in Figure 5-2(b) and its corresponding distortion grid respectively.

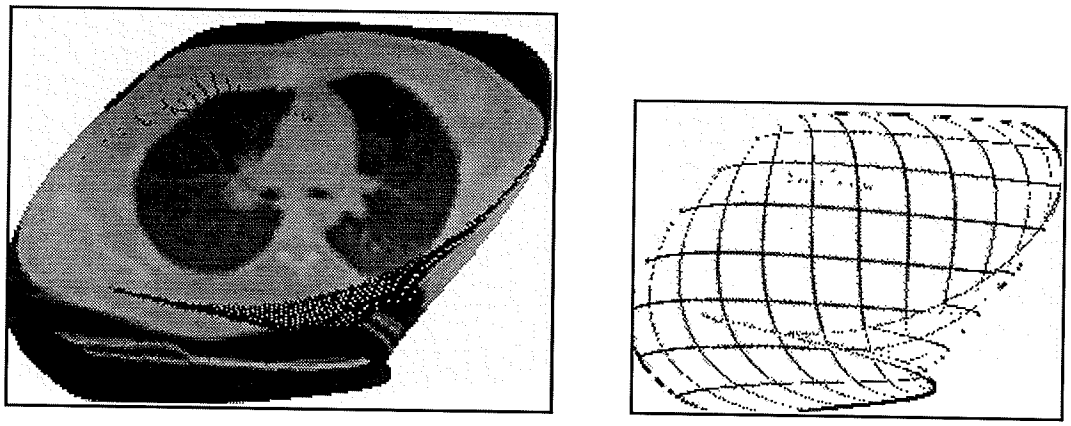

(a) (b)

Figure 5-19. Transformed Image using a Cubic Polynomial Warping Photometric Distortion: (a) Pincushion, (b) Distortion Grid

Note that although the lungs in Figure 5-19(a) seem to have been registered correctly, the portion of the image containing the top-left and bottom-right body contours has been incorrecly transformed, due to the global nature of the polynomial transformation. This is a good example of an incorrect registration.

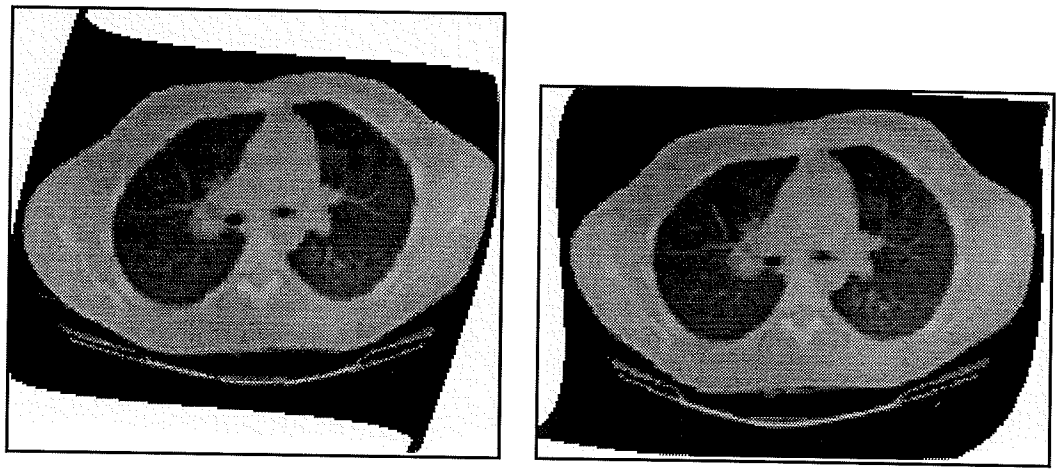

(a) (b)

Figure 5-20. Transformed Image using a Cubic Polynomial Warping Radial Distortion: (a) Horizontal (b) Vertical

Figure 5-20(a) and (b) show the result of transforming the images in Figure 5-2(c) and (d) respectively, using the cubic polynomial. The MSRE's for each of the control-

points in the transformed images in Figures 5-16 to 5-20 with respect to the control-points in the reference image are shown in Table 5-3.

Distorted Image	*Transformation Method*	*MSRE before the Transformation*	*MSRE after the Transformation*
Photometric Distortion Barrel (Figure 5-2(a))	Cubic Polynomial (Figure 5-18)	8.24	2.36
	Surface-Spline (Figure 5-16(a))	8.24	0.19
Photometric Distortion Pincushion (Figure 5-2(b))	Cubic Polynomial (Figure 5-19)	10.15	2.74
	Surface-Spline (Figure 5-16(b))	10.15	0.55
Radial Distortion Horizontal (Figure 5-2(c))	Cubic Polynomial (Figure 5-20(a))	7.89	2.24
	Surface-Spline (Figure 5-17(a))	7.89	0.0
Radial Distortion Vertical (Figure 5-2(d))	Cubic Polynomial (Figure 5-20(b))	7.75	1.84
	Surface-Spline (Figure 5-17(b))	7.75	0.0

Table 5-3. MSRE Estimates for the Geometrically Distorted Images

5.9.3 Multimodal Images

5.9.3.1 MR ⇒ CT Transformation

As a final example, consider the magnetic resonance image of Figure 5-3(b). Due to the unknown nature of the distortion in the MR image, it has been transformed using both polynomial warping and surface-spline transformations. Figure 5-21 shows the transformation of Figure 5-3(b) using a global quadratic polynomial transformation.

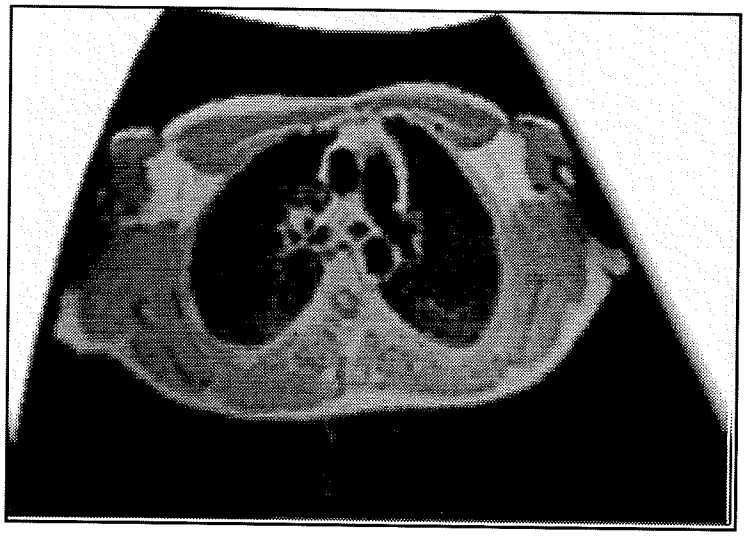

Figure 5-21. Quadratic Polynomial Transformation of Figure 5-3(b)

Whilst the resampled image in Figure 5-19 seems to provide an adequate result, it is nonetheless a global transformation and the resampled image is thereby better modeled using a local transformation method, such as the surface-spline transformation. The resulting image is shown in Figure 5-22(a). The corresponding distortion grid is shown in Figure 5-22(b).

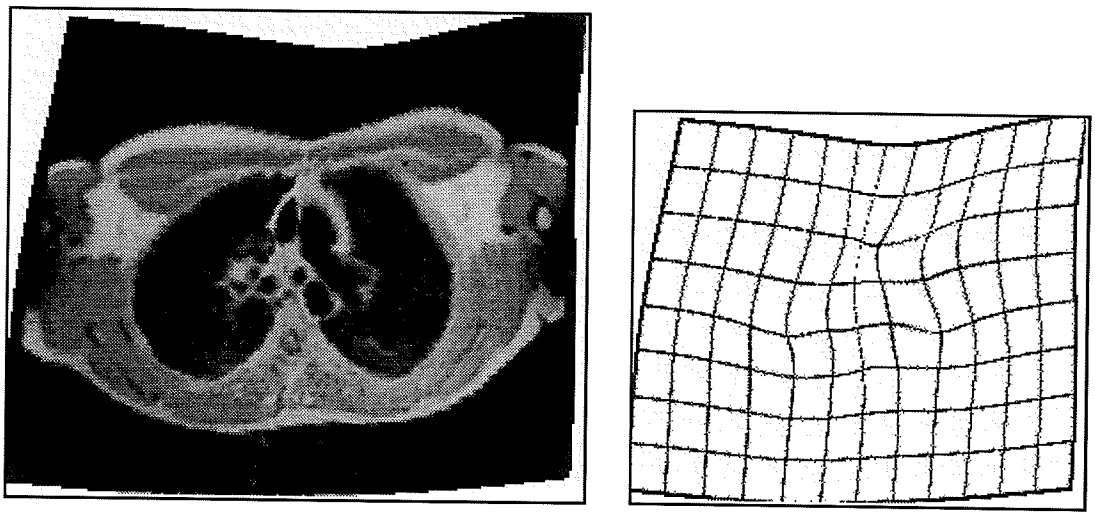

(a) (b)

Figure 5-22. Surface-Spline Transformation of the MR Image in Figure 5-3(b)
(a) Resampled MR Image, (b) Distortion Grid

The MSRE's for each of the control-points in the transformed MR images in Figures 5-21 and 5-22 with respect to the control-points in the reference image are shown in Table 5-4. The differences between the MSRE estimates for the quadratic polynomial and the surface-spline are quite substantial, probably due to the fact that the distortion contained in the MR image is of a local geometric nature and thereby the global polynomial seems less suited for transforming the image, and also because the surface-spline is an interpolating transformation and has many parameters, whilst the quadratic polynomial is an approximating transformation and has only six parameters.

Distorted Image	*Transformation Method*	*MSRE before the Transformation*	*MSRE after the Transformation*
MR Image (Figure 5-3(b))	Quadratic Polynomial (Figure 5-21)	13.00	3.64
	Surface-Spline (Figure 5-22(a))	13.00	0.4

Table 5-4. MSRE Estimates for the Magnetic Resonance Image

5.9.3.2 CT/MR Composite Image

Registered images can be compared side-by-side, in sequence, or by forming composite images. Here a composite multimodal image has been produced from the original CT image and the surface-spline transformed MR image. The lung and spinal regions from the CT image (Figure 5-23(b)) have been superimposed on the magnetic resonance image, (Figure 5-23(a)) resulting in the composite image shown in Figure 5-23(c).

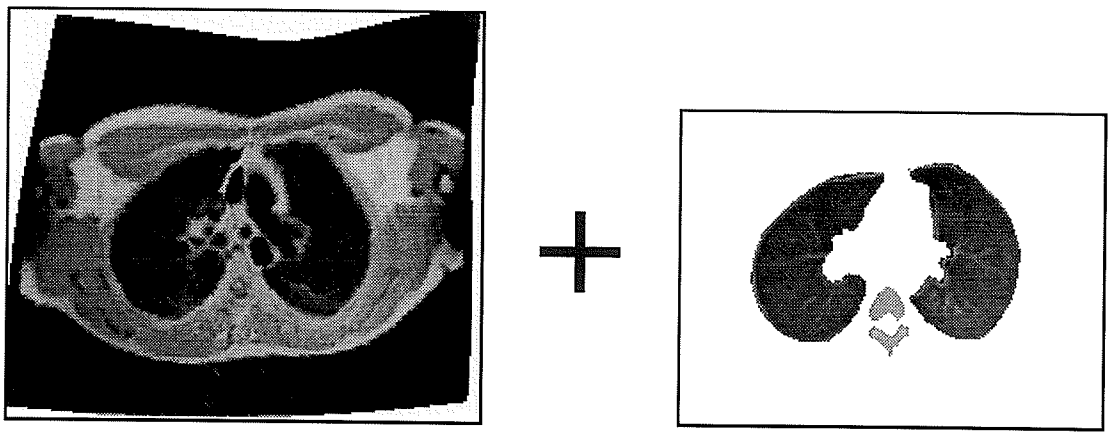

(a) (b)

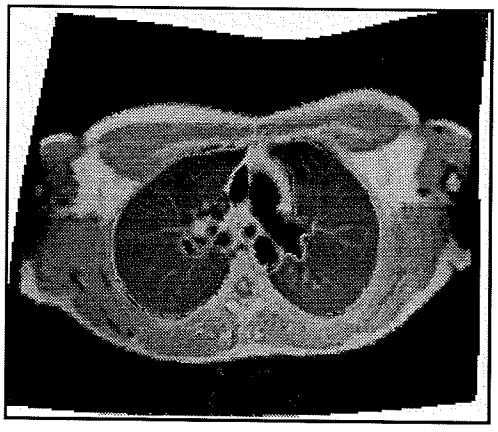

(c)

Figure 5-23. Generation of a Composite Image
(a) MR, (b) CT Lungs and Spinal Region , (c) Composite MR/CT Image

This composite anatomical image provides information on both soft-tissue and bone. It should be noted however, that the x and y resolutions of medical images often vary, as do their slice thicknesses and image size. Since coarser images provide lower definition of features, they may limit the accuracy of registration with finer images. For certain kinds of medical images, particularly where the form of distortion is unknown, such as in multimodal images, it might be appropriate to transform the image by means of an "elastic" transformation. One such form of "elastic" tranformation is to first globally match the images using an affine of low-degree polynomial transformation and then improve this by a local interpolation method.

Chapter 6

3-D Reconstruction and Registration

6.1 Introduction

Although a two-dimensional image is adequate for medical diagnosis, it does not communicate the 3-D nature of the anatomy of a patient. Three-dimensional medical images are reconstructed from a series of two-dimensional images which may be cross-sections of the human body or head produced from modalities such as CT and MR. A fundamental problem in 3-D multimodality medical image comparison is the 3-D registration of volume and surface images.

This chapter discusses some of the concepts associated with 3-D medical image registration. Section 6.2 describes a method of constructing a 3-D volumetric image from tomographic cross-sections using the registration transformations discussed previously. Section 6.3 deals with a brief overview of three-dimensional registration techniques. Section 6.4 deals with the segmentation and subsequent extraction of features via 3-D edge detection. Section 6.5 briefly covers the kinds of control points which could be detected within these features. Finally, methods of 3-D geometric transformation are reviewed in Section 6.6.

6.2 3-D Image Reconstruction

3D image reconstruction can be achieved using image registration techniques. Medical imaging modalities such as computed tomography produce a series of tomographic image "slices" which can be used to reconstruct a 3-D volumetric image. A point on the 2D-grid of an image is called a *pixel.* A *volumetric* image is a three-dimensional image composed of volume elements, or *voxels* [90]. The volumetric image is usually comprised of parallel adjacent cross-sections. The advantage of using volumetric images, over traditional 3-D image reconstruction techniques such as surface rendering is that they provide mechanisms to reveal and explore the inner structure of such 3-D images. In volumetric images, the distance between the consecutive slices is larger than the distance between consecutive pixels within a slice.

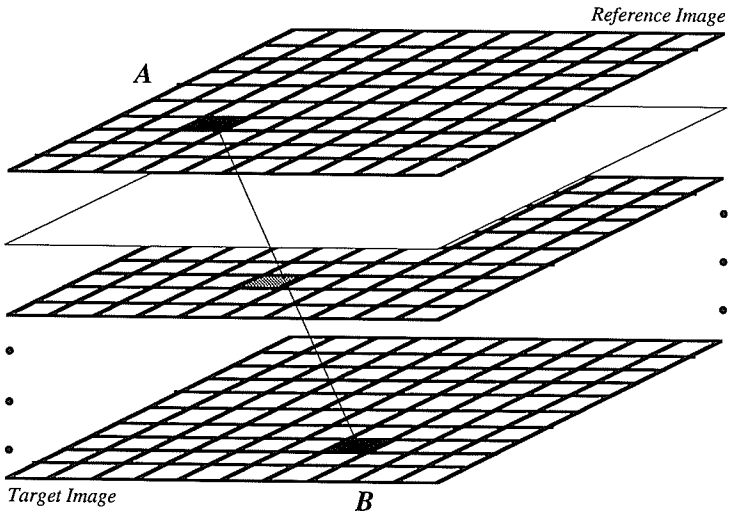

Figure 6-1. Generation of the Intermediate Slices of a Volumetric Image

Consecutive tomographic slices usually have small geometric differences. Two consecutive slices are used to generate intermediate slices to obtain a volumetric data set. The upper slice is called the *reference image* and the lower slice is called the *target image* (See Figure 6-1). The intermediate slices are generated by establishing correspondence between the control points in the reference image and target image and determining the intersections of the lines that connect the corresponding points with the intermediate slices. The control points on the intermediate slice are then used to generate a transformation function that will transform the reference image into the intermediate image. In the illustration shown in Figure 6-1, control point A and control point B correspond to each other, the intersection of line AB with the intermediate slice gives the position of the intermediate control point. If a tissue shrinks or expands from one slice to the next, a point in one slice may connect to several adjacent points in another slice. The intensities of the points are determined by the linear interpolation of intensities of points A and B.

Given that m intermediate slices are to be generated between the reference image $R(x,y)$ and the target image $T(u,v)$, corresponding control points can be found on each of the intermediate slices which are used to transform the reference image. If (u_i,v_i) and (x_i,y_i) $(i=1,\ldots,n)$ represent the control points on the target and reference images respectively then the function F, used to determine the corresponding control points on the intermediate image $I_j(p_i,q_i)$ $(j=1,\ldots,m)$ would be of the form:

$$I_j(p_i,q_i) = F((u_i,v_i),(x_i,y_i)) \tag{6.1}$$

The intermediate image can then be generated by the transformation of the reference image with respect to the control points derived for the intermediate image, using the transformation function T_R given in Equation (6.2).

$$I_j(p,q) = T_R(R(x,y)) \tag{6.2}$$

Tomographic images have the following properties in common:

i) Image slices do not have scaling differences and have very small or no translational and rotational differences;

ii) The correspondence to a point in the reference image lies in a small area centred at the same coordinates in the target image;

iii) There is continuity in the correspondences, that is, neighboring points in the target image map to neighboring points in the reference image. A point in the target image may map to several points in the reference image due to tissue shrinkage, or several points in the target image may map to one point in the reference image due to tissue expansion; however continuity is preserved in the correspondences. An exception occurs when a point discontinues from one slice to the next;

iv) The geometric difference between consecutive slices is local. Therefore a single global transformation function cannot adequately transform the images. The transformation should be in the form of a local-transformation function such as the Surface-Spline Transformation discussed previously in Section 5.6 which is sensitive to local distortions in the image.

As an extension, multi-modality volumetric images could be produced. Such a process would consist of two steps. The first step would involve producing a composite 2-D image from two corresponding images from different modalities. Naturally this step would involve a multi-modality image registration technique to remove distortions before an image from one modality can be superimposed on an image from another modality. The second step would be to produce a 3-D volumetric image from the series of composite tomographic images, produced in step one. For example, corresponding CT and MR images of the chest and abdomen could be registered and combined to provide composite anatomical images from which a 3-D volumetric image could be produced. This 3-D image could then be fused with a 3-D PET or SPECT physiological image [57,83] using a 3-D registration technique such as the one outlined in the following sections. The result is a composite 3-D anatomical/physiological image which can be used to facilitate quantitative analysis of functional images.

6.3 3-D Registration Techniques

Many papers have focused on the registration of multimodality 3-D images [17,19,21,56,122,], which have been used to integrate functional and anatomical information. The majority of methods deal with the registration problem by means of a point-matching geometric transformation. Thirion, *et al.* [108] register 3-D images of the head by means of a rigid transformation: a rotation and a translation between the images. Hill *et al.* [49] propose a method for registering 3-D MR and SPECT images using seven parameters composed of a 3-D rotation in each axis, a 3-D translation in each axis and a uniform scaling and also a method for registering 3-D SPECT images with MR-derived neuro-anatomical atlases using non-uniform scaling instead of uniform scaling. All three methods of geometric transformation used to

register two-dimensional images in Chapter 5 can be extended to produce three-dimensional transformations. As in 2-D point-based registration techniques, there are three steps, control-point selection, via feature extraction, control-point matching and generation of a geometric transformation.

6.4 3-D Edge Detection

Characteristic features in a 3-D image, as in a 2-D image, consist of edges. These edges usually define the boundary of a 3-D feature and provide the basis for selecting the control points described in the next section.

The 2-D gradient operators of Section 3.4.3 can be modified and extended to meet 3-D requirements. The simplest method for generating 3-D masks is to add a third dimension to the 2-D masks. For example, 3×3 masks in 2-D can be replaced by 3×3×1 masks in 3-D. For 2-D edge detectors, two masks are used for the x and y directions respectively. For 3-D edge detectors, three masks for the x, y, and z directions are used. Since most gradient operators are symmetric, their 3-D extensions can be obtained by the symmetric production of three respective masks. The x-mask in the x-y plane, the y-mask in the y-z plane and the z-mask in the z-x plane. For example, the 3-D Sobel operator is shown in Figure 6-2(a), where three 3×3×1 masks for the three respective planes are depicted. This extended 3-D Sobel operator uses 18 neighboring voxels of the central voxel. For the 26-neighbor case, three 3×3×3 masks are used (See Figure 6-2(b)).

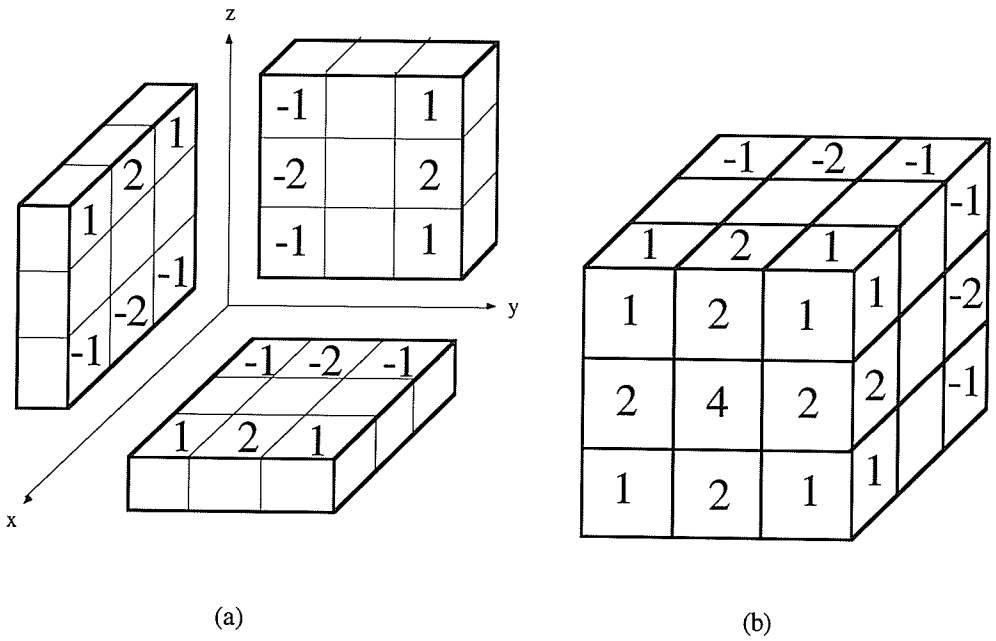

Figure 6-2. 3D Sobel Gradient Masks
(a) 3×3×1 Mask, (b) 3×3×3 (x-mask)

For other gradient operators, the masks can be similarly extended. As with 2-D gradient operators, two responses are obtained, the magnitude and the direction. The magnitude response of the 3-D gradient operator is taken normally as the (Euclidean) norm of its composing mask responses (Equation (6.3)).

$$G_M = \left\{ f_x(x,y)^2 + f_y(y,z)^2 + f_z(z,x)^2 \right\}^{\frac{1}{2}} \tag{6.3}$$

The directions of the 3D gradient operators with respect to the three coordinate axes, namely α, β, and γ, can be obtained using Equations (6.4a), (6.4b) and (6.4c) respectively, where α, β, and γ, are the direction angles of the line perpendicular to the plane from the origin with respect to the x, y and z axes respectively.

$$G_{D\alpha} = \cos^{-1}\left(\frac{f_x(x,y)}{magnitude}\right) \tag{6.4a}$$

$$G_{D\beta} = \cos^{-1}\left(\frac{f_y(y,z)}{magnitude}\right) \tag{6.4b}$$

$$G_{D\gamma} = \cos^{-1}\left(\frac{f_z(z,x)}{magnitude}\right) \tag{6.4c}$$

An overview of 3D gradient edge detectors can be found in Zhang [119].

6.5 3-D Control Point Selection

A point in three-dimensional space is characterized by the coordinates (x,y,z), representing the position of the point. When dealing with three-dimensional images, the control points selected may take the form of significant features such as irregularities on the surfaces.

6.5.1 3-D Surface Primitives

3D points include such surface primitives as peak, pit, saddle, ridge, valley or ravine, flat, hillside, ridge-line and ravine-line (See Figure 6-3) [116]. A *peak* occurs where there is a local maximum in all directions. A *pit* is identical to a peak except that it is a local minimum in all directions rather than a local maximum. A *saddle* point occurs where there is a local maximum in one direction and a local minimum in a perpendicular direction. A *ridge* occurs where there is a local maximum in one direction. A *ridge line* is a curve consisting of a series of ridge points and it may be flat, slope upward, slope downward, curve upward or curve downward. A *ravine* is identical to a ridge except that it is a local minimum in one direction rather than a

local maximum. A *ravine line* is a curve consisting of a series of ravine points. A *flat* is a point where the surrounding surface is a plane. A point is called a *hillside* if and only if it is not covered by the previous categories.

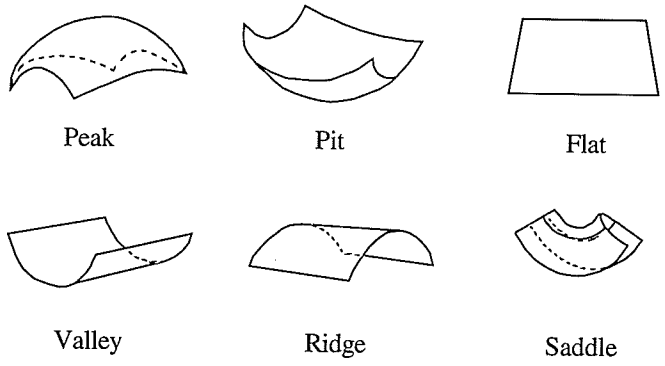

Figure 6-3. Examples of 3-D Surface Primitives

Unlike the two-dimensional case, the selection of control points from such surface primitives is by no means easy. Besl and Jain [10] use the Mean Curvature and the Gaussian Curvature to classify surface primitives. Fan [25] discusses curvature properties related to 3-D images and the detection of surface discontinuities.

6.6 3-D Geometric Transformations

6.6.1 3-D Affine Transformation

Any number of rotations and scalings in any order can be described by an affine transformation. A general transformation in three dimensions has 9 degrees of freedom: 3 translations, 3 rotations and 3 scalings [75]. For example, three rotations, one along each axis, followed by three scalings and then three translations also about each axis, can be described by the transformation function given by:

$$T_{3D} = R(\theta,\beta,\alpha)S(M_x,M_y,M_z)T(t_x,t_y,t_z) \qquad (6.5)$$

The transformation in Equation (6.5) is composed of three scaling factors, M_x, M_y and M_z in the x- y- and z-directions respectively; three translations, t_x, t_y, and t_z in the x-, y-, and z-directions respectively and a rotation matrix which is expressed in terms of the minimum number of rotation parameters, presented here as rotations about the x, y and z axes respectly. The total rotation is given by the product of the three individual rotations (See Figure 6-4) given in Equation (6.6).

$$R(\theta,\beta,\alpha) = R(\alpha)R(\beta)R(\theta) \tag{6.6}$$

$$\begin{bmatrix} \cos\alpha & \sin\alpha & 0 & 0 \\ -\sin\alpha & \cos\alpha & 0 & 0 \\ 0 & 0 & 1 & 0 \\ 0 & 0 & 0 & 1 \end{bmatrix} \quad \begin{bmatrix} \cos\beta & 0 & -\sin\beta & 0 \\ 0 & 1 & 0 & 0 \\ \sin\beta & 0 & \cos\beta & 0 \\ 0 & 0 & 0 & 1 \end{bmatrix} \quad \begin{bmatrix} 1 & 0 & 0 & 0 \\ 0 & \cos\theta & \sin\theta & 0 \\ 0 & -\sin\theta & \cos\theta & 0 \\ 0 & 0 & 0 & 1 \end{bmatrix}$$

(a) (b) (c)

Figure 6-4. 3-D Rotations (a) z-axis (b) y-axis (c) x-axis

$$\begin{bmatrix} 1 & 0 & 0 & 0 \\ 0 & 1 & 0 & 0 \\ 0 & 0 & 1 & 0 \\ t_x & t_y & t_z & 1 \end{bmatrix} \quad \begin{bmatrix} M_x & 0 & 0 & 0 \\ 0 & M_y & 0 & 0 \\ 0 & 0 & M_z & 0 \\ 0 & 0 & 0 & 1 \end{bmatrix} \quad \begin{bmatrix} 1 & h_{yx} & h_{zx} & 0 \\ h_{xy} & 1 & h_{zy} & 0 \\ h_{xz} & h_{yz} & 1 & 0 \\ 0 & 0 & 0 & 1 \end{bmatrix}$$

(a) (b) (c)

Figure 6-5. 3-D (a) Translations (b) Scalings and (c) Shearings

The translation, scaling and shearing transformations are given in Figure 6-5(a) 6-5(b) and 6-5(c) respectively. The resulting 3-D affine transformation (without shear) is

shown in Figure 6-6, with the equations expressing the transformed point (x', y', z') given in Equation 6.7.

$$\begin{bmatrix} M_x\cos\alpha\cos\beta & M_y(\sin\alpha\cos\theta+\cos\alpha\sin\beta\sin\theta) & M_z(\sin\alpha\sin\theta-\cos\alpha\sin\beta\cos\theta) & 0 \\ -M_x\sin\alpha\cos\beta & M_y(\cos\alpha\cos\theta-\sin\alpha\sin\beta\sin\theta) & M_z(\cos\alpha\sin\theta+\sin\alpha\sin\beta\cos\theta) & 0 \\ M_x\sin\beta & -M_y\cos\beta\sin\theta & M_z\cos\beta\cos\theta & 0 \\ t_x & t_y & t_z & 1 \end{bmatrix}$$

Figure 6-6. 3-D Affine Transformation

$$x' = M_x(\cos\alpha\cos\beta-\sin\alpha\cos\beta+\sin\beta)+t_x \quad (6.7a)$$

$$y' = M_y(\sin\alpha\cos\theta+\cos\alpha\cos\theta+\sin\theta(\cos\alpha\sin\beta-\sin\alpha\sin\beta-\cos\beta)+t_y \quad (6.7b)$$

$$z' = M_z(\sin\alpha\sin\theta+\cos\alpha\sin\theta-\cos\theta(\cos\alpha\sin\beta-\sin\alpha\sin\beta-\cos\beta)+t_z \quad (6.7c)$$

The transformation parameters can be estimated using the 3-D least squares fitting technique developed by Arun, Huang and Blostein [5]. This method is based on the use of singular value decomposition (SVD) [35] to minimize the sum of squares of the control points. Abche *et al.* [1,111] estimate the transformation parameters by minimizing the χ^2 (chisquared) function that is defined in terms of the squares of distances of corresponding points in the two images. The distance and chisquared functions are given by Equations (6.8) and (6.9) respectively.

$$d_i^2 = (x_i - x_i')^2 + (y_i - y_i')^2 + (z_i - z_i')^2 \quad (6.8)$$

$$\chi^2 = \frac{1}{n}\sum_{i=1}^{n} d_i^2 / \left(\sigma_{1i}^2 + \sigma_{2i}^2\right) \quad (6.9)$$

Both σ_{1i} and σ_{2i} are the errors associated with the measured values of the control-points and n is the number of control-points. The minimization is accomplished by

non-linear techniques: the Simplex Method, introduced by Nelder and Mead [76] followed by a Variable Metric method [26].

6.6.2 3-D Polynomial Warping

Although an affine transformation may seem sufficient to deal with most kinds of 3D transformations, if geometric distortion exists in the 3-D image, then a general transformation is required. The polynomial transformation discussed previously in Section 5.5 could be extended into three-dimensions. The polynomials would have the form shown in Equation (6.10).

$$x' = \sum_{j=0}^{m}\sum_{k=0}^{j}\sum_{l=0}^{k} a_{jkl} x^l y^{k-l} z^{j-k} \tag{6.10a}$$

$$y' = \sum_{j=0}^{m}\sum_{k=0}^{j}\sum_{l=0}^{k} b_{jkl} x^l y^{k-l} z^{j-k} \tag{6.10b}$$

$$z' = \sum_{j=0}^{m}\sum_{k=0}^{j}\sum_{l=0}^{k} c_{jkl} x^l y^{k-l} z^{j-k} \tag{6.10c}$$

where (x,y,z) are the coordinates of the control point in the reference image and (x',y',z') are the corresponding control points in the transformed image. As an example, consider a polynomial of degree 2, i.e. m=2. Equation (6.10a) when expanded becomes:

$$a_{000} + a_{100}z + a_{110}y + a_{111}x + a_{200}z^2 + a_{210}yz + a_{211}xz + a_{220}y^2 + a_{221}xy + a_{222}x^2 \tag{6.11}$$

The expanded forms of Equations (6.10b) and (6.10c) are similar. The parameters of the mapping function are then determined by minimizing the sum of squares, as in Equation (6.12), using a technique similar to that described for the 3-D affine transformation.

$$E = \sum_{i=1}^{n} \left[\left(u_i - x_i' \right)^2 + \left(v_i - y_i' \right)^2 + \left(w_i - z_i' \right)^2 \right] \tag{6.12}$$

Chapter 7

Conclusion

7.1 Summary

A point-matching technique for registering distorted monomodal and multimodal medical images using geometric transformations has been presented. The technique has three components associated with it, namely, *control-point selection*, *control-point matching* and *geometric transformation*. The main focus of the study was on methods of automatic control-point selection and the generation of an appropriate transformation function. Medical images used to illustrate the concepts presented here are in the form of a computed tomography image of the thorax (chest) and its corresponding magnetic resonance image. The simulated distorted images were synthetically warped using Adobe Photoshop.

For the purpose of illustrating the selection of control points from anatomical features, features were extracted in the forms of contours. The largest contours were extracted from the images, namely the two lung boundaries and the front and back body contours. Control points are selected from both the reference and the distorted images, by means of locating significant points on curves which have been extracted from the

image using segmentation techniques such as edge detection and thresholding. Two types of dominant point detection methods related to curves were discussed: polygonal approximation and angle detection.

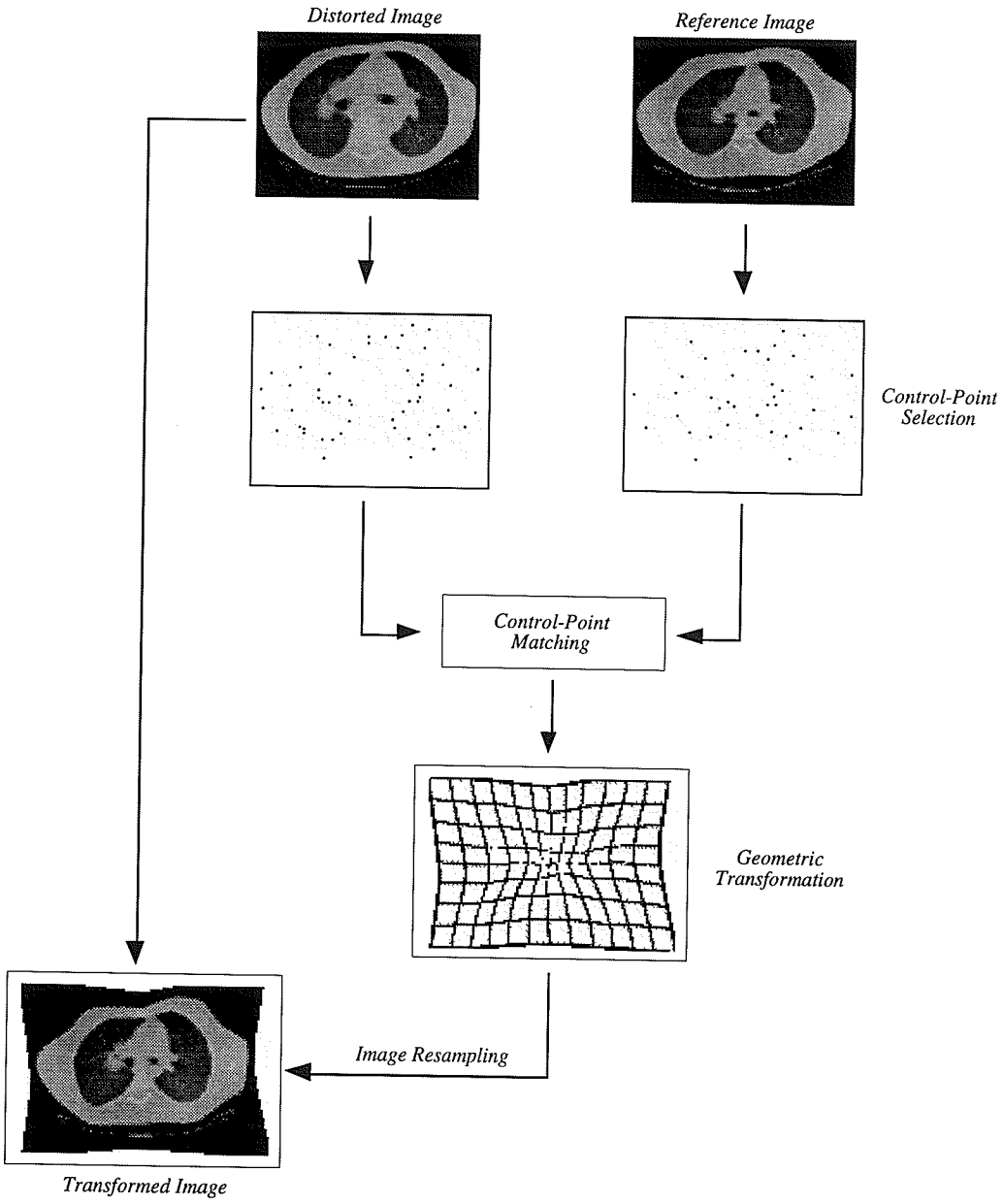

Figure 7-1. Example of Medical Image Registration

The lungs and surrounding regions are the areas of interest, and the front and back body contours were matched only for aesthetic reasons. Typically 30-40 control points were selected from each image using the Farthest Point Bisection Method. The control points from both images were then matched to produce between 15 and 25 control-point pairs depending on the content of the image. The distortion in each CT image is then approximated by determining an appropriate geometric transformation function to model the distortion. The entire process is illustrated in Figure 7-1. The distorted images serve to illustrate both local/global and linear/geometric distortion which appears in medical images. The distorted image is then resampled according to the transformation function. Finally the magnetic resonance image was transformed to illustrate multimodality registration and a composite image was formed using regions from both the resampled MR image and the reference image.

The study then leads on to a discussion of a technique developed for the generation of 3-D volumetric images from tomographic slices, using the principles of geometric transformation.

7.2 Future Work

The concepts discussed throughout this study were related to grayscale medical images. Essentially the only difference between the registration of grayscale images and the registration of color images would occur at the control-point selection step, where color enhancement and segmentation techniques would be substituted for grayscale techniques. The use of color segmentation techniques such as color edge detection would involve extending the gradient edge detection to allow for color images, as in Cumani [20]. This process is not straight-forward, as color images are composed of three separate images representing the red, green and blue components.

The natural extension of this work would involve relating the concepts developed for 2-D registration to three-dimensional medical images, either those created from tomographic images using 3-D reconstruction techniques or those taken directly from 3-D modalities (e.g.. 3-D PET). Some of the concepts related to 3-D image registration were discussed previously in Chapter 6.

Appendix A

Least Squares Calculations

A.1 Least Squares

Given a set of n points from the reference image, denoted $\{(u_i, v_i)$ (for $i = 1,...,n)\}$ and a set of n points, $\{(x_i, y_i)$ (for $i = 1,...,n)\}$ from the distorted image, estimate the corresponding points in the transformed image (x_i', y_i') using the functions $f(x,y)$ and $g(x,y)$ shown in Equation (A.1).

$$\begin{aligned} x_i' &= f(x_i, y_i) \\ y_i' &= g(x_i, y_i) \end{aligned} \tag{A.1}$$

The transformed point (x_i', y_i') differs from the reference point (u_i, v_i) by an error E_i the x and y components of which are calculated using Equation (A.2).

$$E_{xi} = u_i - x_i' \tag{A.2a}$$

$$E_{yi} = v_i - y_i' \tag{A.2b}$$

Define a function which is the sum of squares of the error components:

$$\begin{aligned} E &= \sum_{i=1}^{n} E_{xi}^2 + E_{yi}^2 \\ &= \sum_{i=1}^{n} (u_i - x_i')^2 + (v_i - y_i')^2 \end{aligned} \tag{A.3}$$

A least squares estimate can now be obtained by differentiating the quadratic function E with respect to the parameters of $f(x,y)$ and $g(x,y)$, and setting the result to zero [59]. The resulting set of linear equations can be solved using Gaussian elimination with back-substitution, LU decomposition or singular-value decomposition (SVD) [14].

A.2 Affine Transformation

A.2.1 Rotation, Translation and Uniform Scaling

The equation representing the sum of least squares of an affine transformation with uniform scaling of the form described in Chapter 5 is given by:

$$E = \sum_{i=1}^{n} \left\{ \left[u_i - (ax_i - by_i + h) \right]^2 + \left[v_i - (bx_i + ay_i + k) \right]^2 \right\} \tag{A.4}$$

Evaluating for $\sum_{i=1}^{n} \left[u_i - (ax_i - by_i + h) \right]^2$ gives $\sum_{i=1}^{n} \left[u_i - ax_i + by_i - h \right]^2$ which when expanded gives:

$$\sum_{i=1}^{n} \left(u_i^2 - 2u_i ax_i + 2u_i by_i - 2u_i h + (ax_i)^2 - 2abx_i y_i + 2ax_i h + (by_i)^2 - 2by_i h + h^2 \right) \tag{A.5}$$

Evaluating for $\sum_{i=1}^{n} \left[v_i - (bx_i + ay_i + k) \right]^2$ gives $\sum_{i=1}^{n} \left[v_i - bx_i - ay_i - k \right]^2$ which when expanded gives:

$$\sum_{i=1}^{n} \left(v_i^2 - 2v_i bx_i - 2v_i ay_i - 2v_i k + (bx_i)^2 + 2abx_i y_i + 2bx_i k + (ay_i)^2 + 2ay_i k + k^2 \right) \tag{A.6}$$

Adding Equations (A.5) and (A.6) gives:

$$E=\sum_{i=1}^{n}\left\{\begin{array}{c}u_i^2+v_i^2-2u_iax_i+2u_iby_i-2u_ih-2v_ibx_i-2v_iay_i-2v_ik+(ax_i)^2+(bx_i)^2\\ +2ax_ih+2bx_ik+(by_i)^2+(ay_i)^2-2by_ih+2ay_ik+h^2+k^2\end{array}\right\} \tag{A.7}$$

The partial derivatives of E with respect to the coefficients a, b, h, and k are:

$$\frac{\partial E}{\partial a}=-2\sum_{i=1}^{n}u_ix_i-2\sum_{i=1}^{n}v_iy_i+2a\sum_{i=1}^{n}\left(x_i^2+y_i^2\right)+2h\sum_{i=1}^{n}x_i+2k\sum_{i=1}^{n}y_i \tag{A.8a}$$

$$\frac{\partial E}{\partial b}=2\sum_{i=1}^{n}u_iy_i-2\sum_{i=1}^{n}v_ix_i+2b\sum_{i=1}^{n}\left(x_i^2+y_i^2\right)+2k\sum_{i=1}^{n}x_i-2h\sum_{i=1}^{n}y_i \tag{A.8b}$$

$$\frac{\partial E}{\partial h}=-2\sum_{i=1}^{n}u_i+2a\sum_{i=1}^{n}x_i-2b\sum_{i=1}^{n}y_i+2h\sum_{i=1}^{n}1 \tag{A.8c}$$

$$\frac{\partial E}{\partial k}=-2\sum_{i=1}^{n}v_i+2b\sum_{i=1}^{n}x_i+2a\sum_{i=1}^{n}y_i+2k\sum_{i=1}^{n}1 \tag{A.8d}$$

Setting each of the derivatives in Equation (A.8) to zero gives four linear equations:

$$\begin{aligned}a\sum_{i=1}^{n}\left(x_i^2+y_i^2\right)+h\sum_{i=1}^{n}x_i+k\sum_{i=1}^{n}y_i&=\sum_{i=1}^{n}(u_ix_i+v_iy_i)\\ b\sum_{i=1}^{n}\left(x_i^2+y_i^2\right)-h\sum_{i=1}^{n}y_i+k\sum_{i=1}^{n}x_i&=\sum_{i=1}^{n}(v_ix_i-u_iy_i)\\ a\sum_{i=1}^{n}x_i-b\sum_{i=1}^{n}y_i+h\sum_{i=1}^{n}1&=\sum_{i=1}^{n}u_i\\ a\sum_{i=1}^{n}y_i+b\sum_{i=1}^{n}x_i+k\sum_{i=1}^{n}1&=\sum_{i=1}^{n}v_i\end{aligned} \tag{A.9}$$

Which gives a matrix of the form shown in Figure A-1, where $n=\sum_{i=0}^{n}1$

$$\begin{bmatrix} \sum_{i=1}^{n}(x_i^2+y_i^2) & 0 & \sum_{i=1}^{n}x_i & \sum_{i=1}^{n}y_i \\ 0 & \sum_{i=1}^{n}(x_i^2+y_i^2) & -\sum_{i=1}^{n}y_i & \sum_{i=1}^{n}x_i \\ \sum_{i=1}^{n}x_i & -\sum_{i=1}^{n}y_i & n & 0 \\ \sum_{i=1}^{n}y_i & \sum_{i=1}^{n}x_i & 0 & n \end{bmatrix} \begin{bmatrix} a \\ b \\ h \\ k \end{bmatrix} = \begin{bmatrix} \sum_{i=1}^{n}(u_i x_i + v_i y_i) \\ \sum_{i=1}^{n}(v_i x_i - u_i y_i) \\ \sum_{i=1}^{n}u_i \\ \sum_{i=1}^{n}v_i \end{bmatrix}$$

Figure A-1. Matrix Form of Equation (A.9)

A.2.2 Rotation, Translation and Non-Uniform Scaling

The equation representing the sum of least squares of an affine transformation with non-uniform scaling of the form described in Chapter 5 is given by:

$$E = \sum_{i=1}^{n}\left[u_i - (ax_i - by_i + h)\right]^2 + \left[v_i - (cx_i + dy_i + k)\right]^2 \qquad \text{(A.10)}$$

Evaluating for $\sum_{i=1}^{n}\left[u_i - (ax_i - by_i + h)\right]^2$ gives $\sum_{i=1}^{n}\left[u_i - ax_i + by_i - h\right]^2$ which when expanded gives:

$$\sum_{i=1}^{n}(u_i^2 - 2u_i ax_i + 2u_i by_i - 2u_i h + (ax_i)^2 - 2abx_i y_i + 2ax_i h + (by_i)^2 - 2by_i h + h^2) \qquad \text{(A.11)}$$

Evaluating for $\sum_{i=1}^{n}\left[v_i - (cx_i + dy_i + k)\right]^2$ gives $\sum_{i=1}^{n}\left[v_i - cx_i - dy_i - k\right]^2$ which when expanded gives:

$$\sum_{i=1}^{n}\left(v_i^2 - 2v_i cx_i - 2v_i dy_i - 2v_i k + (cx_i)^2 + 2cdx_i y_i + 2cx_i k + (dy_i)^2 + 2dy_i k + k^2\right) \qquad \text{(A.12)}$$

Adding Equations (A.11) and (A.12) gives:

$$E = \sum_{i=1}^{n}\begin{Bmatrix} u_i^2 - 2u_i ax_i + 2u_i by_i - 2u_i h + (ax_i)^2 - 2abx_i y_i + 2ax_i h + (by_i)^2 - 2by_i h + h^2 \\ +v_i^2 - 2v_i cx_i - 2v_i dy_i - 2v_i k + (cx_i)^2 + 2cdx_i y_i + 2cx_i k + (dy_i)^2 + 2dy_i k + k^2 \end{Bmatrix} \qquad \text{(A.13)}$$

The partial derivatives of E with respect to the coefficients a, b, c, d, h, and k are:

$$\frac{\partial E}{\partial a} = -2\sum_{i=1}^{n} u_i x_i + 2a\sum_{i=1}^{n} x_i^2 - 2b\sum_{i=1}^{n} x_i y_i + 2h\sum_{i=1}^{n} x_i \tag{A.14a}$$

$$\frac{\partial E}{\partial b} = 2\sum_{i=1}^{n} u_i y_i - 2a\sum_{i=1}^{n} x_i y_i + 2b\sum_{i=1}^{n} y_i^2 - 2h\sum_{i=1}^{n} y_i \tag{A.14b}$$

$$\frac{\partial E}{\partial c} = -2\sum_{i=1}^{n} v_i x_i + 2c\sum_{i=1}^{n} x_i^2 + 2d\sum_{i=1}^{n} x_i y_i + 2k\sum_{i=1}^{n} x_i \tag{A.14c}$$

$$\frac{\partial E}{\partial d} = -2\sum_{i=1}^{n} v_i y_i + 2c\sum_{i=1}^{n} x_i y_i + 2d\sum_{i=1}^{n} y_i^2 + 2k\sum_{i=1}^{n} y_i \tag{A.14d}$$

$$\frac{\partial E}{\partial h} = -2\sum_{i=1}^{n} u_i + 2a\sum_{i=1}^{n} x_i - 2b\sum_{i=1}^{n} y_i + 2h\sum_{i=1}^{n} 1 \tag{A.14e}$$

$$\frac{\partial E}{\partial k} = -2\sum_{i=1}^{n} v_i + 2c\sum_{i=1}^{n} x_i + 2d\sum_{i=1}^{n} y_i + 2k\sum_{i=1}^{n} 1 \tag{A.14f}$$

Setting each of the derivatives in Equation (A.14) to zero gives six linear equations:

$$\begin{aligned}
a\sum_{i=1}^{n} x_i^2 - b\sum_{i=1}^{n} x_i y_i + h\sum_{i=1}^{n} x_i &= \sum_{i=1}^{n} u_i x_i \\
-a\sum_{i=1}^{n} x_i y_i + b\sum_{i=1}^{n} y_i^2 - h\sum_{i=1}^{n} y_i &= -\sum_{i=1}^{n} u_i y_i \\
c\sum_{i=1}^{n} x_i^2 + d\sum_{i=1}^{n} x_i y_i + k\sum_{i=1}^{n} x_i &= \sum_{i=1}^{n} v_i x_i \\
c\sum_{i=1}^{n} x_i y_i + d\sum_{i=1}^{n} y_i^2 + k\sum_{i=1}^{n} y_i &= \sum_{i=1}^{n} v_i y_i \\
a\sum_{i=1}^{n} x_i - b\sum_{i=1}^{n} y_i + h\sum_{i=1}^{n} 1 &= \sum_{i=1}^{n} u_i \\
c\sum_{i=1}^{n} x_i + d\sum_{i=1}^{n} y_i + k\sum_{i=1}^{n} 1 &= \sum_{i=1}^{n} v_i
\end{aligned} \tag{A.15}$$

Which gives a matrix of the form shown in Figure A-2, where $n = \sum_{i=0}^{n} 1$

$$\begin{bmatrix} \sum_{i=1}^{n} x_i^2 & -\sum_{i=1}^{n} x_i y_i & 0 & 0 & \sum_{i=1}^{n} x_i & 0 \\ -\sum_{i=1}^{n} x_i y_i & \sum_{i=1}^{n} y_i^2 & 0 & 0 & -\sum_{i=1}^{n} y_i & 0 \\ 0 & 0 & \sum_{i=1}^{n} x_i^2 & \sum_{i=1}^{n} x_i y_i & 0 & \sum_{i=1}^{n} x_i \\ 0 & 0 & \sum_{i=1}^{n} x_i y_i & \sum_{i=1}^{n} y_i^2 & 0 & \sum_{i=1}^{n} y_i \\ \sum_{i=1}^{n} x_i & -\sum_{i=1}^{n} y_i & 0 & 0 & n & 0 \\ 0 & 0 & \sum_{i=1}^{n} x_i & \sum_{i=1}^{n} y_i & 0 & n \end{bmatrix} \begin{bmatrix} a \\ b \\ c \\ d \\ h \\ k \end{bmatrix} = \begin{bmatrix} \sum_{i=1}^{n} x_i u_i \\ -\sum_{i=1}^{n} y_i u_i \\ \sum_{i=1}^{n} x_i v_i \\ \sum_{i=1}^{n} y_i v_i \\ \sum_{i=1}^{n} u_i \\ \sum_{i=1}^{n} v_i \end{bmatrix}$$

Figure A-2. Matrix Form of Equation (A.15)

A.3 Polynomial Transformation

The equation representing the sum of least squares of a quadratic polynomial transformation of the form described in Chapter 5 is given by:

$$E = \sum_{i=1}^{n} \left\{ \begin{array}{l} \left[u_i - \left(a_0 + a_1 x_i + a_2 y_i + a_3 x_i y_i + a_4 x_i^2 + a_5 y_i^2 \right) \right]^2 \\ + \left[v - \left(b_0 + b_1 x_i + b_2 y_i + b_3 x_i y_i + b_4 x_i^2 + b_5 y_i^2 \right) \right]^2 \end{array} \right\} \qquad \text{(A.16)}$$

Evaluating for $\sum_{i=1}^{n} \left[u_i - \left(a_0 + a_1 x_i + a_2 y_i + a_3 x_i y_i + a_4 x_i^2 + a_5 y_i^2 \right) \right]^2$ gives

$\sum_{i=1}^{n} \left[u_i - a_0 - a_1 x_i - a_2 y_i - a_3 x_i y_i - a_4 x_i^2 - a_5 y_i^2 \right]^2$ which when expanded gives:

$$\sum_{i=1}^{n}\begin{Bmatrix} u_i^2 - 2a_0u_i - 2a_1x_iu_i - 2a_2y_iu_i - 2a_3x_iy_iu_i - 2a_4x_i^2u_i - 2a_5y_i^2u_i + a_0^2 + 2a_0a_1x_i \\ +2a_0a_2y_i + 2a_0a_3x_iy_i + 2a_0a_4x_i^2 + 2a_0a_5y_i^2 + (a_1x_i)^2 + 2a_1a_2x_iy_i + 2a_1a_3x_i^2y_i \\ +2a_1a_4x_i^3 + 2a_1a_5x_iy_i^2 + (a_2y_i)^2 + 2a_2a_3x_iy_i^2 + 2a_2a_4x_i^2y_i + 2a_2a_5y_i^3 \\ +(a_3x_iy_i)^2 + 2a_3a_4x_i^3y_i + 2a_3a_5x_iy_i^3 + (a_4x_i^2)^2 + 2a_4a_5x_i^2y_i^2 + (a_5y_i^2)^2 \end{Bmatrix} \quad \text{(A.17)}$$

The partial derivatives of E with respect to the coefficients a_0, a_1, a_2, a_3, a_4 and a_5 are:

$$\frac{\partial E}{\partial a_0} = -2\sum_{i=1}^{n}u_i + 2a_0\sum_{i=1}^{n}1 + 2a_1\sum_{i=1}^{n}x_i + 2a_2\sum_{i=1}^{n}y_i + 2a_3\sum_{i=1}^{n}x_iy_i + 2a_4\sum_{i=1}^{n}x_i^2 + 2a_5\sum_{i=1}^{n}y_i^2 \quad \text{(A.18a)}$$

$$\frac{\partial E}{\partial a_1} = -2\sum_{i=1}^{n}x_iu_i + 2a_0\sum_{i=1}^{n}x_i + 2a_1\sum_{i=1}^{n}x_i^2 + 2a_2\sum_{i=1}^{n}x_iy_i + 2a_3\sum_{i=1}^{n}x_i^2y_i + 2a_4\sum_{i=1}^{n}x_i^3 + 2a_5\sum_{i=1}^{n}x_iy_i^2 \quad \text{(A.18b)}$$

$$\frac{\partial E}{\partial a_2} = -2\sum_{i=1}^{n}y_iu_i + 2a_0\sum_{i=1}^{n}y_i + 2a_1\sum_{i=1}^{n}x_iy_i + 2a_2\sum_{i=1}^{n}y_i^2 + 2a_3\sum_{i=1}^{n}x_iy_i^2 + 2a_4\sum_{i=1}^{n}x_i^2y_i + 2a_5\sum_{i=1}^{n}y_i^3 \quad \text{(A.18c)}$$

$$\frac{\partial E}{\partial a_3} = -2\sum_{i=1}^{n}x_iy_iu_i + 2a_0\sum_{i=1}^{n}x_iy_i + 2a_1\sum_{i=1}^{n}x_i^2y_i + 2a_2\sum_{i=1}^{n}x_iy_i^2 + 2a_3\sum_{i=1}^{n}x_i^2y_i^2 + 2a_4\sum_{i=1}^{n}x_i^3y_i + 2a_5\sum_{i=1}^{n}x_iy_i^3 \quad \text{(A.18d)}$$

$$\frac{\partial E}{\partial a_4} = -2\sum_{i=1}^{n}x_i^2u_i + 2a_0\sum_{i=1}^{n}x_i^2 + 2a_1\sum_{i=1}^{n}x_i^3 + 2a_2\sum_{i=1}^{n}x_i^2y_i + 2a_3\sum_{i=1}^{n}x_i^3y_i + 2a_4\sum_{i=1}^{n}x_i^4 + 2a_5\sum_{i=1}^{n}x_i^2y_i^2 \quad \text{(A.18e)}$$

$$\frac{\partial E}{\partial a_5} = -2\sum_{i=1}^{n}y_i^2u_i + 2a_0\sum_{i=1}^{n}y_i^2 + 2a_1\sum_{i=1}^{n}x_iy_i^2 + 2a_2\sum_{i=1}^{n}y_i^3 + 2a_3\sum_{i=1}^{n}x_iy_i^3 + 2a_4\sum_{i=1}^{n}x_i^2y_i^2 + 2a_5\sum_{i=1}^{n}y_i^4 \quad \text{(A.18f)}$$

Setting each of the derivatives in Equation (A.18) to zero gives six linear equations:

$$
\begin{aligned}
a_0\sum_{i=1}^{n}1 + a_1\sum_{i=1}^{n}x_i + a_2\sum_{i=1}^{n}y_i + a_3\sum_{i=1}^{n}x_iy_i + a_4\sum_{i=1}^{n}x_i^2 + a_5\sum_{i=1}^{n}y_i^2 &= \sum_{i=1}^{n}u_i \\
a_0\sum_{i=1}^{n}x_i + a_1\sum_{i=1}^{n}x_i^2 + a_2\sum_{i=1}^{n}x_iy_i + a_3\sum_{i=1}^{n}x_i^2y_i + a_4\sum_{i=1}^{n}x_i^3 + a_5\sum_{i=1}^{n}x_iy_i^2 &= \sum_{i=1}^{n}x_iu_i \\
a_0\sum_{i=1}^{n}y_i + a_1\sum_{i=1}^{n}x_iy_i + a_2\sum_{i=1}^{n}y_i^2 + a_3\sum_{i=1}^{n}x_iy_i^2 + a_4\sum_{i=1}^{n}x_i^2y_i + a_5\sum_{i=1}^{n}y_i^3 &= \sum_{i=1}^{n}y_iu_i \\
a_0\sum_{i=1}^{n}x_iy_i + a_1\sum_{i=1}^{n}x_i^2y_i + a_2\sum_{i=1}^{n}x_iy_i^2 + a_3\sum_{i=1}^{n}x_i^2y_i^2 + a_4\sum_{i=0}^{n}x_i^3y_i + a_5\sum_{i=1}^{n}x_iy_i^3 &= \sum_{i=1}^{n}x_iy_iu_i \\
a_0\sum_{i=1}^{n}x_i^2 + a_1\sum_{i=1}^{n}x_i^3 + a_2\sum_{i=1}^{n}x_i^2y_i + a_3\sum_{i=1}^{n}x_i^3y_i + a_4\sum_{i=1}^{n}x_i^4 + a_5\sum_{i=1}^{n}x_i^2y_i^2 &= \sum_{i=1}^{n}x_i^2u_i \\
a_0\sum_{i=1}^{n}y_i^2 + a_1\sum_{i=1}^{n}x_iy_i^2 + a_2\sum_{i=1}^{n}y_i^3 + a_3\sum_{i=1}^{n}x_iy_i^3 + a_4\sum_{i=1}^{n}x_i^2y_i^2 + a_5\sum_{i=1}^{n}y_i^4 &= \sum_{i=1}^{n}y_i^2u_i
\end{aligned}
\qquad \text{(A.19)}
$$

Which gives a matrix of the form shown in Figure A-3, where $n = \sum_{i=0}^{n}1$

$$
\begin{bmatrix}
n & \sum x_i & \sum y_i & \sum x_iy_i & \sum x_i^2 & \sum y_i^2 \\
\sum x_i & \sum x_i^2 & \sum x_iy_i & \sum x_i^2y_i & \sum x_i^3 & \sum x_iy_i^2 \\
\sum y_i & \sum x_iy_i & \sum y_i^2 & \sum x_iy_i^2 & \sum x_i^2y_i & \sum y_i^3 \\
\sum x_iy_i & \sum x_i^2y_i & \sum x_iy_i^2 & \sum x_i^2y_i^2 & \sum x_i^3y_i & \sum x_iy_i^3 \\
\sum x_i^2 & \sum x_i^3 & \sum x_i^2y_i & \sum x_i^3y_i & \sum x_i^4 & \sum x_i^2y_i^2 \\
\sum y_i^2 & \sum x_iy_i^2 & \sum y_i^3 & \sum x_iy_i^3 & \sum x_i^2y_i^2 & \sum y_i^4
\end{bmatrix}
\begin{bmatrix} a_0 \\ a_1 \\ a_2 \\ a_3 \\ a_4 \\ a_5 \end{bmatrix}
=
\begin{bmatrix}
\sum u_i \\ \sum x_iu_i \\ \sum y_iu_i \\ \sum x_iy_iu_i \\ \sum x_i^2u_i \\ \sum y_i^2u_i
\end{bmatrix}
$$

Figure A-3. Matrix Form of Equation (A.19)

Appendix B

Mathematical Analysis of Splines

B.1 Thin-Plate Splines

The mathematical analysis presented here has been derived from papers written by Harder and Desmarais [47] and Barrodale *et al.* [8]. A *surface-spline*, or *thin-plate spline* as it is often referred to, is a plate of infinite extent that deforms in bending only. The differential equation relating bending deflections and loads of a plate is given by:

$$D\nabla^4 W = q \tag{B.1}$$

Deflections are specified at n independent points $(x_i, y_i)\ \ i = 1,...,n$. This requires point loads P_i at these n points. The values of these loads must be determined to provide the specified deflections. The first step is to find the deflections due to point load. Introduce polar coordinates $(x = r\cos\theta, y = r\sin\theta)$, and determine the symmetric deflection due to a point load at the origin. Integrating Equation (B.1) gives:

$$W(r) = A + Br^2 + (P/16\pi D)r^2 \ln r^2 \tag{B.2}$$

In Equation (B.2), A and B are undetermined coefficients, and P is the point load. The deflection of the entire spline is taken as the sum of solutions of Equation (B.2), given by Equation (B.3).

$$W(x,y) = \sum_{i=1}^{n}\left(A_i + B_i r_i + (P_i / 16\pi D) r_i^2 \ln r_i^2\right) \tag{B.3a}$$

$$r_i^2 = \left(x - x_i\right)^2 + \left(y - y_i\right)^2 \tag{B.3b}$$

$$a_0 = \sum_{i=1}^{n}\left[A_i + B_i\left(x_i^2 + y_i^2\right)\right] \tag{B.4a}$$

$$a_1 = -2\sum_{i=1}^{n} B_i x_i \tag{B.4b}$$

$$a_2 = -2\sum_{i=1}^{n} B_i y_i \tag{B.4c}$$

$$F_i = P_i / 16\pi D \tag{B.4d}$$

The equation of the surface spline function is derived by substituting the coefficients of Equation (B.4) [47] into Equation (B.3) which gives:

$$W(x,y) = a_0 + a_1 x + a_2 y + \sum_{i=1}^{n} F_i r_i^2 \ln r_i^2 \tag{B.5}$$

The n+3 unknowns are then determined from Equation (B.6) and (B.7).

$$\sum_{i=1}^{n} F_i = \sum_{i=1}^{n} x_i F_i = \sum_{i=1}^{n} y_i F_i = 0 \tag{B.6}$$

$$W(x_j, y_j) = a_0 + a_1 x_j + a_2 y_j + \sum_{i=1}^{n} F_i r_{ij}^2 \ln r_{ij}^2 \quad (j = 1,\ldots,n) \tag{B.7a}$$

$$r_{ij}^2 = \left(x_j - x_i\right)^2 + \left(y_j - y_i\right)^2 \tag{B.7b}$$

The function described by Equation (B.7) can essentially be decomposed into an affine transformation represented by $a_0 + a_1 x_j + a_2 y_j$ and a *principal warp* [12], an affine-free geometric transformations of progressively smaller geometrical scale represented by $\sum_{i=1}^{n} F_i r_{ij}^2 \ln r_{ij}^2$. The coefficients $a_0, a_1, a_2,$ and F_i $(i = 1,\ldots,n)$ are therefore determined by solving the (n+3) system of linear equations expressed in matrix form in Figure B-1.

$$\begin{bmatrix} 0 & 0 & 0 & 1 & 1 & \cdots & 1 \\ 0 & 0 & 0 & x_1 & x_2 & \cdots & x_n \\ 0 & 0 & 0 & y_1 & y_2 & \cdots & y_n \\ 1 & x_1 & y_1 & 0 & r_{21}^2 \ln r_{21}^2 & \cdots & r_{n1}^2 \ln r_{n1}^2 \\ 1 & x_2 & y_2 & r_{12}^2 \ln r_{12}^2 & 0 & \cdots & r_{n2}^2 \ln r_{n2}^2 \\ \cdot & \cdot & \cdot & \cdot & \cdot & & \cdot \\ \cdot & \cdot & \cdot & \cdot & \cdot & & \cdot \\ \cdot & \cdot & \cdot & \cdot & \cdot & & \cdot \\ 1 & x_n & y_n & r_{1n}^2 \ln r_{1n}^2 & r_{2n}^2 \ln r_{2n}^2 & \cdots & 0 \end{bmatrix} \begin{bmatrix} a_0 \\ a_1 \\ a_2 \\ F_1 \\ F_2 \\ \cdot \\ \cdot \\ \cdot \\ F_n \end{bmatrix} = \begin{bmatrix} 0 \\ 0 \\ 0 \\ u_1 \\ u_2 \\ \cdot \\ \cdot \\ \cdot \\ u_n \end{bmatrix}$$

Figure B-1. System of Linear Equations representing the Surface Spline

Given that the surface spline transformation method uses two surface splines to represent the X and Y components of the mapping function, Equation (B.7) exists in two forms $f(x_j, y_j)$ and $g(x_j, y_j)$ $(j = 1,\ldots,n)$ representing the X and Y components respectively for n points, given by:

$$f(x_j, y_j) = a_0 + a_1 x_j + a_2 y_j + \sum_{i=1}^{n} F_i r_{ij}^2 \ln r_{ij}^2 \qquad \text{(B.8)}$$

$$g(x_j, y_j) = b_0 + b_1 x_j + b_2 y_j + \sum_{i=1}^{n} G_i r_{ij}^2 \ln r_{ij}^2 \qquad \text{(B.9)}$$

References

Abbreviations

CGA	Computer Graphics and Applications
CGIP	Computer Graphics and Image Processing
CMIG	Computerized Medical Imaging and Graphics
CVGIP	Computer Vision, Graphics and Image Processing
EMB	Engineering in Medicine and Biology
EMBS	Engineering in Medicine and Biology Society
GE	Transactions on Geoscience Electronics
GMIP	Graphical Models and Image Processing
GRS	Transactions on Geoscience and Remote Sensing
JCAT	Journal of Computer Assisted Tomography
MI	Transactions on Medical Imaging
PAMI	Transactions on Pattern Analysis and Machine Intelligence
SMC	Transactions on Systems, Man, and Cybernetics
TC	Transactions on Computers

[1] Abche, A.B., Tzanakos, G.S., and Micheli-Tzanakou, E.
A Method of Multimodal 3-D Image Registration with External Markers
IEEE EMBS, Vol. 14, No. 5, 1992, pp. 1881-1882

[2] Alpert, N.M., Bradshaw, J.F., Kennedy, D., and Correia, J.A.
The Principal Axes Transformation - A Method for Image Registration
The Journal of Nuclear Medicine, Vol. 31, No. 10, Oct 1990, pp. 1717-1722

[3] Ansari, N., and Delp, E.J.
On Detecting Dominant Points
Pattern Recognition, Vol. 24, No. 5, 1991, pp. 441-451

[4] Ansari, N., and Huang, K.
Non-Parametric Dominant Point Detection
Pattern Recognition, Vol. 24, No. 9, Sep 1991, pp. 849-862

[5] Arun, K.S., Huang, T.S., and Blostein, S.D.
Least Squares Fitting of Two 3D Point Sets
IEEE PAMI, Vol. 9, 1987, pp. 698-700

[6] Asada, H., and Brady, M.
The Curvature Primal Sketch
IEEE PAMI, Vol. 8, No. 1, January 1986, pp.2-14

[7] Bajcsy, R., and Broit, C.
Matching of Deformed Images
IEEE Proc. Sixth Intl. Conf. on Pattern Recognition, Oct. 1982, pp. 351-353

[8] Barrodale, I., Skea, D., Berkley, M., Kuwahara, R., and Poeckert, R.
Warping Digital Images Using Thin Plate Splines
Pattern Recognition, Vol. 26, No. 2, Feb 1993, pp. 375-376

[9] Bartoo, G.T., and Hanson, W.A.
Multi-Modality Image Registration Using Centroid Mapping
IEEE EMBS, Vol. 11, 1989 pp. 550-551

[10] Besl, P.J., and Jain, R.C.
Invariant Surface Characteristics for 3-D Object Recognition in Range Images
CVGIP, Vol. 33, No. 1, Jan. 1986, pp. 33-80

[11] Beus, H.L., and Tiu, S.S.
An Improved Corner Detection Algorithm Based on Chain-Coded Plane Curves
Pattern Recognition, Vol. 20, No. 3, 1987, pp. 291-296

[12] Bookstein, F.L.
Principal Warps: Thin-Plate Splines and the Decomposition of Deformations
IEEE PAMI, Vol. 11, No. 6, June 1989, pp. 567-585

[13] Brown, L.G.
A Survey of Image Registration Techniques
Department of Computer Science, Columbia University, January 1992. pp. 1-60

[14] Burden, R.L. and Faires, J.D. (1985)
Numerical Analysis (Third ed.)
Prindle, Weber & Schmidt, Boston.

[15] Burr, D.J.
A Dynamic Model for Image Registration
CGIP, Vol. 15, 1981, pp. 102-112

[16] Chang, L.W., Chen, H.W., and Ho, J.R.
Reconstruction of 3D Medical Images: A Nonlinear Interpolation Technique for Reconstruction of 3D Medical Images
CVGIP: GMIP, Vol. 53, No. 4, July 1991, pp. 382-391

[17] Chen, Q., Defrise, M., Deconinck, F., and Jonckheer, M.H.
3D Multimodality Imaging: The Registration Problem
IEEE EMBS, Vol. 14, No. 5, 1992, pp. 2168-2169

[18] Cideciyan, A.V., and Nagel, J.H.
Multi-modality Image Registration Using the Hough Transform
IEEE EMBS, Vol. 12, 1990 pp. 141-142

[19] Collignon, A., Vandermeulen, D., Suetens, P., and Marchal, G.
Registration of 3D Multimodality Medical Images Using Surfaces and Point Landmarks
Pattern Recognition Letters, Vol. 15, No. 5, May 1994, pp. 461-467

[20] Cumani, A.
Edge Detection in Multispectral Images
CVGIP, Vol. 53, No. 1, Jan 1991, pp. 40-51

[21] Dann, R., Hoford, J., Kovacic, S., Reivich, M., and Bajcsy, R.
Evaluation of Elastic Matching System for Anatomic (CT,MR) and Functional (PET) Cerebral Images
JCAT, Vol. 13, No. 4, Jul/Aug 1989, pp. 603-611

[22] DaPonte, J.S. and Fox, M.D.
Enhancement of Chest Radiographs with Gradient Operators
IEEE MI, Vol. 7, No. 2, June 1988, pp. 109-117

[23] Davis, L.S., Rosenfeld, A., and Weszka, J.S.
Region Extraction by Averaging and Thresholding
IEEE SMC, Vol. 5, 1975, pp. 383-388

[24] Faber, T.L., and Stokely, E.M.
Orientation of 3-D Structures in Medical Images
IEEE PAMI, Vol. 10, No. 5, Sep 1988, pp. 626-633

[25] Fan, T.J. (1990)
Decribing and Recognizing 3-D Objects Using Surface Properties
Springer-Verlag, New York

[26] Fletcher, R.
A New Approach to Variable Metric Algorithms
Computer Journal, Vol. 13, 1970, pp. 317-322

[27] Flusser, J.
An Adaptive Method for Image Registration
Pattern Recognition, Vol. 25, 1992, pp. 45-54

[28] Flusser, J., and Suk, T.
Pattern Recognition by Affine Moment Invariants
Pattern Recognition, Vol. 26, No. 1, Jan 1993, pp. 167-174

[29] Freeman, H.
Shape Description via the Use of Critical Points
Pattern Recognition, Vol. 10, 1978, pp. 159-166

[30] Freeman, H., and Davis, L.S.
A Corner Finding Algorithm for Chain-Coded Curves
IEEE TC, Vol. 26, 1977, pp. 297-303

[31] Fright, W.R. and Linney, A.D.
Registration of 3-D Head Surfaces Using Multiple Landmarks
IEEE MI, Vol. 12, No. 3, September 1993, pp. 515-520

[32] Fu, K.S. and Mui, J.K.
A Survey on Image Segmentation
Pattern Recognition, Vol. 13, No. 1, 1981, pp. 3-16

[33] Gee, J.C., Reivich, M., and Bajcsy, R.
Elastically Deforming 3D Atlas to Match Anatomical Brain Images
JCAT, Vol. 17, No. 2, Mar/Apr 1992, pp. 225-236

[34] Gerlot-Chiron, P., and Bizais, Y.
Registration of Multimodality Medical Images Using a Region Overlap Criterion
CVGIP: GMIP, Vol. 54, No. 5, September 1992, pp. 396-406

[35] Golub, G.H., and Van Loan, C.F. (1983)
Matrix Computations
John Hopkins University Press, Baltimore

[36] Gonzalez, R.C. and Woods, R.E. (1992)
Digital Image Processing
Addison-Wesley Publishing Company, Reading Massachusetts

[37] Goshtasby, A.
Image Registration by Local Approximation Methods
Image Vision Computing, No.4, November 1988, pp.255-261

[38] Goshtasby, A.
Registration of Images with Geometric Distortions
IEEE GRS, Vol. 6, No. 1, Jan 1988, pp. 60-64

[39] Goshtasby, A.
Piecewise Linear Mapping Functions for Image Registration
Pattern Recognition, Vol. 19, No. 6, 1986, pp. 459-466

[40] Goshtasby, A.
Piecewise Cubic Mapping Functions for Image Registration
Pattern Recognition, Vol. 20, No. 5, 1987, pp. 525-533

[41] Goshtasby, A.
Template Matching in Rotated Images
IEEE PAMI, Vol. 7, No. 3, May 1985, pp.338-344

[42] Goshtasby, A., and Stockman, G.C.
Point Pattern Matching Using Convex Hull Edges
IEEE SMC, Vol. SMC-15, No.5 Sep/Oct 1985, pp. 631-637

[43] Goshtasby, A., Stockman, G.C., and Page, C.V.
A Region -Based Approach to Digital Image Registration with Subpixel Accuracy
IEEE GRS, Vol. GE-24, No. 3, May 1986, pp. 390-399

[44] Goshtasby, A., Turner, D.A., and Ackerman, L.V.
Matching Tomographic Slices for Interpolation
IEEE MI, Vol. 11, No. 4, Dec 1992, pp. 507-516

[45] Haralick, R.M. and Shapiro, L.G.
SURVEY: Image Segmentation Techniques
CVGIP, Vol. 29, 1985, pp. 100-132

[46] Haralick, R.M., and Shapiro, L.G.
Glossary of Computer Vision Terms
Pattern Recognition, Vol. 24, No. 1, Jan 1991, pp. 66-93

[47] Harder, R.L. and Desmarais, R.N.
Interpolation Using Spline Surfaces
Journal of Aircraft, Vol. 9, No. 2, February 1972, pp. 189-191

[48] Herbin, M., Venot, A., Devaux, J.Y., Walter, E. Lebruchec, J.F., Dubertret, L., and Roucayrol, J.C.
Automated Registration of Dissimilar Images: Application to Medical Imagery
CVGIP, Vol. 47, 1989, pp. 77-88

[49] Hill, D.L.G., Hawkes, D.J., Lehmenn, E.D., Crossman, J.E., Robinson, L., Bird, C.F. and Maisey, M.N.
Registered High Resolution Images in the Interpretation of Radionuclide Scans
IEEE EMBS, Vol. 12, No. 1, 1990 pp. 143-144

[50] Hill, D.L.G., Hawkes, D.J., Crossman, J.E., Gleeson, M.J., Cox, T.C.S., Bracey, E.E., Strong, A.J., and Graves, P.
Registration of MR and CT Images for Skull Base Surgery Using Point-Like Anatomical Features
The British Journal of Radiology, Vol. 64, November 1991, pp. 1030-1035

[51] Jähne, B. (1991)
Digital Image Processing: Concepts, Algorithms and Scientific Applications
Springer-Verlag, New York

[52] Jain, A.K. (1989)
Fundamentals of Digital Image Processing
Prentice Hall, Englewood Cliffs, New Jersey

[53] Junck, L., Moen, J.G., Hutchins, G.D. Brown, M.B. and Kuhl, D.E.
Correlation Methods for the Centering, Rotation and Alignment of Functional Brain Images
The Journal of Nuclear Medicine, Vol. 31, No. 7, July 1990, pp. 1220-1226

[54] Kanal, L.N., Lambird, B.A., Levine, D. and Stockman, G.C.
Digital Registration of Images from Similar and Dissimilar Sensors
Proc. Int. Conf. Cybern. Society, 1981, pp. 347-351

[55] Kitchen, L., and Rosenfeld, A.
Grey Level Corner Detection
Pattern Recognition Letters, Vol. 1, 1982, pp. 95-102

[56] Kovacic, S., Gee, J.C., Ching, W.S.L., Reivich, M., and Bajcsy, R.
Three-Dimensional Registration of PET and CT Images
IEEE EMBS, Vol. 11, 1989, pp. 548-549

[57] Kramer, E., Noz, M., Maguire Jr, G., Sanger, J. Walsh, C., and Millan, E.
Fusing of Immunoscintigraphy SPECT with CT or MRI for Improved Multimodality Image Interpretation
IEEE EMBS, Vol. 14, No. 5, 1992, pp. 1805-1806

[58] Lam, L., Lee, S.W., and Suen, C.Y.
Thinning Methodologies - A Comprehensive Survey
IEEE PAMI, Vol. 14, No. 9, Sept 1992, pp. 869-885

[59] Lancaster, P., and Salkauskas, K. (1986)
Curve and Surface Fitting: An Introduction
Academic Press, New York

[60] Levin, D.N., Pelizzari, C.A., Chen, G.T.Y., Chen, C.T., and Cooper, M.D.
Retrospective Geometric Correlation of MR, CT and PET Images
Radiology, Vol. 169, No. 3, 1988, pp. 817-823

[61] Liang, Z.
Tissue Classification and Segmentation of MR Images
IEEE EMB, Vol. 12, No. 1, March 1993, pp. 81-85

[62] Lin, K.P., and Huang, S.C.
An Elastic Mapping Algorithm for Tomographic Images
IEEE EMBS, Vol. 15, No. 1, 1993, pp. 40-41

[63] Liu, H.C., and Srinath, M.D.
Corner Detection from Chain-Code
Pattern Recognition, Vol. 23, No. 1/2, 1990, pp. 51-68

[64] Malison, R.T., Miller, E.G., Greene, R., McCarthy, G., Charney, D.S. and Innis, R.B.
Computer-Assisted Coregistration of Multislice SPECT and MR Images by Fixed External Fiducials
JCAT, Vol. 17, No. 6, Nov/Dec 1993, pp. 952-960

[65] Maurer Jr, C.R., Fitzpatrick, J.M., Wang, M.Y., and Maciunas, R.J.
Correction of Geometrical Distortion in MR Image Registration
IEEE EMBS,, Vol. 15, No. 1, 1993, pp. 122-123

[66] McLain, D.H.
Interpolation Methods for Erroneous Data
in Brodlie, K.W. (ed.) (1980)
in Mathematical Methods in Computer Graphics Design, pp. 87-104

[67] Maguire Jr., G.Q., Noz, M.E., Rusinek, H., Jaeger, J., Kramer, E.L., Sanger, J.J. & Smith, G.
Graphics Applied to Medical Image Registration
IEEE CGA, Vol. 11, March 1991, pp. 20-27

[68] Meek, D.S., and Walton, D.J.
Several Methods for Representing Discrete Data by Line Segments
Cartographica, Vol. 28, No. 2, Summer 1991, pp. 13-20

[69] Mehrotra, R., and Nichani, S.
Corner Detection
Pattern Recognition, Vol. 23, No. 11, Nov 1990, pp. 1223-1233

[70] Merickel, M.
3D Reconstruction: The Registration Problem
CVGIP, Vol. 42, 1988, pp. 206-219

[71] Mitiche, A. and Aggarwal, J.K.
Contour Registration by Shape-Specific Points for Shape Matching
CVGIP, Vol. 22, 1983, pp.396-408

[72] Moshfeghi, M.
Multimodality Image Registration Techniques in Medicine
IEEE EMBS, Vol. 11, 1989, pp. 2007-2008

[73] Moshfeghi, M.
Elastic Matching of Multimodality Medical Images
CVGIP: CGIP, Vol. 53, No. 3, May 1991, pp. 271-282

[74] Nack, M.L.
Rectification and Registration of Digital Images and the Effect of Cloud Detection
Proc. Machine Processing of Remotely Sensed Data, 1977, pp. 12-23

[75] Neelin,. P., Crossman, J., Hawkes, D.J., Ma, Y., and Evans, A.C.
Validation of an MRI/PET Landmark Registration Method Using 3D Simulated PET Images and Point Simulations
CMIG, Vol. 17, Nos. 4/5, 1993, pp. 351-356

[76] Nelder, J.A., and Mead, R.
A Simplex MEthod for Function Minimization
Computer Journal, Vol. 7, 1965, pp. 308-313

[77] Nichani, S.J. and Ranganathan, N.
Corner Detection
Pattern Recognition, Vol. 23, No. 11, 1990, pp. 1223-1233

[78] Pavlidis, T.
A Thinning Algorithm for Discrete Binary Images
CGIP, Vol. 13, 1980, pp. 142-157

[79] Pavlidis, T. (1982)
Algorithms for Graphics and Image Processing
Computer Science Press, Rockville MD

[80] Peli, E., Augliere, A. and Timberlake, G.T.
Feature-Based Registration of Retinal Images
IEEE MI, Vol. 6, No. 3, Sept. 1987, pp. 272-278

[81] Pelizzari, C.A., Chen, G.T.Y., Spelbring, D.R., Weichselbaum, R.R. and Chen, C.T.
Accurate Three-Dimensional Registration of CT, PET, and/or MR Images of the Brain
JCAT, Vol. 13, No. 1, 1989, pp. 20-26

[82] Perednia, D.A., and White, R.G.
Automatic Registration of Multiple Skin Lesions by Use of Point-Pattern Matching
CMIG, Vol. 16, Nos. 3, 1992, pp. 205-216

[83] Pohjonen, H., Kiuru, A., Nikkinen, P., and Karp, P.
Registration of Anatomical and Functional 3D-Data Sets
IEEE EMBS, Vol. 14, No. 5, 1992, pp. 2239-2240

[84] Pratt, W.K. (1991)
Digital Image Processing (2nd ed.)
John Wiley & Sons, Inc., New York

[85] Ranade, S. and Rosenfeld,A.
Point Pattern Matching by Relaxation
Pattern Recognition Vol. 12, 1980, pp.269-275

[86] Ray, B.K., and Ray, K.S.
An Algorithm for Detection of Dominant Points and Polygonal Approximation of Digitized Curves
Pattern Recognition Letters, Vol. 13, No. 12, Dec 1992, pp. 849-856

[87] Ray, B.K., and Ray, K.S.
Detection of Significant Points and Polygonal Approximation of Digitized Curves
Pattern Recognition Letters, Vol. 13, No. 6, June 1992, pp. 443-452

[88] Rizzo, G., Gilardi, M.C., Bettinardi, V., Cerutti, S. and Fazio, F.
Integration of Multimodal Medical Images
IEEE EMBS, Vol. 12, No. 1, 1990 pp. 145-146

[89] Rizzo, G., Prinster, A., Gilardi, M.C., Cerutti, S., Bettinardi, V., Biondi, E., and Fazio, F.
Matching of Multimodal Medical Images to a Reference Atlas: Use of an Elastic Transformation Method
IEEE EMBS Vol. 14, No. 5, 1992, pp. 1803-1804

[90] Robb, R.A. (ed.) (1985)
Three-Dimensional Biomedical Imaging Volume I
CRC Press, Inc., Boca Raton, Florida

[91] Robb, R.A. (ed.) (1985)
Three-Dimensional Biomedical Imaging Volume II
CRC Press, Inc., Boca Raton, Florida

[92] Rogers, D.F. and Adams, J.A. (1990)
Mathematical Elements for Computer Graphics (Second Ed.)
McGraw-Hill Publishing Company, New York

[93] Rosenfeld, A.
Image Analysis: Problems, Progress and Prospects
Pattern Recognition, Vol. 17, No. 1, 1984, pp. 3-12

[94] Rosenfeld, A., and Johnston, E.
Angle Detection on Digital Curves
IEEE TC, Vol. 22, No. 9, 1973, pp. 875-878

[95] Rosenfeld, A., and Weszka, J.S.
An Improved Method of Angle Detection on Digital Curves
IEEE TC, Vol. 24, No. 9, 1975, pp. 940-941

[96] Sahoo, P.K., Soltani, S., Wong, A.K.C., and Chen, Y.C.
A Survey of Thresholding Techniques
CVGIP, Vol. 41, 1988, pp. 233-260

[97] Sedgewick, R. (1988)
Algorithms (2nd ed.)
Addison-Wesley Publishing Company, Reading Massachusetts

[98] Shu, J.S.P.
One-Pixel-Wide Edge Detection
Pattern Recognition, Vol. 22, No. 6, June 1989, pp. 665-673

[99] Shukla, S.S., Honeyman, J.C., Crosson, B., Williams, C.M. and Nadeau, S.E.
Method for Registering Brain SPECT and MR Images
JCAT, Vol. 16, No. 6, Nov/Dec 1992, pp. 966-970

[100] Singh, A. and Schneier, M.
Gray Level Corner Detection: A Generalization and a Robust Real Time Implementation
CVGIP, Vol. 51, 1990, pp. 54-69

[101] Steiner, D. and Kirby, M.E.
Geometrical Referencing of Landsat Images by Affine Transformation and Overlaying of Map Data
Photogrammetria, Vol. 33, 1977, pp. 41-75

[102] Stockman, G.C., Kopstein, S. and Benett, S.
Matching Images to Models for Registration and Object Detection via Clustering
IEEE PAMI, Vol. 4, No. 3, May 1982, pp.229-241

[103] Sumanaweera, T.S., Glover, G.H., Binford, T.O., and Adler, J.R.
MR Susceptibility Misregistration Correction
IEEE MI, Vol. 12, No. 2, June 1993, pp. 251-259

[104] Tang, Y.Y., and Suen, C.Y.
New Algorithms for Fixed and Elastic Transformation Models
IEEE IP, Vol. 3, No. 4, July 1994, pp. 355-365

[105] Teh, C.H., and Chin, R.T.
On Digital Approximation of Moment Invariants
CVGIP, Vol. 33, 1986, pp. 318-326

[106] Teh, C.H., and Chin, R.T.
On the Detection of Dominant Points on Digital Curves
IEEE PAMI, Vol. 11, No. 8, Aug 1989, pp. 859-872

[107] Thapa, K.
Critical Points Detection and Automatic Line Generalization in Raster Data Using Zero Crossings
The Cartographic Journal, Vol. 25, No. 1, June 1988, pp. 58-68

[108] Thirion, J.P., Gourdon, A., Monga, O., Gueziec, A., and Ayache, N.
Fully Automatic Registration of 3D CAT-Scan Images Using Crest Lines
IEEE EMBS,, Vol. 14, No. 5, 1992, pp. 1888-1890

[109] Toennies, K.D., Udupa, J.K., Herman, G.T., Wornom III, I.L. and Buchman, S.R.
Registration of 3D Objects and Surfaces
IEEE CGA, May 1990, pp. 52-62

[110] Ton, J. and Jain, A.K.
Registering Landsat Images by Point Matching
IEEE GRS, Vol. 27, No. 5, September 1989, pp. 642-651

[111] Tzanakos, G.S., Abche, A.B., and Micheli-Tzanakou, E.
Implementation of a Method for Multimodal 3-D Image Registration with External Markers
IEEE EMBS, Vol. 15, No. 1, 1993, pp. 12-13

[112] Van den Elsen, P.A., Pol, E-J.D., and Viergever, M.A.
Medical Image Matching - A Review with Classification
IEEE EMB, Vol. 12, No. 1,March 1993, pp. 26-39

[113] Vannier, M.W., Hildebolt, C.F., Gayou, D.E., and Marsh, J.L.
Introduction to 3D Imaging in
Udupa, J.K. and Herman, G.T. (eds.) (1991)
3D Imaging in Medicine, CRC Press, Ann Arbor.

[114] Van Wie, P., and Stein, M.
A Landsat Digital Image Rectification System
IEEE GE, Vol. 15, No. 3, July 1977, pp. 130-137

[115] Von Seggern, D.H. (1990)
CRC Handbook of Mathematical Curves and Surfaces
CRC Press, Inc. Boca Raton, Florida

[116] Wang, L. and Pavlidis, T.
Direct Gray-Scale Extraction of Features for Character Recognition
IEEE PAMI, Vol. 15, No. 10, Oct. 1993, pp. 1053-1067

[117] Wang, C. Y., Sun, H., Yada, S., and Rosenfeld, A.
Some Experiments in Relaxation Image Matching Using Corner Features
Pattern Recognition Vol. 16 No. 2, 1983, pp.167-182

[118] Weszka, J.S.
A Survey of Threshold Selection Techniques
CVGIP, Vol. 7, 1978, pp. 259-265

[119] Zhang, Y.J.
Quantitative Study of 3D Gradient Operators
Image and Vision Computing, Vol. 11, No. 10, Dec 1993, pp. 611-622

[120] Zheng, Q. and Chellappa, R.
A Computational Vision Approach to Image Registration
IEEE IP, Vol. 2, No. 3, July 1993, pp. 311-325

[121] Zhou, X.
Digital Subtraction Mammography via Geometric Unwarping for Detection of Early Breast Cancer
Ph.D. Thesis, University of Manitoba, Winnipeg, 1991.

[122] Zubal, G., Tagare, H., Zhang, L. and Duncan, J.
3-D Registration of Intermodality Medical Images
IEEE EMBS, Vol. 13,, 1991 pp. 293-294

[123] Zucker, S.W.
Region Growing: Childhood and Adolescence
CGIP, Vol. 5, 1976, pp. 382-399